1
Aspects of Nuclear Physics and Astrophysics

1.1
History

In 1920, Aston discovered that the mass of the helium atom is slightly less than four times the mass of the hydrogen atom. Immediately afterward, Eddington suggested in his 1920 presidential address to the British Association for the Advancement of Science that Aston's discovery would explain the energy generation of the Sun via the conversion of hydrogen to helium. However, Eddington could not explain why the stellar temperatures inferred from observation were well below those thought necessary to initiate fusion reactions. In 1928 Gamow, and independently Condon and Gourney, calculated the quantum mechanical probability for particles to tunnel through potential barriers and thereby explained the phenomenon of α-particle decay (Gamow, 1928; Condon and Gourney, 1929). Atkinson and Houtermans used Gamow's results to suggest that quantum mechanical tunneling may explain the energy generation of stars via nuclear fusion reactions (Atkinson and Houtermans, 1929).

Cockcroft and Walton (1932) initiated the first nuclear reaction using artificially accelerated particles by bombarding and disintegrating lithium nuclei with protons accelerated to several hundred kilo electron volts energy. Incidentally, the disintegration of lithium into two α-particles is one of the reactions of what would later be called the *pp chains*. Lauritsen and Crane produced in 1934 a 10-min radioactivity following the bombardment of carbon with protons. It was the first measurement of one of the reactions of what would later be called the *CNO cycle*.

Atkinson (1936) proposed the fusion of two hydrogen nuclei to deuterium as a source of stellar energy generation. A detailed treatment of this reaction was provided by Bethe and Critchfield who showed that the p + p reaction gives an energy generation of the correct order of magnitude for the Sun (Bethe and Critchfield, 1938). The energy production in stars via the CNO cycle was independently discovered by von Weizsäcker (1938) and Bethe (1939). The latter work, in particular, investigated for the first time the rate of energy production and the temperature dependence of the CNO cycle.

In the following years some of the pioneering ideas of nuclear astrophysics were established. In two papers, Hoyle first presented the theory of nucleosynthesis

Nuclear Physics of Stars, Second Edition. Christian Iliadis.

within the framework of stellar evolution using the nuclear data available at the time (Hoyle *et al.*, 1946; Hoyle, 1954). Nuclear experiments had firmly established that no stable nucleus of mass number 5 or 8 exists in nature. For this reason, it was a mystery how these mass gaps could be bypassed in the synthesis of heavier nuclei from lighter species. Salpeter suggested in 1951 that a small equilibrium concentration of unstable ^{8}Be could capture another α-particle to form stable ^{12}C and that this *triple-α reaction* could be the main energy source in red giant stars (Salpeter, 1952). Hoyle pointed out that the capture probability would be far too small unless an excited state existed in ^{12}C at about 7.7 MeV excitation energy. The level was experimentally verified (Dunbar *et al.*, 1953) and its properties determined (Cook *et al.*, 1957), thereby establishing the triple-α reaction as the mechanism to overcome the mass 5 and 8 gaps.

In an influential review, Suess and Urey demonstrated the existence of several double peaks in a greatly improved distribution of observed solar-system abundances (Suess and Urey, 1956). It became immediately clear that these abundance peaks were associated with the neutron shell fillings at the magic neutron numbers in the nuclear shell model that Jensen and Goeppert Mayer had developed in 1949. The nucleosynthesis processes for the heavy nuclides beyond iron via neutron captures became later known as the *s- and r-processes*.

Of great importance was the discovery of spectral lines from the element technetium in evolved red giant stars (Merrill, 1952). All of the technetium isotopes are unstable and the longest lived isotope has a half-life of $\approx 4.2 \times 10^6$ y. Such half-lives are very short on a cosmological time scale ($\approx 10^{10}$ y) and, consequently, the discovery showed beyond doubt that the technetium must have been produced *recently* within the stars and that the products of nucleosynthesis could reach the stellar surface with the help of mass loss and mixing.

The available knowledge at the time regarding the synthesis of elements was presented in a review article by Burbidge *et al.* (1957), and independently by Cameron (1957). These papers laid the ground work for the modern theory of nuclear astrophysics. The field has developed since into an exciting discipline with impressive achievements, linking the topics of astronomical observation, nuclear physics experiment, nuclear theory, stellar evolution, and hydrodynamics.

1.2 Nomenclature

Atomic nuclei consist of protons and neutrons. The symbol Z denotes the number of protons and is called *atomic number*. The number of neutrons is denoted by the symbol N. The *mass number* A is defined by the integer quantity $A = Z + N$. It is sometimes also referred to as *nucleon number*. Nuclei with the same number of protons and number of neutrons have the same nuclear properties. They can be represented by the symbol ${}^{A}_{Z}\mathrm{X}_{N}$, where X is the element symbol. Any individual nuclear species is called a *nuclide*. Nuclides with the same number of protons,

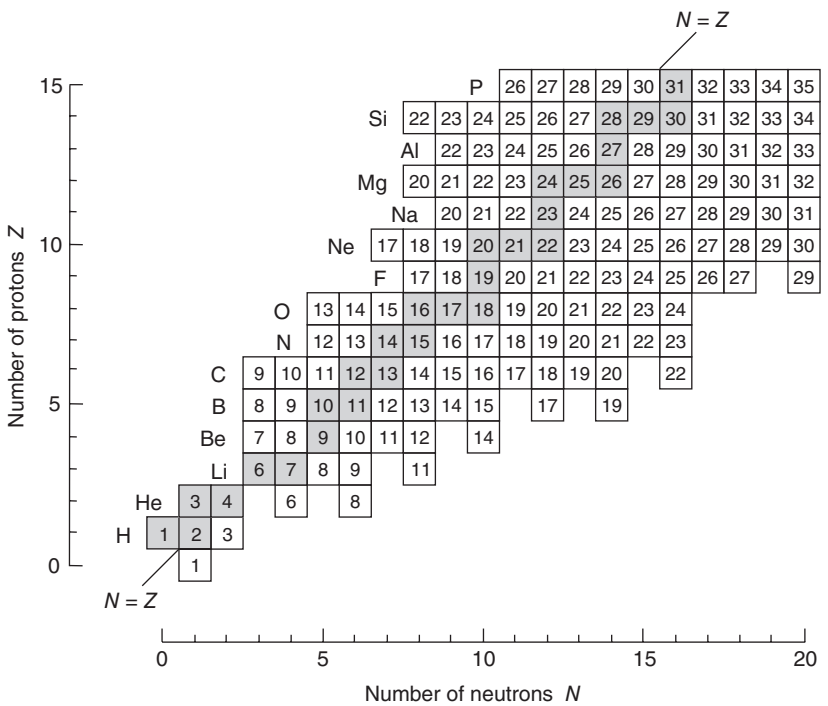

Figure 1.1 Section of the chart of the nuclides, showing the lightest species with $Z \leq 15$ and $N \leq 20$. The shaded squares represent stable nuclides, while the open squares correspond to unstable nuclides with half-lives in excess of 1 ms. The only exceptions are the nuclides ^{8}Be and ^{9}B, which have considerably shorter half-lives. No stable nuclides exist with a mass number of $A = 5$ or 8.

but different number of neutrons (and hence a different mass number A) are called *isotopes*. Nuclides of the same mass number, but with different numbers of protons and neutrons are called *isobars*. Nuclides with the same number of neutrons, but with different number of protons (and hence a different mass number A) are called *isotones*. Isotopes, isobars, and isotones have different numbers of protons or neutrons and, therefore, their nuclear physics properties are different.

Nuclides can be represented in a two-dimensional diagram, called *chart of the nuclides*. It displays the number of neutrons and protons on the horizontal and vertical axes, respectively. Each square in this diagram represents a different nuclide with unique nuclear physics properties. Figure 1.1 displays a section of the chart of the nuclides, showing the lightest species with $Z \leq 15$ and $N \leq 20$. The shaded squares represent stable nuclides, while the open squares correspond to unstable nuclides with half-lives in excess of 1 ms. Many more unstable than stable nuclides exist in nature. It is also striking that no stable nuclides exist with a mass number of $A = 5$ or 8. This circumstance has a profound influence on the nucleosynthesis in stars, as will be seen in Chapter 5.

Example 1.1

The nuclide of carbon ($Z = 6$) with 7 neutrons ($N = 7$) has a mass number of $A = Z + N = 13$ and is represented by the symbol ${}^{13}_{6}C_{7}$. Since the element symbol and the number of protons (atomic number) carry the same information, both $Z = 6$ and $N = A - Z = 7$ are frequently suppressed in the notation. The carbon species with mass number $A = 13$ is then unambiguously described by the symbol ${}^{13}C$.

The species ${}^{12}_{6}C_{6}$, ${}^{13}_{6}C_{7}$, and ${}^{14}_{6}C_{8}$ are isotopes of carbon ($Z = 6$); ${}^{20}_{10}Ne_{10}$, ${}^{20}_{11}Na_{9}$, and ${}^{20}_{12}Mg_{8}$ are isobars of $A = 20$; ${}^{28}_{14}Si_{14}$, ${}^{29}_{15}P_{14}$, and ${}^{30}_{16}S_{14}$ are isotones of $N = 14$.

1.3 Solar System Abundances

It is commonly accepted that the solar system formed from the collapse of a gaseous nebula that had an almost uniform chemical and isotopic abundance distribution. Abundances in the solar system are also similar to those found in many stars, in the interstellar medium of the Sun's neighborhood and in parts of other galaxies. Therefore, it was hoped for a long time that a careful study of solar system abundances would provide a "cosmic" or "universal" abundance distribution, that is, an average abundance distribution representative for all luminous matter in the universe. A closer comparison of abundances in the solar system and other parts of the universe shows, however, significant compositional differences. Furthermore, the discovery of presolar grains in primitive meteorites allowed for the first time a very precise chemical and isotopic analysis of interstellar matter. Measurements of isotopic abundances in these presolar grains revealed the existence of very large deviations compared to solar system values. Following common practice in the literature, we will avoid the term "universal" abundances and use instead the expression *solar system abundances* when referring to the abundance distribution in the solar system at the time of its formation. The latter distribution provides an important standard to which reference is frequently made.

There are two major, independent and sometimes complementary, sources of solar system elemental abundances: (i) observations of the solar photosphere, and (ii) analysis of a specific class of meterorites, called *CI carbonaceous chondrites*. The Sun contains most of the mass in the solar system and is, therefore, representative for the overall composition. On the other hand, planets contain considerably less mass but they underwent extensive chemical fractionation over the past 4.5 Gy since their formation (Cowley, 1995). Among the more than 20 000 recovered meteorites, there are only five known CI carbonaceous chondrites. Although they contain a minuscule amount of matter, they are believed to be among the most primitive objects in the solar system. They show the least evidence for chemical fractionation and remelting after condensation and thus they retained most of the elements (except for a few very volatile species) present in the original matter

of the solar nebula. Details on how these abundances are obtained will not be repeated here (see, e.g., Arnett, 1996; Grevesse and Sauval, 1998; Palme and Jones, 2003; Lodders, Palme, and Gail, 2009). It is sufficient to remark at this point that the abundances derived from the solar photosphere and from primitive meteorites are in remarkable overall agreement (better than ± 10% for most elements). Solar system *isotopic* abundances are then derived from the *elemental* abundances using mainly terrestrial isotopic ratios (Rosman and Taylor, 1998).

The solar system abundances of the nuclides are shown in Figure 1.2a versus mass number A. The abundances are normalized to the number of silicon atoms. In cases where two or more stable isobars exist for a specific mass number A, the sum of the individual abundances is shown. Figure 1.2b displays the abundances separately for even-A and odd-A nuclides. Almost all the mass is contained in ^{1}H (71.1%) and ^{4}He (27.4%). There is an abundance minimum in the $A = 5$–11 region, corresponding to the elements Li, Be, and B. More than half of the remaining mass (1.5%) is in the form of ^{12}C and ^{16}O. The abundances drop slowly with increasing mass number. Another minimum occurs in the $A = 41$–49 region, around the element Sc. The abundance curve exhibits a maximum in the $A =$ 50–65 region, near the element Fe. The nuclides in this region are referred to as the *iron peak*. Beyond the iron peak, the abundances in general decrease with increasing mass number, although pronounced maxima are visible in the $A = 110$–150 and $A = 180$–210 regions. Closer inspection of Figure 1.2b also reveals that even-A nuclides are generally more abundant than odd-A nuclides. Furthermore, the abundance curve for odd-A nuclides is considerably smoother than the one for even-A nuclides.

The outstanding gross features in Figure 1.2 are the abundance maxima and minima. Specifically, the abundances do not scatter randomly, but instead exhibit a certain regularity and systematics. It is reasonable to assume that the abundances within any group or subgroup of nuclides can be attributed primarily to a specific mechanism of nucleosynthesis. Starting with the work of Suess and Urey (1956), such tables of solar system abundances had an enormous influence on investigations of the origin of the elements and the development of nuclear astrophysics. Not only did it become possible to identify and study various processes of nucleosynthesis that left their distinctive signatures in the abundance distribution, but a connection could also be made to the environments in which these sources of nucleosynthesis operated. All nuclides, with few exceptions, are synthesized in stars. Therefore, the observed solar system abundances offer powerful clues to stellar history and evolution, and by extension, to the chemical evolution of the galaxy as a whole.

It is fascinating that the structures seen in Figure 1.2 reflect the nuclear physics properties of various processes occurring in nature. A few very general comments follow below. All of the hydrogen (^{1}H and ^{2}H) and most of the helium (^{3}He and ^{4}He) nuclei originated in the big bang. The most abundant of these, ^{1}H and ^{4}He, are the basic building blocks for the synthesis of heavier and more complex nuclei. A deep abundance minimum occurs in the Li–Be–B region. These nuclides are quickly destroyed in fusion reactions with protons since their cross sections are

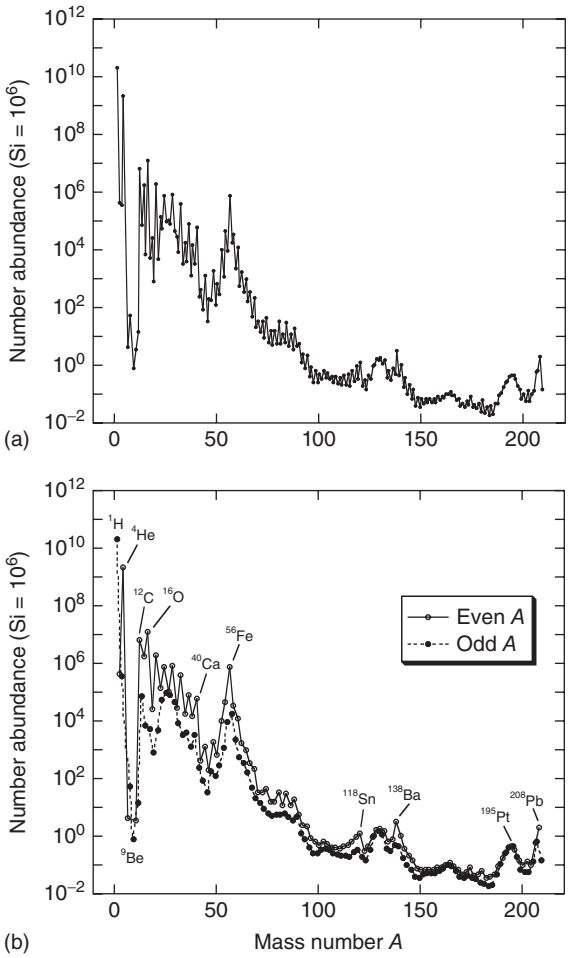

Figure 1.2 Abundances of the nuclides in the solar system at its birth. Number abundances are normalized to the number of silicon atoms (Si = 10^6). Data from Lodders (2003). (a) Sum of all nuclide abundances at a given value of A versus mass number. The maximum in the A = 50–65 region is referred to as the *iron peak*. (b) Separate abundance contributions from nuclides with an even or an odd value of A versus mass number. Even-A nuclides are in general more abundant than odd-A nuclides.

very large. Therefore, their observed solar system abundances must be explained by processes that occur in sites other than stellar interiors. They are thought to be produced via spallation reactions induced by Galactic cosmic rays. However, the big bang and certain stars did most likely contribute to the production of ^{7}Li. All of the heavier nuclides with $A \geq 12$ are produced in stars. The nuclides in the region between ^{12}C and ^{40}Ca are synthesized via charged-particle nuclear reactions in various stellar burning processes. Reactions between charged particles are subject to the Coulomb repulsion. The larger the charge of the reacting nuclei, the smaller

the nuclear reaction probability will become. This circumstance is reflected in the overall decline of the abundance curve from ^{12}C to ^{40}Ca. The abundance maximum of the iron peak occurs because these nuclides represent energetically the most stable species (Section 1.5.1). Because of the large Coulomb repulsion, the synthesis of nuclides beyond the iron peak via charged-particle reactions becomes very unlikely. These nuclei are instead produced by the capture of neutrons. The abundances of nuclides in the $A > 80$ region are on average a factor of 10^{10} smaller than the hydrogen abundance, as can be seen from Figure 1.2. The observed narrow and broad peaks in this mass region provide unambiguous evidence for the existence of two distinctive neutron capture processes. All of the above comments are very general and do not explain any details of the solar system abundance curve. An extensive discussion of the various nucleosynthetic processes will be given in Chapter 5. Information regarding the origin of the solar system nuclides is provided at the end of this book (Section 5.8).

1.4
Astrophysical Aspects

1.4.1
General Considerations

The study of stars is central to astronomy and astrophysics since stars are long-lived objects that are responsible for most of the visible light we observe from normal galaxies. The fusion of light nuclides into heavier species liberates kinetic energy at the expense of mass and serves as the interior source of the energy radiated from the surface. These very same reactions alter the composition of the stellar matter. As already pointed out, all nuclides with masses of $A \geq 12$ are produced in stars. When a star ejects part of its mass into space during certain evolutionary stages, the chemical composition of the interstellar medium will be altered by the thermonuclear debris. The interstellar medium, in turn, plays a key role in providing material out of which new generations of stars form. This cycling of matter between stars and the interstellar medium involves countless stars. By comparing the age of the Galaxy (≈ 14 Gy) with the age of the Sun (≈ 4.5 Gy) we can conclude that the cycling process that gave rise to the solar system abundance distribution operated for almost 10 billion years.

There is unambiguous *direct* evidence for the nucleosynthesis in stars. First, we already mentioned in Section 1.1 the observation of radioactive technetium in stellar spectra (Merrill, 1952). Second, γ-rays from radioactive ^{26}Al were discovered in the interstellar medium by spectrometers onboard satellites (Mahoney *et al.*, 1982; Diehl *et al.*, 1993). The half-life of this nuclide ($\approx 7.17 \times 10^5$ y) is even shorter than that for radioactive technetium, thus demonstrating again that nucleosynthesis is currently active in the Galaxy. Third, neutrinos are predicted to be the byproducts of nuclear processes in stars (Chapter 5). Since they interact very weakly with matter, they escape essentially unimpeded from stellar interiors.

Neutrinos from the Sun (Bahcall, 1989; Hirata *et al.*, 1990; Bellini *et al.*, 2014) and from the type II supernova 1987A (Hirata *et al.*, 1987; Bionta *et al.*, 1987) were detected on Earth, providing another direct test of stellar nucleosynthesis. Fourth, models of supernovae predict the ejection of radioactive ^{56}Ni (half-life of 6 days), which then decays to the radioactive daughter nucleus ^{56}Co (half-life of 77 days). The subsequent decay of this nuclide to stable ^{56}Fe is predicted to determine the decline of the light emission from these stellar explosions. The predictions agree well with the observed light curves of supernovae. Furthermore, the energetic γ-rays produced in the radioactive decays initially thermalize and deposit their energy via Compton scattering and photoelectric absorption. Because of the expansion, however, the column density decreases with time and the ejecta eventually become transparent. Photons from the radioactive decays of ^{56}Co and ^{44}Ti have been directly detected from supernova 1987A (Matz *et al.* 1988; Tueller *et al.* 1990; Grebenev *et al.* 2012).

The discovery of the existence of two distinct stellar populations by astronomers was also of paramount importance in this respect. The populations are referred to as *population I* and *population II* stars. They differ in their age and their content of metals, by which astronomers mean any element other than hydrogen and helium. Population I stars, including the Sun, are metal rich. They are young stars, having formed within the past few billion years, and can be found in the disk of the Galaxy. Extreme population I stars represent the youngest, most metal-rich stars and are found in the spiral arms of the Galaxy. Population II stars, on the other hand, are metal poor. They are relatively old and are found in the halo and the bulge of the Galaxy. Extreme population II stars represent the oldest, most metal poor stars and are found in the halo and in globular clusters. Their metal abundance, relative to hydrogen, is smaller by a factor of 100 or more compared to population I stars.

If one assumes that the initial composition of the Galaxy was uniform and if there exists no mechanism capable of concentrating the metals in the disk of the Galaxy, then the Galaxy must have synthesized an overwhelming fraction of its own metals. This argument provides strong support for the theory that nucleosynthesis is a natural process to occur during the evolution of stars. The metal content of the Galaxy increases with time since the matter out of which stars form is being cycled through an increasing number of stellar generations. Therefore, the differences in metallicity between the two stellar populations suggest that population I stars formed later during the history of the Galaxy when the interstellar medium became metal rich.

Nuclear reactions not only are required for explaining the bulk solar-system abundance distribution, but also are indispensable for explaining the observed chemical composition of individual stars. Such observations, even for trace elements, are crucial for constraining theoretical models of stars and for better understanding the complicated interplay of stellar hydrodynamics, convection, mixing, mass loss, and rotation. Stellar nucleosynthesis also plays a decisive role for explaining the chemical composition of the interstellar medium and is thus

intertwined with γ-ray astronomy, the study of primitive meteorites, and the nature of cosmic rays.

1.4.2 Hertzsprung–Russell Diagram

The total amount of radiation emitted per unit time, or the *luminosity*, varies strongly from star to star. The same holds for the effective stellar surface temperature. However, if we plot these two quantities for many individual stars in a diagram, then the result is not a random scatter of points, but most stars fall into several distinct groups. This correlation of stellar luminosity and effective surface temperature represents the single most important relationship of stellar properties. It is referred to as *Hertzsprung–Russell diagram* or color-magnitude diagram. The latter name implies that the surface temperature can be expressed in terms of the color of the star, while luminosity is related to the absolute magnitude. An explanation of these relationships can be found in any introductory astronomy textbook. The Hertzsprung–Russell diagram has a profound influence on the theory of stellar evolution and, by extension, on the history of the Galaxy as a whole.

Consider first Figure 1.3a, showing a Hertzsprung–Russell diagram for a sample of ≈ 5000 stars in the solar neighborhood. Each dot corresponds to a single star. The surface temperature increases from right to left in the figure. The vast majority of stars occupy the *main sequence* (MS), stretching diagonally from the upper left (hot and bright stars) to the lower right (cool and faint stars). The Sun, for example, belongs to the main sequence. In the low and right part (cool and faint stars) of the main sequence one finds the *red dwarfs* (RD). The *subgiant branch* (SGB) joins the main sequence and extends in a direction to cooler and brighter stars, where the populated region turns first into the *red clump* (RC), and then into the *red giant branch* (RGB). In a region corresponding to smaller luminosity and higher temperature (lower left), one finds a group of faint and hot stars known as *white dwarfs* (WD). A well-known example is Sirius B, the companion of Sirius. Some stars are located below the main sequence, but are considerably brighter than white dwarfs. These are known as *subdwarfs* (SD). A number of star categories do not appear in the figure. *Supergiants* (SG) are the brightest stars in the Galaxy and would occupy the upper end of the Hertzsprung–Russell diagram, but are very rare in the solar neighborhood. The cool and faint *brown dwarfs* would appear off scale way down in the lower-right, but are too faint to appear in the figure.

A Hertzsprung–Russell diagram for the globular cluster M 3 is shown in Figure 1.3b. There are about 200 globular clusters in the Galaxy. They are located in a spherical space surrounding the Galactic center, called the *halo of the Galaxy*. Each cluster consists of 10^4–10^6 gravitationally bound stars that are highly concentrated toward the cluster center. An image of the globular cluster M 10 is shown in color Figure 1 on page 613. Spectroscopic observations revealed that globular clusters are metal poor compared to the Sun, implying that they are very old and that they formed during the early stages of Galactic evolution. It is

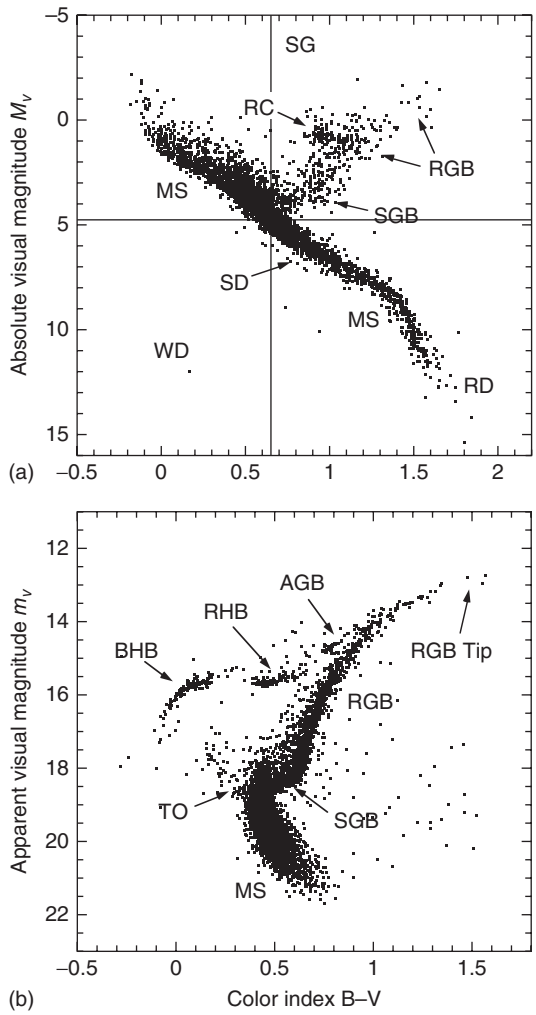

Figure 1.3 Observational Hertzsprung–Russell diagrams, showing visual magnitude versus color index B–V. Each dot corresponds to a star. See the text for an explanation of the labels. (a) Sample of ≈ 5000 stars in the solar neighborhood with precisely known distances. The data were acquired by the Hipparcos astrometry satellite. The vast majority of stars occupy the main sequence, stretching diagonally from the hot (blue) and luminous upper left to the cool (red) and faint lower right. The cross hair indicates the position of the Sun. Certain categories of stars do not appear in the figure, for example, supergiants, which are rare in the solar neighborhood, and brown dwarfs, which are too faint for detection by Hipparcos. (b) Data for the globular cluster M 3. Apparent rather than absolute magnitude is displayed on the vertical axis since the stars have the same distance from the Earth. The RR Lyrae variable stars, located between the red (RHB) and blue (BHB) horizontal branches, are omitted. Data from Corwin and Carney (2001).

commonly accepted that all stars in a typical globular cluster formed around the same time from material of very similar composition. The observation that the stars of a globular cluster occupy distinct regions in the Hertzsprung–Russell diagram must then be explained by differences in the only other major stellar property, that is, their initial mass. As will be shown below, the stellar mass is the most important property influencing the evolution of stars: the higher the mass, the faster a star will evolve.

Figure 1.3b shows some of the same stellar categories already mentioned in connection with Figure 1.3a. The densest region is occupied by main-sequence stars. The distinctive kink extending from the main sequence toward cooler and brighter stars is called the *turn-off point* (TO). The supergiant branch stars (SGB) are located on a horizontal part stretching toward the right, which turns upward into the red giant branch (RGB). Three more groups of stars can be distinguished on the left-hand side of the red giant branch: the asymptotic giant branch (AGB), the red horizontal branch (RHB), and the blue horizontal branch (BHB). As will be seen below, the different groups of stars seen in Figure 1.3a,b correspond to different stages of stellar evolution. Globular clusters in particular play an outstanding role in astrophysics since the distinct features in their Hertzsprung–Russell diagrams represent strong constraints for stellar models.

1.4.3
Stellar Evolution of Single Stars

One of the most important goals of the theory of stellar structure and evolution is to understand why certain stars appear only in specific regions of the Hertzsprung–Russell diagram and how they evolve from one region to another. Our aim in this section is to summarize without detailed justification the most important issues related to the nuclear physics of stars. An introduction to stellar evolution can be found in Binney and Merrifield (1998) or Iben (1985). A more comprehensive account is given, for example, in Kippenhahn and Weigert (1990). We will use in this section expressions such as hydrogen burning, helium burning, pp chain, CNO cycle, and so on, to obtain a general idea regarding nuclear processes in stars. These will be explained in depth in Chapter 5.

Theoretical models of stars in hydrostatic equilibrium are constructed in the simplest case by solving a set of four partial differential equations (for radius, luminosity, pressure, and temperature) that describe the structure of a star as a function of the distance from the center and as a function of time. A time sequence of such solutions, or stellar models, represents an *evolutionary track* in the Hertzsprung–Russell diagram. Stellar structure and evolution calculations rely heavily on large scale numerical computer codes. The time changes in the stellar properties are closely related to the energy budget. Energy is generated by the star via nuclear reactions and gravitational contraction, while energy is continuously lost from the stellar surface via emission of photons and neutrinos. As will become clear in the following discussion, a star spends most of its nuclear burning time fusing hydrogen to helium on the main sequence. Careful observations revealed a

direct correlation between the mass and the luminosity of a main-sequence star. The greater the total mass of the star, the greater the temperature and pressure in the core, the faster nuclear energy is generated, and the greater the energy output or the luminosity of the star. For example, a $10\,M_\odot$ main-sequence star has ≈ 3000 times the luminosity of the Sun. Furthermore, the main-sequence lifetime will also depend strongly on the stellar mass because a star burns the nuclear fuel at a rate that is determined by its luminosity. For example, solar-metallicity stars with masses of $1\,M_\odot$, $5\,M_\odot$, and $15\,M_\odot$ spend about 10 Gy, 100 My, and 12 My, respectively, on the main sequence. Once a star leaves the main sequence, the evolution speeds up significantly, as will be seen below.

Modern theories have been enormously successful in describing the properties of stars. Nevertheless, many open questions remain unsolved. Stellar evolution is an active research field and it is worthwhile to keep in mind the uncertainties in the model calculations. These reflect our incomplete knowledge of certain processes in stars, including the treatments of energy transport via convection, mass loss, atomic diffusion, turbulent mixing, rotation, and magnetic fields. For binary stars (Section 1.4.4), a host of additional problems is encountered because, first, the model assumption of spherical symmetry must be relaxed and, second, the interaction between the two stars becomes important. We will not discuss these effects in any detail other than to mention that most of them become increasingly important with ongoing stellar evolution. The effects of nuclear physics are deeply intertwined with these issues. When we discuss in later chapters the impact of nuclear physics uncertainties on the nuclear energy generation and the nucleosynthesis, it is very important to keep in mind that we are referring only to one piece in a complex puzzle. One of the main goals in nuclear astrophysics is to better understand the inner workings of stars. To this end, a reliable knowledge of nuclear physics is indispensable.

A chart showing the main evolutionary phases for single stars of various initial masses is shown in Figure 1.4 and will be helpful for the subsequent discussions. The stellar masses are shown on the left-hand side and time increases from left to right.

Premain-Sequence Stars

When an interstellar gas cloud consisting mainly of hydrogen and helium contracts, gravitational potential energy is transformed into thermal energy and into radiation. The gas is initially in gravitational free fall and most of the liberated energy is not retained but radiated away because the gas is relatively transparent. With increasing density, the opacity increases as well and some of the emitted radiation is retained in the cloud. As a result, the temperature and the pressure begin to rise and the contraction of the central, denser part of the cloud slows down. The increasing temperature causes first a dissociation of hydrogen molecules into atoms, and then an ionization of hydrogen and helium atoms. When a temperature of about 10^5 K is reached, the gas is essentially ionized. The electrons trap radiation efficiently and, as a result, the pressure and temperature increase and the collapse of the central part of the cloud halts. The premain-sequence star

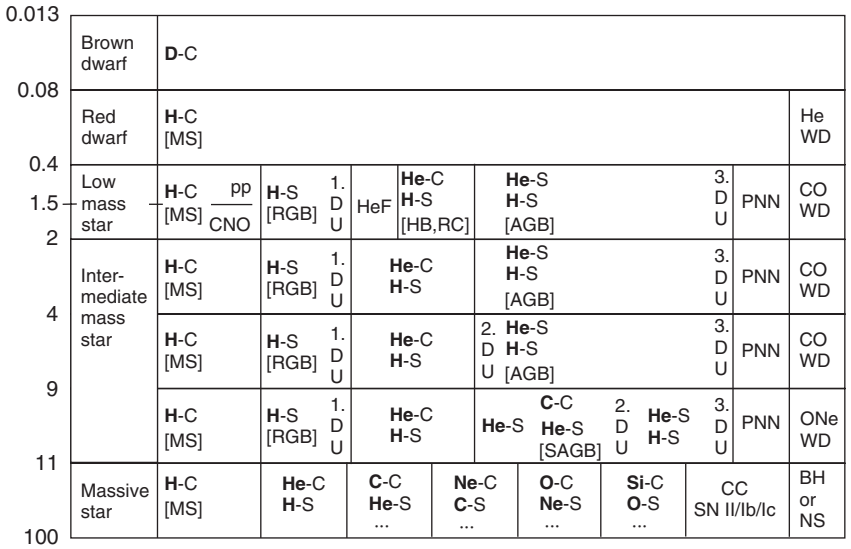

Figure 1.4 Major evolutionary stages for single stars in different mass ranges. The initial stellar mass is given on the left-hand side. Time increases from left to right. The nuclear fuel in each burning phase is shown in bold. For example, "**H**-C" refers to hydrogen burning in the core, "**He**-S" denotes helium burning in a shell, and so on. For lower-mass stars, the meaning of the labels in square brackets is described in the text (see also caption of Figure 1.5); "DU" denotes the different dredge-up events. For massive stars, the three dots indicate that there are additional overlying burning shells (Figure 1.7); the labels are: "CC" for core collapse, "SN" for supernova, "NS" for neutron star, and "BH" for black hole. The mass ranges are approximate estimates only and depend on the stellar metallicity. For the evolution of stars in the mass range of $M \geq 100\,M_{\odot}$, see Woosley, Heger, and Weaver (2002), and references therein.

eventually reaches a state of hydrostatic equilibrium, while still accreting matter from the outer parts of the cloud.

The source of energy is gravitational contraction, but the first nuclear reactions start to occur when the central temperature reaches a few million kelvin. Primordial deuterium fuses with hydrogen, a process that is called *deuterium burning* (Section 5.1.1), and primordial lithium may be destroyed via interactions with protons ($^7\mathrm{Li} + \mathrm{p} \rightarrow \alpha + \alpha$; the notation will be explained in Section 1.5.2). At this stage, energy is transported via convection and most of the star's matter, including surface material, is expected to be processed through the center. Although the nuclear energy release is very small, the reactions change the light element abundances and thus provide valuable information on the central temperatures.

When the temperature reaches several million kelvin, the fusion of hydrogen to helium starts to occur and contributes an increasing fraction to the total energy output. Ultimately, a point will be reached where hydrogen fusion in the core becomes the only source of energy. The star is now in hydrostatic and thermal equilibrium and has reached a location in the Hertzsprung–Russell diagram that

is referred to as the *zero age main sequence* (ZAMS). Stars with different initial masses reach the main sequence at different times. For example, the premain-sequence evolution of a $1\,M_\odot$ star lasts about 75 million years. Different stellar masses populate different locations on the zero age main sequence, which thus represents a line in the Hertzsprung–Russell diagram. Massive stars have higher temperatures, initiate nuclear reactions earlier, and are therefore located on the hotter and brighter part (upper left), while less massive stars will be found on the cooler and fainter part (lower right).

Newly born stars are difficult to observe because they are usually surrounded by a rotating disk of gas and dust. The solar system, for example, presumably formed from such a disk. Examples for premain-sequence objects are the *T Tauri stars*. Their lithium abundance is relatively high, indicating that the central temperature has not yet reached large enough values to destroy lithium via nuclear reactions involving protons.

The subsequent fate of stars depends strongly on their initial mass. We will consider the different mass ranges in turn. These main divisions are not sharp but depend somewhat on the chemical composition.

Initial Mass of $0.013\,M_\odot \lesssim M \lesssim 0.08\,M_\odot$

Theory predicts that objects in this mass range never reach the central temperatures required to sustain hydrogen fusion in their cores and are thus unable to generate sufficient nuclear energy to provide pressure support. The search for these very faint and cool stars provides important constraints for stellar evolution theory. Such objects have only been discovered in the mid-1990s and are referred to as *brown dwarfs*. They are predicted to be very abundant in the Galaxy and are, therefore, candidates for the elusive (baryonic) dark matter. Brown dwarfs are fully convective and their energy source in the early stages is provided by gravitational contraction.

Although brown dwarfs are not true stars, they do have enough mass to undergo deuterium burning, which sets them apart from massive planets such as Jupiter. This provides an additional, low-level, source of energy. They also have a relatively high lithium abundance since temperatures remain too low to destroy this element. The outer layers of a brown dwarf can be described by the ideal gas law. The core, however, becomes eventually electron degenerate. As a result, the contraction halts and the brown dwarf slowly cools, at approximately constant radius, by radiating its thermal energy into space. In the Hertzsprung–Russell diagram, a brown dwarf evolves almost vertically downward and straight past the main sequence (Figure 1.3).

A detailed description of the properties of degenerate matter is given in many modern physics textbooks and is not repeated here. We will summarize a few properties, however, that are also important for our discussion of other stars. Matter becomes degenerate at relatively high densities as a result of the Pauli exclusion principle which states that no more than two spin-1/2 particles (such as electrons) can occupy a given quantum state simultaneously. A degenerate gas strongly resists further compression because electrons cannot move into

lower energy levels that are already occupied. Unlike an ideal classical gas, whose pressure is proportional to its temperature, the pressure exerted by a completely degenerate gas does not depend on temperature. Or, in other words, increasing the temperature of a partially degenerate gas has only a small effect on the total pressure. It will be seen later that, when the temperature reaches a sufficiently high value, the degeneracy is lifted, by which we mean that the properties of such a gas revert to those of an ideal classical gas. Furthermore, there exists an upper limit to the pressure provided by a degenerate gas. If gravity exceeds this pressure, the star will collapse despite the presence of the degenerate particles. The maximum value for the mass of a star that can maintain an equilibrium between degeneracy pressure and gravity is called the *Chandrasekhar limit*. Its precise value depends on the composition. For an electron degenerate gas and matter characterized by two nucleons per electron (e.g., ^{4}He, ^{12}C, or ^{16}O), the limiting value is $\approx 1.44\,M_\odot$. Stars that enter a state of electron degeneracy toward the end of their evolution are called *white dwarfs*. White dwarfs with masses in excess of the Chandrasekhar limit are not observed in nature.

Initial Mass of $0.08\,M_\odot \lesssim M \lesssim 0.4\,M_\odot$

Stars in this mass range are sometimes referred to as *red dwarfs* (or M dwarfs). They are the most common type of star in the neighborhood of the Sun. For example, the nearest star to the Sun, Proxima Centauri, is a red dwarf. These stars have sufficient mass to fuse hydrogen to helium (*hydrogen burning*) in their cores via the pp chain. Starting from the zero age main sequence, the red dwarf evolves toward higher luminosity and increasing surface temperature (up and left). All stars that sustain hydrostatic equilibrium by burning hydrogen in their cores are called *main-sequence stars*. Theoretical models indicate that, for example, a $0.1\,M_\odot$ star of solar metallicity remains on the main sequence for about 6000 Gy. During this time the red dwarf is fully convective, which implies that its entire hydrogen content is available as nuclear fuel. Since the age of the universe is about 14 Gy, all red dwarfs that we observe must be main-sequence stars. Eventually, they will run out of nuclear fuel, that is, all their hydrogen will be converted to helium. Red dwarfs do not have enough mass to produce the higher temperatures required to fuse helium nuclei. Thus, they contract until electron degeneracy sets in. Their volume is constant from then on since the degeneracy pressure resists further compression. They become helium white dwarfs that cool slowly by radiating away their thermal energy.

Initial Mass of $0.4\,M_\odot \lesssim M \lesssim 2\,M_\odot$

The evolution of stars in this mass range is considerably more complicated compared to the previous cases. The life of the star starts on the zero age main sequence when hydrogen begins to fuse to helium in the core. In stars with masses below $M \approx 1.5\,M_\odot$, hydrogen fusion proceeds via the pp chains, while more massive stars burn hydrogen via the CNO cycles in their cores. It will be seen later that these different processes affect the stellar structure since they possess very different

temperature dependences (Section 5.1). In stars with $M \gtrsim 1.5\,M_\odot$, the strong temperature dependence of the CNO cycles concentrates the energy production in the center and, as a result, the core transports energy via convection. In stars with $M \lesssim 1.5\,M_\odot$, the energy generated in the core by the pp chains is transported via radiation.

As an example, we will discuss in the following the evolution of a special star, the Sun (see color Figure 2 on page 614). The evolutionary track is shown schematically in Figure 1.5a. The arguments given below follow the numerical results obtained by Sackmann, Boothroyd and Kraemer (1993). The Sun started central hydrogen burning via the pp chains on the zero age main sequence about 4.5 Gy ago. At present, the central temperature and density amount to $T \approx 15$ MK and $\rho \approx 150$ g/cm^3, respectively, and about one half of the original hydrogen in the core has been consumed so far. The Sun has a very small convective region at the surface, comprising only $\approx 2\%$ of its entire mass. About 4.8 Gy from now, the hydrogen in the core will be exhausted. The Sun will then be located at the bluest and hottest point on the main sequence, called the *turn-off point*. Note that in Figure 1.5a the track describing nuclear burning on the main sequence follows an arc. This partially explains why the main sequence in observational Hertzsprung–Russell diagrams represents a band rather than a narrow line.

Hydrogen fusion continues via the CNO cycles in a shell near the core where hydrogen is still left. The Sun slowly leaves the main sequence at this point. The Sun's center begins to contract to generate energy that is no longer provided by nuclear processes and the contraction causes further heating. As a result, the temperature in the hydrogen burning shell, and the associated nuclear energy generation rate, also increase. Initially, the Sun has not yet developed a fully convective envelope and it is called a *subgiant branch star* (SGB). Eventually, the envelope becomes fully convective. The extra energy output from the hydrogen burning shell results in a dramatic surface expansion and engulfs the planet Mercury. The Sun becomes a red giant star. While the Sun ascends the red giant branch, the luminosity increases continuously. Maximum luminosity is achieved on the tip of the red giant branch after about 0.6 Gy from the time when the Sun left the main sequence. During the red giant branch phase the Sun starts to experience significant mass loss. The contraction of the core during the red giant phase increases the central temperature and density by factors of 10 and 10^4, respectively, compared to the values at hydrogen ignition. The core achieves such high densities that the matter becomes electron degenerate. During the red giant branch phase, the convective envelope deepens significantly until it comprises about 75% of the Sun's mass. This deep convective envelope dredges up the products of hydrogen burning from the outer core. The process is referred to as the *first dredge-up*.

When the temperature reaches about $T \approx 0.1$ GK, the helium in the core starts to fuse to carbon and oxygen (*helium burning*). In a normal gas, the extra energy release would cause an expansion. As a result, the temperature would fall and the nuclear energy generation rate would decrease as well. This is the usual manner by which stars adjust to an energy increase in their interior, allowing them to stabilize.

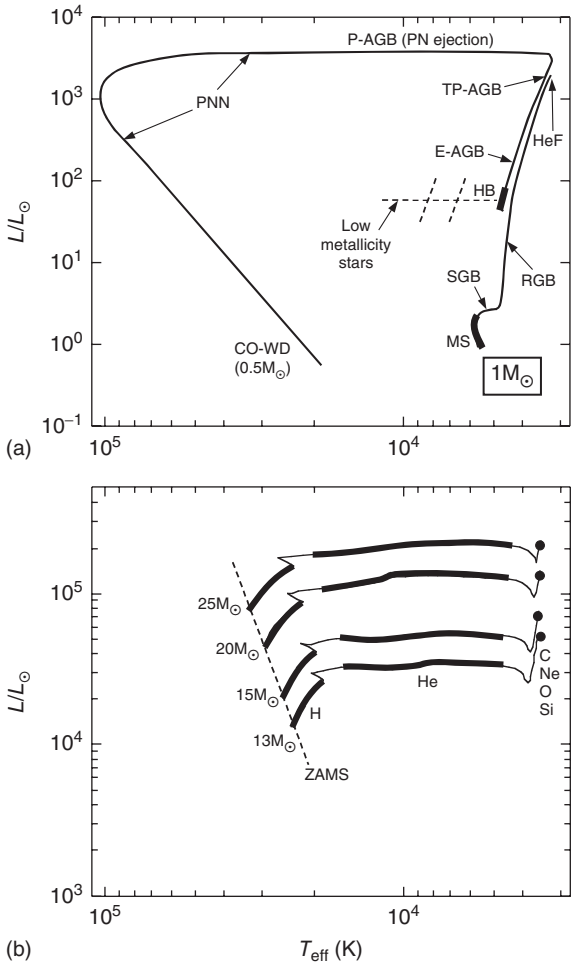

Figure 1.5 Schematic evolutionary tracks of (a) the Sun, and (b) massive stars of initial solar composition, in the Hertzsprung–Russell diagram; the luminosity on the vertical axis is given in units of the present solar luminosity. The heavy portions define the locations where major core nuclear burning phases occur. Details of tracks during transitions between major nuclear burning phases are omitted. The meaning of the labels are: main sequence (MS); zero age main sequence (ZAMS); subgiant branch (SGB); red giant branch (RGB); core helium flash (HeF); horizontal branch (HB); early asymptotic giant branch (E-AGB); thermally pulsing asymptotic giant branch (TP-AGB); post asymptotic giant branch (P-AGB); planetary nebula nucleus (PNN); carbon–oxygen white dwarf (CO-WD). Metal-poor stars in the initial mass range of $0.4\,M_\odot \lesssim M \lesssim 2\,M_\odot$ appear during core helium burning in a region marked by the horizontal dashed line in part (a), depending on the mass loss during the red giant branch phase. The two dashed diagonal lines indicate the instability strip. In part (b) the core burning phases are labeled by the nuclear fuel: hydrogen (H), helium (He), carbon (C), and so on. The onset of carbon burning is marked by the full circle. Note the vastly different luminosity scale in parts (a) and (b).

However, in a degenerate gas the temperature increase does not affect the pressure. No expansion occurs and, as a result, the temperature increases causing an even higher energy generation rate. As will be seen in Section 5.2, helium burning is highly temperature sensitive. The sequence of events repeats itself, giving rise to a *thermonuclear runaway*. It only terminates after a considerable energy is released that lifts the degeneracy. Thus, the ignition of helium in the core results in a violent *core helium flash* (HeF).

Notice that the helium flash does not represent a stellar explosion. The energy during the thermonuclear runaway goes into lifting the electron degeneracy and into the subsequent expansion of the core. The surface luminosity of the star does not increase, but the opposite happens. The surface luminosity declines by two orders of magnitude because the expansion of the core causes the surrounding hydrogen burning shell, which has been supplying all the surface luminosity, to cool and to generate less energy. Eventually, the Sun becomes a *horizontal branch* star, quietly burning helium in the core. The temperatures in the hydrogen shell just above the core are high enough for hydrogen to continue to burn via the CNO cycles. The nuclear energy release in helium fusion is considerably smaller compared to hydrogen fusion. Therefore, the duration of the core helium burning stage is considerably shorter than that of the core hydrogen burning stage. The Sun remains on the horizontal branch for about 0.1 Gy, which is typical for all stars in this mass range.

When the helium in the core is exhausted, the core contracts again, heats up, and ignites the helium in a surrounding shell. The Sun now burns nuclear fuel in two shells, helium in a shell surrounding the carbon–oxygen core, and hydrogen in a shell surrounding the helium burning region. The two shells are separated by an intershell region consisting mainly of helium. This stage is referred to as the *early asymptotic giant branch phase* (E-AGB), because the second ascent of the giant branch merges almost asymptotically with the first giant branch (at least for some stellar masses). While the Sun ascends the asymptotic giant branch, the helium burning shell becomes thermally unstable (Schwarzschild and Härm, 1965, see also Section 5.6.1). Energy is not generated at a steady rate, but the hydrogen and helium burning shells alternate as the major contributor to the overall luminosity. The details are rather complex, but an overview can be obtained from Figure 1.6, showing the time evolution of the stellar region at the interface of the hydrogen envelope and the carbon-oxygen core. The hydrogen and helium burning shell is depicted as thick and thin solid black line, respectively. For about 90% of the time, the hydrogen burning shell provides the Sun's nuclear energy, while the helium shell is only marginally active. Hydrogen burning adds continuously to the mass of the helium zone, however, so that the temperature and density near this zone rise until energy is generated by helium burning at a rate that is larger than the rate at which it can be carried outward by radiative diffusion. As a result, a thermonuclear runaway occurs. The sudden release of energy drives convection within the helium-rich intershell and extinguishes the hydrogen burning shell. The helium burning shell is now the only source of nuclear energy. Eventually, the expansion and associated cooling quenches the helium shell flash (or *thermal*

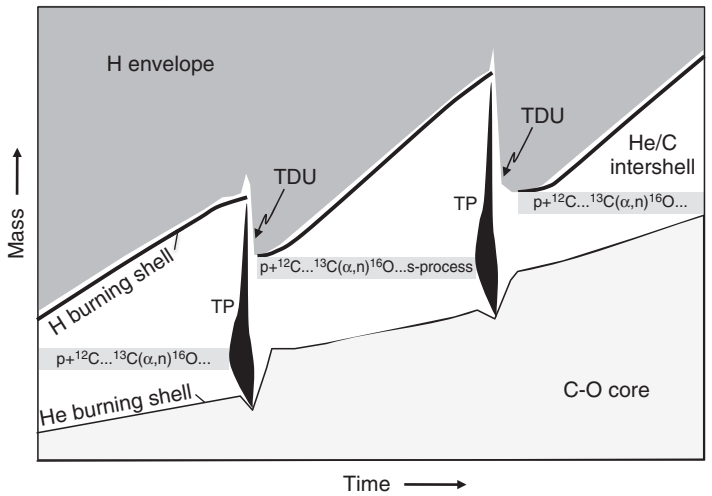

Figure 1.6 Schematic representation (mass versus time) of a low- or intermediate-mass ($M \lesssim 9\ M_{\odot}$), thermally pulsing AGB star. The figure is not to scale. Shown are: convective H envelope (dark gray); radiative ^{4}He-^{12}C intershell (white); degenerate C–O core (light gray). The thick and thin black line indicates the H-burning shell, which is active between thermal pulses, and the weakly active He-burning shell, respectively. For regular short periods of time, the barely active He shell ignites in a thermal pulse (TP), giving rise to a convective region (black) that extends over the entire intershell, extinguishing in the process the H-burning shell. When the thermal pulse comes to an end, the convective shell disappears and the quiescent He-burning resumes. Important mixing episodes occur at the end of each thermal pulse: (i) the convective envelope reaches into the intershell so that synthesized matter is transported to the stellar surface (third dredge-up; TDU); (ii) protons diffuse from the base of the envelope into the intershell, where they are captured by ^{12}C to produce (after β-decay) ^{13}C. Neutrons are then released by the ^{13}C(α,n)^{16}O reaction, producing *in situ* the main s-process component. During the subsequent thermal pulse, temperatures can be high enough to initiate the ^{22}Ne(α,n)^{25}Mg neutron source (Section 5.6.1).

pulse; solid black region labeled "TP" in Figure 1.6) and the Sun contracts again. The hydrogen burning shell reignites and ultimately takes over as the dominant nuclear energy source, until the next thermal pulse occurs about 10^5 y later. The cycle may repeat many times. This evolutionary stage is called the *thermally pulsing asymptotic giant branch (TP-AGB)*. The total amount of time the Sun spends on the AGB amounts only to about 20 My and is thus very short compared to the main-sequence lifetime. The thermal pulses cause the Sun's radius to vary periodically by a factor of 4, with the peak radius reaching close to the Earth.

The Sun suffers an episode of significant mass loss on the AGB via a strong stellar wind. Thermal pulses are ceasing at this point as the Sun becomes a post-asymptotic giant branch star (P-AGB), with only a fraction of its initial mass left and the other part returned to the interstellar medium. As more hydrogen of the envelope is ejected into space, hotter layers are uncovered and the Sun begins to move in the Hertzsprung–Russell diagram toward higher surface temperatures

(horizontally to the left). When the surface of the Sun becomes hot enough, the intense ultraviolet radiation ionizes the expanding ejecta, which begin to fluoresce brightly as a *planetary nebula* (PN). Two examples for planetary nebulae, the Dumbbell Nebula and the Cat's Eye Nebula, are shown in color Figures 3 and 4 on pages 615 and 616, respectively. The residual core is called a *planetary nebula nucleus* (PNN). Eventually, the hydrogen envelope disappears and the hydrogen burning shell extinguishes. The luminosity decreases rapidly causing the evolutionary track to turn downward and slightly to the right. The Sun will then end its existence as a white dwarf with a mass of $\approx 0.5\,M_{\odot}$, consisting mainly of carbon and oxygen. It is supported by electron degeneracy pressure and cools slowly by radiating away its thermal energy.

In the above discussion, the evolution beyond the red giant branch is rather uncertain because of our incomplete knowledge for predicting convection and mass loss. That these effects will occur has been demonstrated by stellar observations, but a deeper understanding is lacking at present. It is generally accepted that each thermal pulse during the TP-AGB phase provides favorable conditions for another dredge-up episode after the end of flash-burning in the helium shell. The convective envelope reaches deep into the intershell region, carrying the products of helium burning (mainly carbon, but also elements heavier than iron) to the stellar surface. This process is referred to as the *third dredge-up* (labeled "TDU" in Figure 1.6) and increases the carbon abundance in the envelope relative to other elements, for example, oxygen. Stars for which the number ratio of carbon to oxygen in their atmospheres exceeds unity are called *carbon stars*. Many of these have been observed and most are believed to correspond to stars in their TP-AGB phase. As will be seen later, AGB stars are also the source of many heavy nuclides with mass numbers beyond $A = 60$. Stellar models predict that these (s-process) nuclei are also dredged up to the surface where they can be observed in stellar atmospheres. The first direct evidence that nucleosynthesis takes place in stars and that the products could be mixed to the surface was the observation of radioactive technetium in certain (S-type) carbon stars (Section 1.1). For more information on AGB stars, see Habing and Olofsson (2004).

We are now in a position to understand some other details in the observational Hertzsprung–Russell diagrams shown in Figure 1.3. The precise location in luminosity and surface temperature of a star on the horizontal branch depends on the chemical composition of the envelope, the size of the helium core at the time of the helium flash, and the mass of the envelope which is influenced by the mass loss during the preceding red giant branch phase. In a globular cluster, all the stars start out with the same, low-metallicity, composition and their location on the horizontal branch is mainly influenced by mass loss. The more the mass lost from the hydrogen envelope, the hotter the layers in the star are uncovered. Stars with the smallest amount of mass in the hydrogen envelope populate the blue part (BHB), while stars with more hydrogen left in the envelope can be found on the red part (RHB). The horizontal branch intersects the instability strip (which is not related to nuclear burning). Stars located in this narrow and almost vertical band, indicated by the two vertical dashed lines in Figure 1.5a, are unstable to radial

pulsation and are called *RR Lyrae variables*. Their luminosity correlates with both their period (several hours to ≈ 1 day) and their metallicity. Therefore, they are important for determining the distances to globular clusters and for establishing a cosmic distance scale (Binney and Merrifield, 1998). Increasing the metallicity has the overall effect of making a star fainter and cooler. Therefore, stars in metal-rich clusters or in the solar neighborhood (Figure 1.3) accumulate at the red end (right) of the horizontal branch, fairly independent of their envelope mass. This region is called the *red clump* (RC).

The metallicity argument also applies to the subdwarfs. These are main-sequence stars of very low metallicity. They are hotter than solar-metallicity stars at a comparable evolutionary stage and are thus located to the left of the main sequence that is occupied by metal-rich stars.

It should also be clear now why the upper part of the main sequence in Figure 1.3b is missing. Globular clusters are metal-poor and old, and do not form new stars. The high-mass stars that were originally located on the upper part of the main sequence evolved a long time ago into red giants. Only the slowly evolving low-mass stars are left today on the main sequence. With increasing time lower mass stars will eventually become red giants and the main sequence will become shorter. It is interesting that the age of the cluster can be determined from the location of the turn-off point, located at the top of the surviving portion of the main sequence. If the distance to the cluster is known by independent means, the luminosity of the stars at the turn-off point can be related to their mass. Stellar evolution models can predict the main-sequence lifetime of stars with a given mass, which must then be nearly equal to the age of the cluster. Such investigations yield ages for the most metal-poor (and presumably oldest) globular clusters of about 12–13 Gy, indicating that these objects formed very early in the history of the Galaxy. This estimate also represents an important lower limit on the age of the universe (Krauss and Chaboyer, 2003).

Initial Mass of $2\,M_\odot \lesssim M \lesssim 11\,M_\odot$

We can divide this mass range into several subranges. Stars with initial masses of $2\,M_\odot \lesssim M \lesssim 4\,M_\odot$ evolve faster than less massive stars and their tracks will look quantitatively different from the results shown in Figure 1.5a. But otherwise they evolve through the same stages as a solar-like star. A major difference, however, arises for stars with $M \gtrsim 2\,M_\odot$ since their helium cores during the red giant branch phase do not become electron degenerate. Therefore, a helium flash does not occur but instead helium ignites quiescently in the center. Subsequently, these stars make excursions to the left (toward higher temperatures) in the Hertzsprung–Russell diagram and some of them are liable to pass into the instability strip. The observational counterparts of these variable stars are called *classical Cepheids*. They are important for establishing a cosmic distance scale since their observed pulsation period is correlated with their luminosity.

Stars with initial masses of $M \gtrsim 4\,M_\odot$ experience an additional episode of mixing. Following helium exhaustion in the core, the structural readjustment to helium shell burning results in a strong expansion, such that the hydrogen

burning shell is extinguished as the star begins to ascend the early asymptotic giant branch (E-AGB). At this time, the base of the convective envelope penetrates the dormant hydrogen shell, and the products of hydrogen burning are mixed to the surface. This process is referred to as the *second dredge-up*. Afterward, the hydrogen shell reignites and the star continues to evolve up the asymptotic giant branch (AGB). Subsequently, during the interpulse period of the TP-AGB phase, the base of the convective envelope reaches down to the top of the hydrogen burning shell, where the temperature exceeds 50 MK. The ensuing nucleosynthesis is referred to as *hot bottom burning*. Because the envelope is fully convective, it is completely cycled through this burning region and the products of hydrogen burning will be enriched at the stellar surface.

The evolution of stars in the initial mass range of $9\,M_\odot \lesssim M \lesssim 11\,M_\odot$ is more complicated and less established at present. Models predict a number of important differences compared to the evolution of lower mass stars. We will discuss the evolution of a $10\,M_\odot$ star with initial solar composition as an example (Ritossa, García-Berro, and Iben, 1996). The star starts out by burning hydrogen in the core via the CNO cycles for about 10 million years. Following the exhaustion of hydrogen in its center, the star evolves toward the red giant branch where eventually the first dredge-up event occurs. Helium burning starts in the core under nondegenerate conditions and lasts for about 270 000 years. After helium exhaustion, the core contracts and heats up, and the outer layers of the star expand. Thereafter, the hydrogen burning shell extinguishes, while helium continues to burn in a shell surrounding a partially electron degenerate carbon–oxygen core. Eventually, the core becomes sufficiently hot for the fusion of carbon nuclei (*carbon burning*). When carbon ignites, the star enters the super asymptotic giant branch (SAGB). Carbon burning starts with a thermonuclear runaway (*carbon flash*) and the energy generation rate from carbon fusion increases greatly. The energy release causes the overlying layers to expand, giving rise to a reduction in the helium shell burning energy generation rate. After a relaxation period, the helium burning shell returns to its prior energy output. Several of these flashes occur over the carbon burning lifetime, which lasts for about 20 000 years. When carbon is exhausted in the center, the electron degenerate core consists mainly of oxygen and neon. After carbon burning extinguishes, the second dredge-up event occurs. Subsequently, the dormant hydrogen shell on top of the helium burning shell is reactivated and a complicated interplay between these two burning shells gives rise to thermal pulses driven by helium shell flashes. During this time, the third dredge-up event occurs. Eventually, the hydrogen-rich surface is removed by a strong stellar wind and the star becomes the central object of a planetary nebula. It ends its existence as an oxygen–neon white dwarf with a mass of $\approx 1.2\,M_\odot$.

Initial Mass of $M \gtrsim 11\,M_\odot$

The evolution of stars in this mass range is in many ways fundamentally different compared to our earlier discussion. Schematic evolutionary tracks for $13\,M_\odot$, $15\,M_\odot$, $20\,M_\odot$, and $25\,M_\odot$ stars are shown in Figure 1.5b. The case of a $25\,M_\odot$ star with initial solar composition will be discussed in the following as an example

(Chieffi, Limongi, and Straniero, 1998; Limongi, Straniero, and Chieffi, 2000; Woosley, Heger, and Weaver, 2002). The total life of such a massive star is relatively short and amounts only to ≈ 7 My. The star spends 90% of this time on the main-sequence burning hydrogen to helium via the CNO cycles in the core. When the hydrogen in the center is exhausted, hydrogen burning continues in a shell. The core contracts and heats up until helium is ignited. This new source of nuclear energy heats the overlying hydrogen shell and the outer layers of the star expand greatly. The star becomes a supergiant. These stars show up in the Hertzsprung–Russell diagram at the highest observed luminosities. Examples are Rigel (blue supergiant) and Betelgeuse (red supergiant) in the constellation Orion.

Core helium burning lasts for about 800 000 years and some of the heavy nuclides with masses of $A > 60$ are synthesized during this stage via neutron captures (s-process; Section 5.6.1). When helium is exhausted in the center, helium burning continues in a shell located beneath the hydrogen burning shell. Eventually, carbon burning starts in the core. These burning stages have already been discussed above.

Stars with initial masses exceeding $\approx 11\,M_\odot$ are capable of igniting successive burning stages in their cores using the ashes of the previous core burning stage as fuel. Three distinct burning stages follow carbon burning. They are referred to as *neon burning*, *oxygen burning*, and *silicon burning*, and will be discussed in detail in Section 5.3. There is a fundamental difference between the initial and the advanced burning stages in the manner by which the nuclear energy generated in the stellar interior is transformed and radiated from the surface. For hydrogen and helium burning, nuclear energy is almost exclusively converted to light. During the advanced burning stages energy is almost entirely radiated as neutrino–antineutrino pairs and the light radiated from the star's surface represents only a very small fraction of the total energy release. Since the neutrino losses increase dramatically during the advanced burning stages and because the nuclear burning lifetime scales inversely with the total luminosity, the evolution of the star rapidly accelerates. For example, silicon burning will last for only about one day. Since the advanced burning stages transpire very quickly, the envelope has insufficient time to react to the structural changes in the stellar interior. Thus, from carbon burning onward, the star will no longer move in the Hertzsprung–Russell diagram, but remains at the position indicated by the solid circle in Figure 1.5b. Furthermore, since the star spends most of its life burning either hydrogen or helium in the core, these are typically the only phases that we can observe.

The approximate structure of the massive star after silicon has been exhausted in the core is shown in Figure 1.7 (left side). The star consists now of several layers of different composition that are separated by thin nuclear burning shells. The details of the nucleosynthesis are complicated and will be discussed in Chapter 5. It is sufficient to mention at this point that the heaviest and most stable nuclei (i.e., the iron peak nuclei; Section 1.3) are found in the core. Also, the luminosity during the red giant phase is so large that the star undergoes a significant mass loss. The effect is more pronounced for stars with $M \gtrsim 30$–$35\,M_\odot$ that lose eventually most of their hydrogen envelope. The observational counterparts of such stars are the

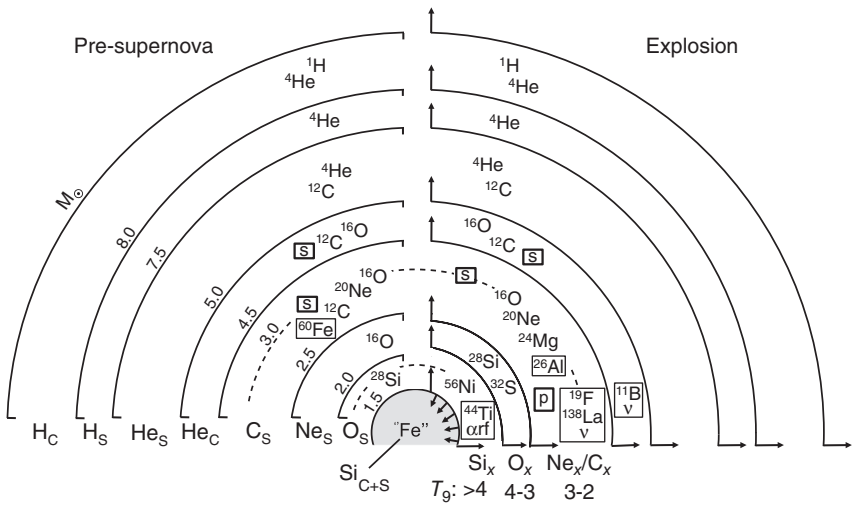

Figure 1.7 Structure and evolution of a $25M_\odot$ star of solar metallicity, as predicted by one-dimensional, spherically symmetric models (Limongi, Straniero, and Chieffi, 2000), shortly before and after core collapse (not to scale). Only the main constituents in each layer are shown. Minor constituents, among them important γ-ray emitters, are set in thin rectangles. Various processes are set in thick rectangles: weak s-process component (s); p-process (p); α-rich freeze-out (αrf); ν-process (ν). (Left) Snapshot of pre-supernova structure. Nuclear burning takes place in thin regions (burning shells) at the interface of different compositional layers, where each burning shell migrated outward to the position indicated by the black lines. The compositions result from burning stages indicated at the bottom (subscripts *C* and *S* stand for core and shell burning, respectively). The diagonally arranged numbers indicate the interior mass (in solar masses) for each burning shell. (Right) Explosive nucleosynthesis resulting from the passage of the shock wave through overlying layers, giving rise to explosive burning of silicon (Si_x), oxygen (O_x) and neon-carbon (Ne_x/C_x). Strictly speaking, this classification depends on the temperature range, not on the available fuel. Nevertheless, the names indicate approximately which compositional layers of the presupernova will usually be affected. Outside the outer dashed line, the composition is little altered by the shock. The inner dashed line indicates the approximate boundary of the part of the star that is ejected (mass cut). This model is sometimes referred to as the *onion shell structure* of a massive star.

hot and massive *Wolf–Rayet stars*, which have been observed to lose mass at a rate of $\approx 10^{-5}\,M_\odot$ per year at stellar wind speeds of ≈ 2000 km/s. An image of a Wolf–Rayet star is shown in color Figure 5 on page 617.

The electron degenerate stellar core has at this point no other sources of nuclear energy to its disposal and grows in mass as the overlying burning shells contribute more nuclear ashes. When the mass of the core reaches the Chandrasekhar limit ($\approx 1.4\,M_\odot$), the electron degeneracy pressure is unable to counteract gravity, and the core collapses freely at about a quarter of the speed of light. When the density reaches values on the order of the nuclear density ($\rho \approx 10^{14}$ g/cm^3), the nuclei and free nucleons begin to feel the short-range nuclear force, which is repulsive

at very short distances. The collapsing inner core reaches high inward velocities and overshoots the nuclear density. The nuclear potential acts as a stiff spring that stores energy in the compressive phase until it rebounds. The rebounding part of the core encounters infalling matter and thus gives rise to an outward moving prompt shock wave. The hot and dense inner core has become a proto-neutron star with a mass of $\approx 1.5\,M_\odot$. While the shock wave moves outward through the outer core region, it loses energy by photodisintegrating the iron peak nuclei. Furthermore, energy is removed from the shock wave by the emission of neutrinos. It takes about 1 s after core collapse, and about 10 ms after the core has bounced, for the shock wave to reach the outer edge of the core. At this time, the shock wave has lost all of its kinetic energy and it stalls. How exactly the shock is revived and how it will ultimately propagate through the stellar layers beyond the iron core and disrupt the star in a core-collapse supernova explosion is among the most elusive problems in nuclear astrophysics. We will discuss this issue in Section 5.4.

Once the shock wave is revived, it moves through the star and heats matter to high temperatures for a time period of seconds. Subsequently, the hot and dense matter expands nearly adiabatically. As a result, the star experiences several episodes of *explosive nuclear burning*. The silicon (^{28}Si) and oxygen (^{16}O) in the first layers the shock wave encounters are quickly converted to iron peak and intermediate-mass nuclei at high temperatures ($\approx$ 3–5 GK). As will be shown later, the nuclide $^{56}_{28}\mathrm{Ni}_{28}$ is among the most abundant products originating from these layers. Some other important nuclides are synthesized by the shock in other layers, among them the ^{26}Al observed in the interstellar medium (Section 1.7.5 and color Figure 12 on page 624). The character of the explosive nuclear burning depends, among other things, on the location of the shock and the expansion time scale. During the explosion nuclides that have been synthesized before and after the core collapse are ejected and are then mixed into the interstellar medium. Several nuclear processes that occur during the explosion are indicated in Figure 1.7 (right side) and will be discussed in more detail in Chapter 5.

Stellar model simulations support the idea that supernovae of type II and type Ib/Ic are the observational counterparts of the core collapse in massive stars. The different supernova types are classified observationally according to their optical spectra. Spectra of type II supernovae contain hydrogen lines, while those of type I supernovae do not. Type I supernovae whose spectra show absorption caused by the presence of silicon are referred to as *type Ia supernovae*; otherwise they are classified as type Ib or Ic supernovae (the latter distinction is based on a helium line feature in the spectrum). Type II supernovae tend to occur in the arms of spiral galaxies, but not in early-type galaxies (elliptical galaxies) that lack gas and show very low levels (if any) of star formation. Type Ib or Ic supernovae also seem to occur in spiral arms. On the other hand, type Ia supernovae show no such preference. Since the spiral arms contain many massive, and thus young, stars and elliptical galaxies only contain old stellar populations (with ages of $\approx 10^{10}$ y), the observations suggest that massive stars are the progenitors of type II and type Ib/Ic supernovae, but not of type Ia supernovae. Stars with initial masses of $M \lesssim 20$–$30\,M_\odot$ explode as a type II supernova and form a neutron star

as a remnant. Stars with masses above this range (Wolf-Rayet stars), or less massive stars in binaries, that have lost their hydrogen envelopes are thought to be the progenitors of type Ib and Ic supernovae. It is not clear at present if the latter explosions leave a neutron star or a black hole behind as a remnant, mainly because of our incomplete knowledge of post-main sequence mass loss and the details of fall-back of matter onto the central object. As will become clear in Chapter 5, core-collapse supernovae are of outstanding importance for three reasons: (i) they are predicted to be among the most prolific sources of element synthesis in the Galaxy; (ii) they are the sites where neutron stars are born; and (iii) they are a likely source of shock waves that are believed to accelerate Galactic cosmic rays (Section 5.7.2).

We still lack self-consistent models of core-collapse supernovae. Therefore, many current stellar models induce the shock wave artificially by depositing a given amount of energy somewhere near the iron core. The models are constrained by observation. In particular, observations of supernova 1987A, which exploded in the Large Magellanic Cloud in 1987, were of outstanding importance in this regard (see color Figure 6 on page 618). Since it was located so close to us, the event could be studied in greater detail than any other supernova. Observations of supernova 1987A and other type II supernova light curves estimate explosion energies of $\approx (1–2) \times 10^{44}$ J and, therefore, strongly constrain the magnitude of artificial energy deposition in the models. The location of artificial energy deposition is also constrained by observation: it can neither be located inside the iron core or otherwise neutron-rich iron group nuclides are overproduced, nor can it be located beyond the oxygen burning shell or the resulting neutron star mass, after fall-back of matter, will be too large. In most simulations, the *mass cut*, that is, the boundary between ejected and fall-back matter, is located in the silicon layer (inner dashed line on right side of Figure 1.7).

Current stellar models of core-collapse supernovae agree with observation in many respects. For example, a burst of neutrinos had long been predicted by theory and was detected for supernova 1987A (Section 1.4.1). Furthermore, current models reproduce the amount of the ejected radioactive ^{56}Ni that, after first decaying to ^{56}Co and then to stable ^{56}Fe, gives rise to the tail in the light curves of core-collapse supernovae. A famous type II supernova remnant, the Crab Nebula, is shown in color Figure 7 on page 619.

The supernova rate in our Galaxy amounts to ≈ 3 events per century, with an estimated systematic uncertainty of a factor of two (Li *et al.*, 2011b). For a volume-limited sample, within a radius of about 70 Mpc in the local universe, the observed fractions of supernovae of type II, Ia, and Ib/c are 57%, 24%, and 19%, respectively (Li *et al.*, 2011a). Type Ia supernovae will be discussed below.

1.4.4 Binary Stars

Perhaps as many as one half of all stars are members of binary star systems. If the stars are members of a close binary system, then they will significantly influence

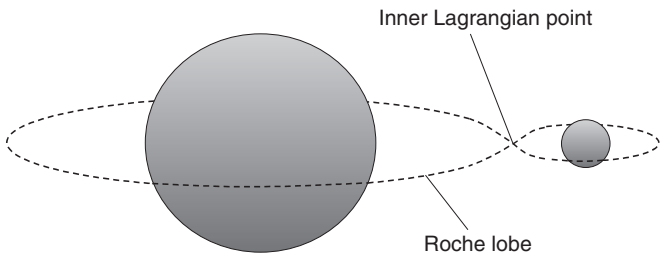

Figure 1.8 Binary star system. Each star is surrounded by a hypothetical surface, called the *Roche lobe*, that marks its gravitational domain. The intersection of the equatorial plane with the Roche lobes is shown as a dashed curve. The location where the two Roche lobes touch is called the *inner Lagrangian point*.

each other's evolution. In a close binary system, the separation may range from a few times the radii of the stars to a situation where both stars share a common envelope (*contact binaries*). Consider the binary star system shown in Figure 1.8. Each star is surrounded by a hypothetical surface marking its gravitational domain. This surface is referred to as the *Roche lobe* and its intersection with the equatorial plane is shown as a dashed figure-eight curve. The location where the two Roche lobes touch, that is, where the effects of gravity and rotation cancel each other, is called the *inner Lagrangian point*. When one of the stars evolves off the main sequence and becomes a red giant, it may fill its Roche lobe. Material is then free to flow from that star through the inner Lagrangian point onto its companion. Many different kinds of stars may be members of close binary systems and the transfer of mass from one star to another gives rise to very interesting phenomena (Iben, 1991). In the following we will focus on binary systems that contain a compact object, either a white dwarf or a neutron star.

Type Ia Supernovae

Type Ia supernovae are the brightest phenomena powered by nuclear energy release in the universe and they sometimes outshine their host galaxies. The observed mean velocities of the ejecta are of order 10 000 km/s, corresponding to kinetic energies of $\approx 10^{44}$ J. An image of the type Ia supernova 1994D is shown in color Figure 9 on page 621. Recall that type Ia supernovae occur in both early-type galaxies (elliptical galaxies) and spiral galaxies. The former show very low levels (if any) of star formation and all supernovae observed so far in elliptical galaxies are of type Ia. In spiral galaxies, the type Ia rate is positively correlated with the star formation rate. Therefore, type Ia supernovae are likely associated with older stellar populations and with stars of moderate mass. Their light curves are powered by the decay of radioactive ^{56}Ni to ^{56}Co, followed by the decay of ^{56}Co to stable ^{56}Fe. The inferred amount of ^{56}Ni synthesized in type Ia supernovae is $\approx 0.6\,M_{\odot}$ per event, significantly higher than the amount observed in type II supernovae (Section 5.4.4).

We already mentioned that type Ia supernovae are classified according to their spectra near maximum light: they lack hydrogen and helium lines, but contain an absorption feature caused by the presence of Si. During the peak phase, other intermediate-mass elements (O, Mg, S, Ca) are also observed in their spectra, together with contributions from Fe and Co. With progressing time, the relative contribution of the iron-peak elements increases. About two weeks after peak luminosity, the spectra are dominated by Fe, although Si and Ca lines are still present. The observations indicate that the thermonuclear explosion gave rise to the synthesis of intermediate-mass elements in the outer layers, which become visible early during the peak phase, and to the synthesis of iron-peak elements in the deeper layers, which become visible a few weeks later.

Type Ia supernovae are fascinating objects in their own right, but a deeper understanding of the explosion is crucial both for Galactic chemical evolution and for cosmology. About 70% of observed type Ia supernovae (Li *et al.*, 2011a) show a remarkably small spread in peak brightness. Supernova 1994D, for example, belongs to this class of *normal* type Ia supernovae. When the light curves of all type Ia supernovae are compared, including both normal and peculiar events, it is found that the peak luminosities correlate with the post-peak decline rate of the light curves (Phillips, 1993). This correlation can be used to compensate for the peak luminosity spread and, therefore, the intrinsic brightness can be determined to within a narrow range. By measuring their apparent luminosity it becomes hence possible to estimate their distance. Since type Ia supernovae are so bright, they can be observed across billions of light years. For these reasons, type Ia supernovae are used as *cosmological distance indicators*. By recording both their apparent luminosity and their redshifts, observations of very distant type Ia supernovae provide a measure for the expansion history of the universe. The surprising finding that the expansion is accelerating, driven by the elusive *dark energy* (Riess *et al.*, 1998; Perlmutter *et al.*, 1999), is an observation of paramount importance for cosmology.

The observed variation in peak luminosity among the majority of type Ia supernovae can be interpreted as a consequence of a single parameter, that is, the different amounts of ^{56}Ni synthesized during the thermonuclear explosion (Arnett, 1982). The more ^{56}Ni is produced, the larger the peak brightness. At the same time, expansion velocities are larger and the light curve becomes broader since the opacity increases with a higher concentration of iron-peak elements.

With an increasing number of type Ia supernovae discovered, it is now clear that they represent a class of some diversity and that their properties cannot be fully explained by a single parameter. For example, there is a spread in the expansion velocities at the photospheres even for similarly bright events. Furthermore, some peculiar type Ia supernovae of exceptionally high or extremely low luminosity do not obey the Phillips relation. These observations indicate that different type Ia supernovae may be caused by different progenitor systems. Furthermore, the Phillips relation is based on a sample of low redshift supernovae. It is concerning that systematic differences in the properties of local and high-redshift type Ia supernovae may exist, which could lead to erroneous cosmological distances.

The profound cosmological implications strongly motivate the identification and understanding of type Ia supernova progenitors.

Many different stellar models have been proposed to explain type Ia supernovae, but we are still lacking a satisfactory understanding. A common feature of all viable progenitor systems is a thermonuclear explosion of a carbon-oxygen white dwarf, which is initiated when the pressure and temperature become sufficient to fuse carbon (Hoyle and Fowler, 1960). As a result, a significant fraction of the initial carbon and oxygen is burned to ^{56}Ni, with a predicted nuclear energy release of $\approx 10^{44}$ J. About two thirds of this energy is invested in the kinetic energy of the expanding debris, in agreement with observation. The remaining fraction is responsible for disrupting the white dwarf at high velocity within a time scale of seconds (*thermonuclear supernovae*). An example is Tycho's supernova remnant (SN 1572), shown in color Figure 10 on page 622, where no compact remnant has been found, supporting the idea that the supernova was of type Ia. The conjecture of a primary white dwarf is also supported by observational constraints (Bloom *et al.*, 2012) obtained for the *normal* type Ia supernova SN 2011fe that was discovered in the Pinwheel galaxy (M 101).

All of these models include a companion (secondary) star that supplies mass to the (primary) white dwarf. When the Chandrasekhar limit ($\approx 1.4\,M_\odot$) is approached, carbon ignites under degenerate conditions. A thermonuclear runaway ensues because the temperature increase from the nuclear burning does not create an increase in pressure, and the temperature continues to increase until the degeneracy is lifted. At this point, the energy generation rate is so large that an explosion occurs. Stellar model simulations have also shown that the white dwarf must be composed mainly of ^{12}C and ^{16}O, instead of ^{16}O and ^{20}Ne (see Figure 1.4). In the latter case, the temperature during mass accretion toward the Chandrasekhar limit never becomes high enough to ignite oxygen or neon, and the result is most likely a core collapse instead of a thermonuclear supernova.

The nature of the secondary star is a matter of dispute. In the proposed single-degenerate scenario, the secondary is a main-sequence star, a red giant, or a helium star, whereas the double-degenerate scenario involves the merger of two white dwarfs as a result of angular momentum loss caused by gravitational wave emission. Both scenarios have difficulties in reproducing key observational features of type Ia supernovae. In the single-degenerate model, the companion star will survive the explosion. On the other hand, no remnant is left behind in the double-degenerate model. One way to distinguish between these models is to search for surviving companion stars near the centers of type Ia supernova remnants. However, the suggestion that Tycho G (a solar-like star) is the likely companion for SN 1572 (Ruiz-Lapuente *et al.*, 2004) is controversial at present.

Another important unresolved issue is related to the propagation of the thermonuclear burning front in the interior of the primary white dwarf. Two burning modes can be distinguished. One possibility is a detonation in which the nuclear flame propagates as a supersonic front. In this case, the flame compresses the

material and increases the temperature to the point of ignition. The energy release from the ignited material behind the flame supports its propagation. Another possibility is a deflagration in which the nuclear burning proceeds subsonically. Here, the heat released from nuclear burning is conducted by electrons and ignites the next layer, causing the white dwarf to expand. The observation of intermediate-mass elements in the spectra of type Ia supernovae rules out a pure detonation regime since it would prevent the expansion of the layers ahead of the burning front, giving most likely rise to the synthesis of iron-peak elements only. These two burning modes are not exclusive and a transition from one mode to another may occur. For example, a burning front could propagate via deflagration, causing the white dwarf to pre-expand, and may then transition by some, yet not understood, mechanism to a detonation (*delayed detonation*). The outcome depends on the density, temperature, chemical composition, and the velocity profiles at the time of ignition. Related to this issue is the question of where precisely, near or off center and at how many locations, the ignition occurs.

We will discuss the nucleosynthesis in type Ia supernovae in more detail in Section 5.5.1. More information on the progenitors of type Ia supernovae, including a discussion of sub-Chandrasekhar models and white dwarf collisions that may explain peculiar events, can be found in the reviews by Wang and Han (2012) and Höflich *et al.* (2013).

Classical Novae

Classical novae are stellar explosions that occur in close binary systems. In this case, hydrogen-rich matter is transferred via Roche lobe overflow from a low-mass main-sequence star to the surface of a compact white dwarf. The transferred matter does not fall directly onto the surface but is accumulated in an accretion disk surrounding the white dwarf. Typical accretion rates amount to $\approx 10^{-10}$–$10^{-9}\,M_\odot$ per year. A fraction of this matter spirals inward and accumulates on the white dwarf surface, where it is heated and compressed by the strong surface gravity. At some point, the bottom layer becomes electron degenerate. Hydrogen starts to fuse to helium (via the pp chains) during the accretion phase and the temperature increases gradually. The electron degeneracy prevents an expansion of the envelope and eventually a thermonuclear runaway occurs near the base of the accreted layers. At this stage, the nuclear burning is dominated by explosive hydrogen burning via the (hot) CNO cycles. Both the compressional heating and the energy release from the nuclear burning heat the accreted material until an explosion occurs.

The classical nova rate in the Galaxy is about ≈ 35 per year and thus they occur more frequently than supernovae (Section 1.4.3). Contrary to type Ia supernovae, which disrupt the white dwarf, all classical novae are expected to recur with periods of $\approx 10^4$–10^5 years. The luminosity increase during the outburst amounts to a factor of $\approx 10^4$. A classical nova typically ejects $\approx 10^{-5}$–$10^{-4}\,M_\odot$ of material, with mean ejection velocities of $\approx 10^3$ km/s. Also, there are other types of novae, such as dwarf novae or nova-like variables. However, these are not related to thermonuclear burning.

Optical, infrared, and ultraviolet spectra of classical novae reveal the presence of many elements in the expanding nova shells that are strongly overabundant compared to solar system values. For example, the observed overabundances of carbon and oxygen in all classical novae demonstrate that at some time during the evolution of the outburst the accreted material must have been mixed to a certain degree with matter from the white dwarf. This dredge-up of material gives rise to a more energetic explosion (by increasing the number of CNO catalyst nuclei; Section 5.5.2). The observation of an overabundance of neon in some classical novae showed that these outbursts do not involve a carbon–oxygen white dwarf, but a more massive white dwarf of oxygen–neon composition. The latter objects result from the evolution of intermediate mass stars with initial masses of $9\,M_\odot \lesssim M \lesssim 11\,M_\odot$ (Figure 1.4). The presence of large amounts of matter from the white dwarf core in the ejecta may imply that the white dwarf in a classical nova system is losing mass as a result of subsequent outbursts. Thus, these objects are unlikely to become progenitors of type Ia supernovae. Other observed overabundances, for example, of nitrogen, silicon, or sulfur, are the result of nuclear processing during the explosive burning of hydrogen. An image of Nova Cygni 1992 is shown in color Figure 11 on page 623.

Stellar model calculations indicate that the peak phase of explosive nuclear burning in classical novae lasts typically for several hundred seconds. The characteristics of the outburst depend on the white dwarf mass and luminosity, the mass accretion rate, and the chemical composition for both the accreted and the white dwarf material. For example, it has been demonstrated that the lower the mass accretion rate, the larger the amount of accreted mass before the thermonuclear runaway is initiated. A more massive accreted layer, in turn, gives rise to a higher pressure in the bottom layers and hence a more violent explosion. On the other hand, if a too large accretion rate is assumed, no thermonuclear runaway is initiated. Simulations also indicate that classical nova outbursts on the surface of the heavier oxygen–neon white dwarfs achieve higher peak temperatures than those exploding on carbon–oxygen cores. For more information on classical novae, see José, Hernanz, and Iliadis (2006) and Starrfield, Iliadis, and Hix (2006).

Type I X-Ray Bursts

A number of close binary star systems involve a neutron star as a compact object. A neutron star has a mass of $\approx 1.4\,M_\odot$, a radius of about 10–15 km, and a density of order 10^{14} g/cm^3. These binary star systems belong to a class of objects that are called *X-ray binaries*. The accretion of matter from the companion on the surface of the neutron star gives rise to a large gravitational energy release. As a result, the temperatures near the neutron star surface are high ($\approx 10^7$ K) and the persistent thermal emission occurs at X-ray energies.

In high-mass X-ray binaries, the companion is a massive ($\gtrsim 5\,M_\odot$) population I star, while the neutron star has a strong magnetic field. The matter is accreted at relatively high rates and is funneled along the magnetic field lines onto the

magnetic poles. This creates a hot spot of X-ray emission and, if the rotational axis of the neutron star is inclined with respect to the magnetic axis, this gives rise to an X-ray pulsar. Typical rotation periods range from 0.1 s to a fraction of an hour. The rotational periods for some X-ray pulsars have been observed to decrease, indicating that the neutron stars spin up as a result of accretion of matter.

In low-mass X-ray binaries, the companion is a low mass ($\lesssim 1.5\,M_\odot$) population II star and matter is transferred to a weakly magnetized neutron star via Roche lobe overflow. Many of these systems produce, apart from the persistent X-ray emission, bursts in the X-ray intensity (Lewin, van Paradijs, and Taam, 1993). For a rare variety, called *type II X-ray bursts*, the bursts occur in rapid succession and are separated by a few minutes. The profile of each burst rises and falls abruptly. They are most likely associated with a sudden increase in the mass transfer rate caused by instabilities in the accretion disk.

The large majority of bursts belong to the class of type I X-ray bursts. In this case, the X-ray luminosity typically increases by an order of magnitude. They are believed to be of thermonuclear origin, unlike the X-ray binary varieties discussed above. When hydrogen- and helium-rich matter from the low-mass companion is first accreted in a disk and then falls onto the surface of the neutron star, the temperatures and densities are high enough to fuse hydrogen continuously to helium via the (hot) CNO cycles. The accreted or synthesized helium, however, is not fusing yet but sinks deeper into the neutron star atmosphere. Eventually the helium is ignited via the triple-α reaction under electron degenerate conditions and a thermonuclear runaway occurs. The helium flash triggers the explosive burning of the outer region consisting of a mixture of hydrogen and helium. This is just one possible scenario. In other models the ignition occurs in pure helium or in mixed hydrogen–helium accreted material. The details of the nucleosynthesis depend on the temperatures and densities achieved in the various burning layers. Calculations show that in the innermost and hottest layers elements up to – and perhaps beyond – the iron peak are synthesized. After the termination of a burst, a new shell of matter is accreted and the cycle repeats.

The above model explains the basic features of type I X-ray bursts. A burst lasts typically for < 1 min and repeats after several hours to days. The luminosity profile shows a rapid rise within $\approx$ 1–10 s, caused by the sudden nuclear energy release, and a slower decline of order $\approx$ 5–100 s, reflecting the cooling of the neutron star surface. Some bursts show millisecond oscillations of the X-ray flux. These have been suggested to arise from a surface wave in the nuclear burning layer or perhaps from anisotropies in the nuclear burning caused by a spreading hot spot on the surface of a rapidly spinning neutron star.

Stellar models of type I X-ray bursts are sensitive to a number of parameters and assumptions, such as the mass accretion rate, rotation, the number of ignition points, the propagation of the burning front across the neutron star surface, and the composition of the accreted matter.

It is unlikely for any significant amount of accreted and processed matter to escape the large gravitational potential of the neutron star. Therefore, type I X-ray bursts are probably not important contributors to the chemical evolution of the Galaxy. They are important, however, for probing the properties of neutron stars, such as the mass, radius, and the composition. For more information, see Parikh *et al.* (2013a), and references therein.

1.5
Masses, Binding Energies, Nuclear Reactions, and Related Topics

1.5.1
Nuclear Mass and Binding Energy

The most fundamental property of the atomic nucleus is its mass. Early mass measurements showed that the total nuclear mass, $m_{\rm nuc}$, is less than the sum of masses of the constituent nucleons. We may write

$$m_{\rm nuc} = Zm_{\rm p} + Nm_{\rm n} - \Delta m \tag{1.1}$$

According to the Einstein relationship between mass and energy, the *mass defect* Δm is equivalent to an energy of $\Delta E = \Delta m \cdot c^2$. The quantity ΔE is referred to as *nuclear binding energy*. It is defined as the energy released in assembling a given nucleus from its constituent nucleons, or equivalently, the energy required to separate a given nucleus into its constituent nucleons. We may express the binding energy as

$$B(Z,N) = \left(Zm_{\rm p} + Nm_{\rm n} - m_{\rm nuc}\right) c^2 \tag{1.2}$$

A plot of experimental binding energies per nucleon, $B(Z,N)/A$, for the most tightly bound nuclide at each mass number A is shown in Figure 1.9a. An expanded region is displayed in part (b), where the round symbols have the same meaning as in the part (a). Most of these nuclides, which are stable in the laboratory, have binding energies between 7 and 9 MeV per nucleon. Nuclides with mass numbers in the range of $A = 50$–65 have the largest binding energies per nucleon. They are the iron peak species, which we already encountered in Section 1.3. It appears that nature favors the synthesis of the most tightly bound and most stable nuclides, as will be explained in detail in later chapters. The most tightly bound nuclides of all are ^{62}Ni, ^{58}Fe, and ^{56}Fe with binding energies per nucleon of $B(Z,N)/A = 8794.546 \pm 0.008$ keV, 8792.239 ± 0.008 keV, and 8790.342 ± 0.008 keV, respectively (Wang *et al.*, 2012). Lighter or heavier nuclei are less tightly bound. The square symbols in the bottom part refer to $N = Z$ nuclides above $A = 40$, which are all radioactive. The most tightly bound $N = Z$ species is ^{56}Ni, with a binding energy per nucleon of $B(Z,N)/A = 8642.767 \pm 0.010$ keV. It follows that nuclear processes liberate energy as long as the binding energy per nucleon of the final products exceeds

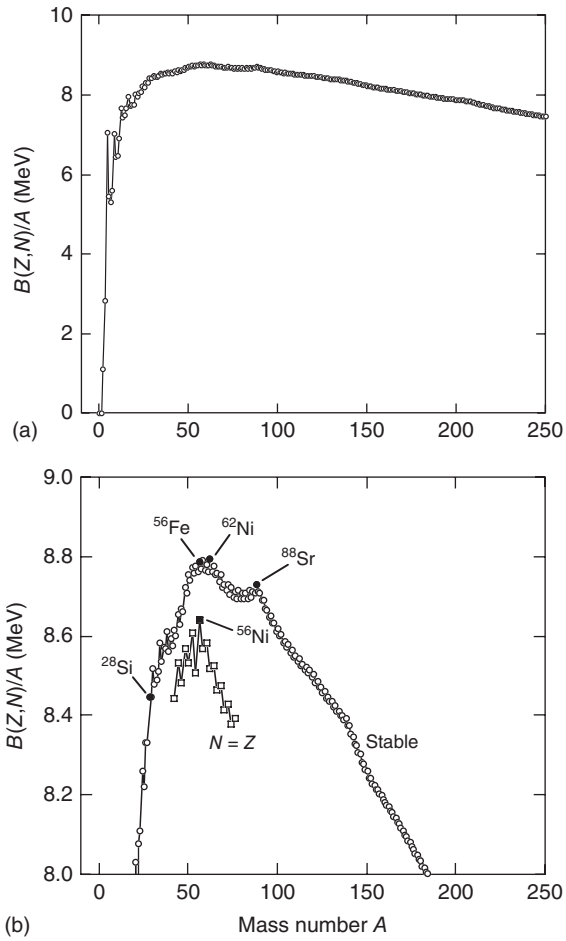

Figure 1.9 Experimental binding energy per nucleon, $B(Z,N)/A$, versus mass number, A. (a) Value of $B(Z,N)/A$ for the most tightly bound nuclide at a given mass number A. (b) Expanded section; the round symbols have the same meaning as in part (a), that is, they correspond to the most tightly bound nuclide of a given mass number; the nuclide with the largest binding energy per nucleon is ^{62}Ni ($B/A = 8.795$ MeV); the square symbols show $B(Z,N)/A$ values for $N = Z$ nuclides above $A = 40$, which are all radioactive; the $N = Z$ species with the largest binding energy per nucleon is ^{56}Ni ($B/A = 8.643$ MeV). Data from Wang *et al.* (2012).

the binding energy per nucleon of the initial constituents. Consequently, nuclear energy can be liberated by the fusion of nuclei lighter than iron, or by the fission of nuclei heavier than iron. For example, if a star consists initially of pure hydrogen (^{1}H), an energy of ≈ 7 MeV per nucleon can be liberated by fusing hydrogen to helium (^{4}He), or almost 9 MeV per nucleon is liberated by fusing hydrogen to ^{56}Fe.

Example 1.2

The binding energies per nucleon of deuterium (^{2}H or d) and helium (^{4}He or α) are given by $B(\mathrm{d})/A = 1.112$ MeV and $B(\alpha)/A = 7.074$ MeV. Calculate the energy released when two deuterium nuclei are combined to form one ^{4}He nucleus.

First, we calculate the binding energies of deuterium and ^{4}He:

$$B(\mathrm{d}) = \frac{B(\mathrm{d})}{A}A = (1.112\,\mathrm{MeV}) \cdot 2 = 2.224\,\mathrm{MeV}$$
$$B(\alpha) = \frac{B(\alpha)}{A}A = (7.074\,\mathrm{MeV}) \cdot 4 = 28.296\,\mathrm{MeV}$$

By combining two deuterium nuclei to one ^{4}He nucleus, the total energy release amounts to

$$(28.296\,\mathrm{MeV}) - (2.224\,\mathrm{MeV}) - (2.224\,\mathrm{MeV}) = 23.85\,\mathrm{MeV}$$

corresponding to a value of 5.96 MeV per nucleon.

1.5.2 Energetics of Nuclear Reactions

A nuclear interaction may be written symbolically as

$$0 + 1 \rightarrow 2 + 3 \qquad \text{or} \qquad 0(1,2)3 \tag{1.3}$$

where 0 and 1 denote two colliding nuclei before the interaction, while 2 and 3 denote the interaction products. Most nuclear interactions of astrophysical interest involve just two species before and after the interaction. If species 0 and 1 are identical to species 2 and 3, then the interaction is called *elastic* or *inelastic* scattering. Otherwise, the above notation refers to a *nuclear reaction*. Photons may also be involved in the interaction. If species 2 is a photon, then the interaction is called *radiative capture reaction*. If species 1 is a photon, then we are considering a *photodisintegration reaction*. All of these interactions will be discussed in later chapters.

Figure 1.10 shows schematically the energetics of nuclear reactions and can be used to illustrate a number of relationships that will be employed frequently in the following chapters. The vertical direction represents energy. Consider Figure 1.10a, showing a reaction $0 + 1 \rightarrow 2 + 3$, where all species involved in the interaction are particles with rest mass. The rest masses of 0 and 1 (before the reaction) and of 2 and 3 (after the reaction) are indicated by horizontal solid lines. The total relativistic energy in a nuclear reaction must be conserved. Thus, one may write

$$m_0c^2 + m_1c^2 + E_0 + E_1 = m_2c^2 + m_3c^2 + E_2 + E_3 \qquad \text{or}$$
$$Q_{01\rightarrow 23} \equiv m_0c^2 + m_1c^2 - m_2c^2 - m_3c^2 = E_2 + E_3 - E_0 - E_1 \tag{1.4}$$

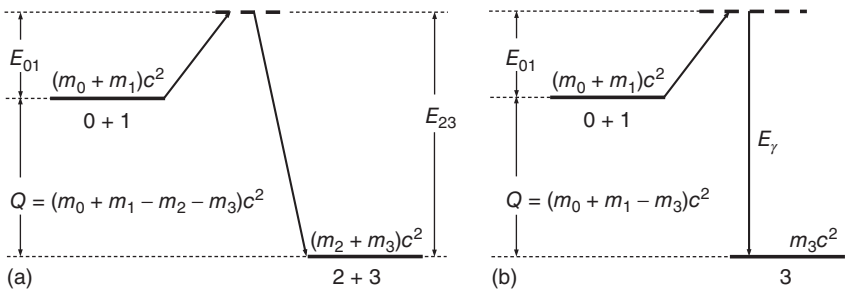

Figure 1.10 Energy level diagrams to illustrate the energetics of nuclear reactions. The vertical direction represents an energy scale. Part (a) corresponds to a situation where all species participating in the reaction are particles with rest mass. In part (b) one of the species is a photon.

where E_i are kinetic energies and m_i are rest masses. The difference in masses before and after the reaction, or the difference in kinetic energies after and before the reaction, is equal to the energy release and is referred to as the *reaction Q-value*. If Q is positive, the reaction releases energy and is called *exothermic*. Otherwise the reaction consumes energy and is called *endothermic*. Apart from a few exceptions, the most important nuclear reactions in stars are exothermic ($Q > 0$). Equation (1.4) is applicable in any reference frame. The difference between center-of-mass and laboratory reference frame is discussed in Appendix C. The quantities E_{01} and E_{23} in Figure 1.10a represent the total kinetic energies in the center-of-mass system before and after the reaction, respectively. It is apparent that the center-of-mass kinetic energies and the Q-value are related by

$$E_{23} = E_{01} + Q_{01\to 23} \tag{1.5}$$

Figure 1.10b shows a radiative capture reaction $0 + 1 \to \gamma + 3$. In this case we find accordingly

$$\begin{aligned} &m_0c^2 + m_1c^2 + E_0 + E_1 = m_3c^2 + E_3 + E_\gamma \qquad \text{or} \\ &Q_{01\to\gamma 3} \equiv m_0c^2 + m_1c^2 - m_3c^2 = E_3 + E_\gamma - E_0 - E_1 \end{aligned} \tag{1.6}$$

Center-of-mass kinetic energies and the Q-value are now related by

$$E_{\gamma 3} = E_{01} + Q_{01\to\gamma 3} \tag{1.7}$$

where $E_{\gamma 3}$ denotes the sum of the energy of the emitted photon (E_γ) and the center-of-mass kinetic energy of the recoil nucleus 3. The latter contribution is usually very small so that one can frequently set $E_{\gamma 3} \approx E_\gamma$ (see Appendix C).

The reaction Q-value for a radiative capture reaction is equal to the energy released when nuclei 0 and 1 combine to form a composite nucleus 3. If one would add this very same amount of energy to nucleus 3, then it becomes energetically possible for nucleus 3 to separate into the fragments 0 and 1. Thus,

the *particle separation energy* of nucleus 3 is equal to the Q-value of the reaction $0 + 1 \rightarrow \gamma + 3$, that is, $S_{3\rightarrow 01} = Q_{01\rightarrow\gamma 3}$. Separation energies will be used frequently in the following chapters. Their values depend on the nuclear properties of species 0, 1, and 3. For example, suppose we start out with a stable nucleus in Figure 1.1 and remove one neutron at a time. As a result, we move in the chart of the nuclides to the left toward increasingly proton-rich nuclei. The farther we move away from the group of stable nuclei, the larger the proton–neutron imbalance becomes, and the less energy is required to remove a proton from a given nucleus. In other words, the proton separation energy S_p decreases. After a certain number of neutrons have been removed, a nuclide is eventually reached for which S_p becomes negative. Such nuclides are called *proton unstable* since they decay via the emission of a proton. The line in the chart of the nuclides with $S_p = 0$ (on the proton-rich side) is referred to as *proton dripline*. Similarly, if we remove from a given stable nucleus protons instead of neutrons, then we would move in the chart of the nuclides downward. The neutron–proton imbalance increases while the neutron separation energy S_n decreases with each removal of a proton. The line with $S_n = 0$ (on the neutron-rich side) defines now the *neutron dripline*. Particle driplines play an important role in certain stellar explosions (Chapter 5).

1.5.3
Atomic Mass and Mass Excess

Direct measurements of nuclear masses are complicated by the presence of the atomic electrons. Atomic masses, on the other hand, can be measured with very high precision. For this reason, experimental mass evaluations tabulate atomic rather than nuclear masses. These quantities are related by

$$m_{\text{atom}}(A, Z) = m_{\text{nuc}}(A, Z) + Zm_e - B_e(Z) \tag{1.8}$$

where m_e and B_e denote the electron mass and the electron binding energy in the atom, respectively. Nuclear reactions conserve the total charge. Therefore, one may replace nuclear by atomic masses since the same number of electron rest masses is added on both sides of a reaction equation. An error is introduced by this approximation because of the difference in the electron binding energies in the atom. The electron binding energy can be approximated by (Lunney, Pearson, and Thibault, 2003)

$$B_e(Z) = 14.4381\, Z^{2.39} + 1.55468 \times 10^{-6}\, Z^{5.35} \quad \text{(eV)} \tag{1.9}$$

This contribution is smaller than the nuclear mass differences and is often neglected. In the following we will be using atomic rather than nuclear masses, unless noted otherwise.

Frequently, a quantity called *atomic mass excess* (in units of energy) is introduced, which is defined by

$$\text{M.E.} \equiv (m_{\text{atom}} - Am_u)c^2 \tag{1.10}$$

where the integer A is the mass number. The quantity m_u denotes the (unified) atomic mass unit, u, defined as one-twelfth of the mass of the neutral ^{12}C atom. Numerically, one finds $m_u c^2 = 931.494\,\text{MeV}$ (Appendix E). The Q-value for a reaction $0 + 1 \rightarrow 2 + 3$ can be expressed in terms of the mass excess as

$$\begin{aligned} Q &= m_0c^2 + m_1c^2 - m_2c^2 - m_3c^2 \\ &= (m_0c^2 + m_1c^2 - m_2c^2 - m_3c^2) + (A_2m_uc^2 + A_3m_uc^2 - A_0m_uc^2 - A_1m_uc^2) \\ &= (\text{M.E.})_0 + (\text{M.E.})_1 - (\text{M.E.})_2 - (\text{M.E.})_3 \end{aligned} \tag{1.11}$$

Using atomic masses or atomic mass excesses gives precisely the same result when calculating reaction Q-values. If positrons are involved in a reaction, then the Q-value obtained using atomic masses (or atomic mass excesses) includes the annihilation energy $2m_ec^2 = 1022$ keV of the positron with another electron from the environment, as will be shown below. In numerical expressions, we will frequently use the quantity

$$M_i = \frac{m_i}{m_u} \tag{1.12}$$

called *relative atomic mass* of species i, which is given in atomic mass units, u. The relative atomic mass for a given species is numerically close to its (integer) mass number, but for accurate work the former quantity should be used. An evaluation of atomic masses is presented in Wang *et al.* (2012). Mass measurement techniques and various theoretical mass models are reviewed in Lunney, Pearson, and Thibault (2003).

Experimental values for atomic mass excesses, binding energies, and relative atomic masses for the light nuclides are listed in Table 1.1. Note that $(\text{M.E.})_{^{12}C} \equiv 0$ by definition. The following example illustrates their use for calculating Q-values.

Example 1.3

Calculate the Q-values for the reactions (i) $^{17}\text{O} + \text{p} \rightarrow \alpha + {}^{14}\text{N}$ and (ii) $\text{p} + \text{p} \rightarrow \text{e}^+ + \nu + \text{d}$ using the information listed in Table 1.1. (The symbols e^+ and ν denote a positron and a neutrino, respectively.)

(i) For the $^{17}\text{O}(\text{p},\alpha)^{14}\text{N}$ Reaction, we find from Eq. (1.11)

$$\begin{aligned} Q &= (\text{M.E.})_{^{17}\text{O}} + (\text{M.E.})_{^{1}\text{H}} - (\text{M.E.})_{^{14}\text{N}} - (\text{M.E.})_{^{4}\text{He}} \\ &= [(-808.76) + (7288.97) - (2863.42) - (2424.92)]\,\text{keV} = 1191.87\,\text{keV} \end{aligned}$$

Exactly the same result is obtained if atomic masses are used. (ii) For the $\text{p}(\text{p},\text{e}^+\nu)\text{d}$ reaction one obtains

$$\begin{aligned} Q &= (m_{^{1}\text{H}} + m_{^{1}\text{H}} - m_{^{2}\text{H}})c^2 = (\text{M.E.})_{^{1}\text{H}} + (\text{M.E.})_{^{1}\text{H}} - (\text{M.E.})_{^{2}\text{H}} \\ &= 2 \times (7288.97\,\text{keV}) - (13135.72\,\text{keV}) = 1442.22\,\text{keV} \end{aligned}$$

Table 1.1 Experimental values of the atomic mass excess (M.E.), binding energy per nucleon (B/A), and relative atomic mass (M) for light nuclides in the $A \leq 20$ mass region.

A	Element	M.E. (keV)	B/A (keV)	M (u)
1	n	8071.3171	0.0	1.0086649158
	H	7288.97059	0.0	1.00782503223
2	H	13135.72174	1112.283	2.01410177812
3	H	14949.8061	2827.266	3.0160492779
	He	14931.2155	2572.681	3.0160293201
4	He	2424.91561	7073.915	4.00260325413
6	Li	14086.8789	5332.331	6.0151228874
7	Li	14907.105	5606.439	7.016003437
	Be	15769.00	5371.548	7.01692872
8	Li	20945.80	5159.712	8.02248625
	Be	4941.67	7062.435	8.00530510
	B	22921.6	4717.15	8.0246073
9	Li	24954.90	5037.768	9.02679019
	Be	11348.45	6462.668	9.01218307
10	Be	12607.49	6497.630	10.01353470
	B	12050.7	6475.07	10.0129369
11	Be	20177.17	5952.540	11.02166108
	B	8667.9	6927.72	11.0093054
	C	10650.3	6676.37	11.0114336
12	B	13369.4	6631.22	12.0143527
	C	0.0	7680.144	12.0000000
13	B	16562.1	6496.41	13.0177802
	C	3125.00875	7469.849	13.00335483507
	N	5345.48	7238.863	13.00573861
14	C	3019.893	7520.319	14.003241988
	N	2863.41669	7475.614	14.00307400443
	O	8007.46	7052.301	14.00859636
15	C	9873.1	7100.17	15.0105993
	N	101.4387	7699.460	15.0001088989
	O	2855.6	7463.69	15.0030656
16	N	5683.9	7373.80	16.0061019
	O	−4737.00137	7976.206	15.99491461957
17	N	7870.0	7286.2	17.008449
	O	−808.7636	7750.728	16.9991317565
	F	1951.70	7542.328	17.00209524
18	N	13113.0	7038.6	18.014078
	O	−782.8156	7767.097	17.9991596129
	F	873.1	7631.638	18.0009373
19	O	3332.9	7566.49	19.0035780
	F	−1487.4443	7779.018	18.9984031627
	Ne	1752.05	7567.342	19.00188091
20	F	−17.463	7720.134	19.99998125
	Ne	−7041.9306	8032.240	19.9924401762
	Na	6850.6	7298.50	20.0073544

Errors are not listed.
Source: Wang *et al.* (2012).

This value includes the annihilation energy $2m_e c^2 = 1022$ keV of the positron with another electron from the environment, as can be seen from

$$\begin{aligned} Q &= [m_{^1\mathrm{H}} + m_{^1\mathrm{H}} - m_{^2\mathrm{H}}]c^2 = [(m_\mathrm{p} + m_\mathrm{e}) + (m_\mathrm{p} + m_\mathrm{e}) - (m_\mathrm{d} + m_\mathrm{e})]c^2 \\ &= [m_\mathrm{p} + m_\mathrm{p} - m_\mathrm{d} + m_\mathrm{e}]c^2 = [(m_\mathrm{p} + m_\mathrm{p} - m_\mathrm{d} - m_\mathrm{e}) + 2m_\mathrm{e}]c^2 \end{aligned}$$

The symbols ^{1}H, ^{2}H and p, d in the above expression denote atomic and nuclear masses, respectively.

1.5.4 Number Abundance, Mass Fraction, and Mole Fraction

The number density of nuclei i in a stellar plasma, N_i, is equal to the total number of species i per unit volume. Avogadro's number N_A is defined as the number of atoms of species i that makes M_i gram, that is, $N_A = M_i/m_i = 6.022 \times 10^{23}$ mol^{-1}. The *mass density* is then given by $\rho = N_i m_i = N_i M_i / N_A$ if only species i is present, or by $\rho = (1/N_A)\sum_i N_i M_i$ for a mixture of species. We write

$$\begin{aligned} \frac{\sum_i N_i M_i}{\rho N_A} &= \frac{N_1 M_1}{\rho N_A} + \frac{N_2 M_2}{\rho N_A} + \frac{N_3 M_3}{\rho N_A} + \cdots \\ &= X_1 + X_2 + X_3 + \cdots = \sum_i X_i = 1 \end{aligned} \tag{1.13}$$

where the quantity

$$X_i \equiv \frac{N_i M_i}{\rho N_A} \tag{1.14}$$

represents the fraction of the mass that is bound in species i and, therefore, is called the *mass fraction*. A related quantity is the *mole fraction*, defined by

$$Y_i \equiv \frac{X_i}{M_i} = \frac{N_i}{\rho N_A} \tag{1.15}$$

In a stellar plasma, the number density N_i will change if nuclear transmutations take place. But it will also change as a result of variations in the mass density caused by compression or expansion of the stellar gas. In situations where the mass density of the stellar plasma varies, it is of advantage to express abundances in terms of the quantity Y_i instead of N_i. In a simple expansion of matter without nuclear reactions or mixing, the former quantity remains constant, whereas the latter quantity is proportional to the mass density ρ.

Strictly speaking, the mass density ρ is not a conserved quantity even if no compression or expansion of the stellar gas occurs. The reason is that nuclear transmutations transform a fraction of the nuclear mass into energy or leptons (e.g., electrons or positrons) and vice versa. To avoid this difficulty, the density is sometimes defined as $\rho_A = (1/N_A)\sum_i N_i A_i$ in terms of the number of nucleons (i.e., the mass number A_i) instead of the relative atomic mass M_i, since the number of nucleons is always conserved in a nuclear transmutation. The mass

fraction of Eq. (1.14) should in principle be replaced by the *nucleon fraction* $X_i = N_i A_i/(\rho_A N_A)$. However, the difference between mass density and nucleon density, or between mass fraction and nucleon fraction, is very small and the distinction is usually not important numerically. To avoid confusion, we will be using in this book mass densities and mass fractions. For more information on abundances see, e.g., Arnett (1996).

Example 1.4

The mass fractions of ^{1}H and ^{4}He at the time of the Sun's birth are equal to 0.71 and 0.27, respectively. Calculate the ratio of the corresponding number densities.

From Eq. (1.14) and Table 1.1, we find

$$\frac{N(^1\mathrm{H})}{N(^4\mathrm{He})} = \frac{\frac{\rho N_A \mathrm{X}(^1\mathrm{H})}{M(^1\mathrm{H})}}{\frac{\rho N_A \mathrm{X}(^4\mathrm{He})}{M(^4\mathrm{He})}} = \frac{M(^4\mathrm{He})}{M(^1\mathrm{H})}\frac{\mathrm{X}(^1\mathrm{H})}{\mathrm{X}(^4\mathrm{He})} = \frac{(4.0026\,\mathrm{u})}{(1.0078\,\mathrm{u})}\frac{0.71}{0.27} = 10.4$$

1.5.5

Decay Constant, Mean Lifetime, and Half-Life

The time evolution of the number density N (or of the absolute number of nuclei $\mathcal{N}$) of an unstable nuclide is given by the differential equation

$$\left(\frac{dN}{dt}\right) = -\lambda N \tag{1.16}$$

The quantity λ represents the probability of decay per nucleus per time. Since it is constant for a given nuclide under specific conditions (constant temperature and density), it is referred to as *decay constant*. Integration of the above expression immediately yields the radioactive decay law for the number density of undecayed nuclei remaining after a time t,

$$N = N_0 e^{-\lambda t} \tag{1.17}$$

where N_0 is the initial number density at $t = 0$. The time it takes for the number density N to fall to one-half of the initial abundance, $N_0/2 = N_0 e^{-\lambda T_{1/2}}$, is called the *half-life* $T_{1/2}$, with

$$T_{1/2} = \frac{\ln 2}{\lambda} = \frac{0.69315}{\lambda} \tag{1.18}$$

The time it takes for N to fall to $1/e = 0.36788$ of the initial abundance, $N_0/e = N_0 e^{-\lambda\tau}$, is called the *mean lifetime* τ, with

$$\tau = \frac{1}{\lambda} = 1.4427\, T_{1/2} \tag{1.19}$$

If a given nuclide can undergo different competing decays (e.g., γ- and β-decay, or different γ-ray transitions), then the total decay probability in Eqs. (1.16)–(1.19) is

given by the sum of the decay probabilities for the individual processes. Hence,

$$\lambda = \sum_i \lambda_i \qquad \text{or} \qquad \frac{1}{\tau} = \sum_i \frac{1}{\tau_i} \tag{1.20}$$

where the quantities λ_i and τ_i are called *partial* decay constant and *partial* lifetime, respectively. The product of the absolute number of nuclei, $\mathcal{N}$, and the decay constant determines the number of decays per unit time and is referred to as the *activity*, $A \equiv \lambda\mathcal{N} = -d\mathcal{N}/dt$. Common units of the activity are the curie (1 Ci = 3.7×10^{10} decays per second) and the becquerel (1 Bq = 1 decay per second). It must be emphasized that Eqs. (1.16)–(1.20) apply to any nuclear decay, such as β-decay, α-particle decay, γ-ray decay of excited levels, and the destruction of nuclei via nuclear reactions in a stellar plasma, as will be shown later.

1.6 Nuclear Shell Model

A detailed treatment of the nuclear shell model is beyond the scope of this book. Basic discussions are presented in many introductory nuclear physics texts (e.g., Krane, 1988). For a more detailed account, the reader is referred to DeShalit and Talmi (1963) or Brussaard and Glaudemans (1977). In the following we will summarize some of the important assumptions and predictions of the model. Our aim is to better understand how nuclear properties, such as binding energies, spins, and parities, can be explained from the underlying configurations of the nucleons. These considerations are also important because a number of nuclear structure properties that are mentioned in this text, for example, reduced γ-ray transition strengths, weak interaction matrix elements, and spectroscopic factors, are frequently computed using the shell model.

The *atomic* shell model has been enormously successful in describing the properties of atoms. In the case of an atom, the heavy nucleus represents a center for the Coulomb field in which the light electrons move independently in first-order approximation. The spherical Coulomb potential is given by $V_C = Ze^2/r$, with Z the atomic number, e the electron charge, and r the distance between nucleus and electron. Solving the Schrödinger equation for this system yields the electron orbits, or shells, that are characterized by various quantum numbers. In general, several of these (sub-)shells are almost degenerate in energy and together they form major shells. The rules for building up the atomic electron configuration follow immediately from the Pauli exclusion principle, stating that no more than two spin-1/2 particles can occupy a given quantum state simultaneously. The shells are then filled up with electrons in order of increasing energy. We thus obtain an inert core of filled shells and some number of valence electrons that primarily determine the atomic properties. Atoms with all states of the major shells occupied exhibit a high stability against removal or addition of an electron. These are the inert gases.

The application of a similar model to the atomic nucleus encounters a number of complications. First, the nuclear interaction is very different from the Coulomb

interaction and, moreover, the nature of the nucleon–nucleon interaction is not precisely known. Second, there are two kinds of elementary particles present in the nucleus (protons and neutrons) as opposed to the atomic case (electrons). Third, there is no heavy center of force for the nucleons. Despite these complications, the nuclear shell model has been highly successful in describing many properties of nuclei. Its basic assumption is that the interaction of each nucleon with all the other protons and neutrons in the nucleus is well approximated by some average potential $V(r)$. A single nucleon moves independently in this potential and can be described by a single-particle state of discrete energy and constant angular momentum.

The independent motion of the nucleons can be understood qualitatively in the following manner. According to the Pauli exclusion principle, no more than two protons or neutrons can exist in a given quantum state. The single-particle levels are filled with nucleons up to some level, depending on how many nucleons are present. Consider now a single nucleon, occupying some intermediate single-particle level, moving through the nucleus. The nuclear force has a short range and, therefore, we expect that the nuclear potential will strongly fluctuate. The nucleon may collide with other protons or neutrons, but it cannot gain or lose energy easily since the neighboring levels are already occupied and thus cannot accept an additional nucleon. It may gain a large amount of energy and hence move to a higher lying, unoccupied single-particle level. But such collisions with a significant energy transfer are less likely to occur. Consequently, the motion of the nucleon will often be fairly smooth.

1.6.1
Closed Shells and Magic Numbers

We will start from the assumption that the interaction between one nucleon and all the other nucleons in the nucleus can be approximated by a suitable single-particle potential. In the simplest case, it consists of a central potential (e.g., a harmonic oscillator potential or a Woods–Saxon potential) and a strong spin–orbit coupling term. The solutions of the Schrödinger equation for such a potential are bound single-particle states characterized by the values of the radial quantum number n, orbital angular momentum quantum number ℓ, and total angular momentum quantum number j (the latter is obtained from the coupling $\vec{j} = \vec{\ell} + \vec{s}$, where s denotes the intrinsic spin equal to 1/2 for protons or neutrons; see Appendix B). In particular, the energies of the single-particle states depend explicitly on the values of n, ℓ, and j. The single-particle states are energetically clustered in groups and thus reveal a shell structure. Each state of given j can be occupied by a maximum number of $(2j + 1)$ identical nucleons, corresponding to the number of magnetic substates $(m_j = -j, -j + 1, \ldots, j - 1, j)$, and thus represents a *subshell*. Several different subshells lying close in energy can be grouped together and form a *major shell*. Furthermore, each single-particle state possesses a definite parity (Appendix A), given by $\pi = (-1)^{\ell}$. The shells are filled up according to the Pauli exclusion principle.

The single-particle levels for either protons or neutrons are shown in Figure 1.11 where the horizontal direction represents an energy scale. The left-hand side, part (a), displays the single-particle energies of a harmonic oscillator potential as a function of the oscillator quantum number $N = 2(n-1) + \ell$, corresponding to the total number of oscillator quanta excited. Part (b) shows the single-particle energies of a Woods–Saxon potential. This potential is more realistic but mathematically less tractable. It is defined by $V(r) = V_0[1 + e^{(r-R_0)/a}]^{-1}$, where V_0, R_0, and a denote the potential depth, the potential radius, and the diffuseness, respectively. In part (a), each single-particle state of given N consists in general of states with different values of ℓ. These have the same energies and are thus called *degenerate*. The degeneracy does not occur for the more realistic Woods–Saxon potential, that is, states with different values of ℓ possess different energies. It is customary to use the spectroscopic notation s, p, d, f, g, … for states with orbital angular momenta of ℓ = 0, 1, 2, 3, 4, …, respectively. If an additional spin–orbit term is added to the potential, then each state of given ℓ value (except $\ell = 0$) can have a total angular momentum of either $j = \ell + 1/2$ or $j = \ell - 1/2$ (Appendix B). Since ℓ is an integer, j must be of odd half-integer value. Part (c) shows how the spin–orbit term splits each state with $\ell > 0$ into two levels. The number of identical particles (protons or neutrons) that can occupy a state of given j amounts to $(2j + 1)$ and is presented in part (d). Part (e) displays the single-particle states in spectroscopic notation as $n\ell_j$. The quantum number n corresponds to the order in which the various states of given ℓ and j appear in energy. Thus, $1s_{1/2}$ is the first $\ell = 0$, $j = 1/2$ state, $2s_{1/2}$ is the second, and so on. The parities of the single-particle levels are shown in part (f), and part (g) indicates the subtotal of the number of identical nucleons that can fill all the states up to a given level.

Notice that the spin–orbit coupling term is so strong that it changes the energies of the single-particle states significantly. For example, consider the $N = 3$ and 4 oscillator shells. The g-state ($\ell = 4$) in part (b) splits into two levels, $1g_{7/2}$ and $1g_{9/2}$. Since the spin–orbit coupling is strong the $1g_{9/2}$ state is depressed and appears to be close in energy to the $2p_{1/2}$, $1f_{5/2}$, and $2p_{3/2}$ states that originate from the $N = 3$ oscillator shell. There is now an energy gap at a subtotal nucleon (or occupation) number of 50 and, consequently, this group of states forms a major shell. Similar arguments apply to other groups of levels. It can be seen from Figure 1.11 that gaps (or major shell closures) in the single-particle energy spectrum appear at occupation numbers of 2, 8, 20, 28, 50, 82, and 126. These are referred to as *magic numbers*.

Nuclei with filled major shells of protons or neutrons exhibit an energetically favorable configuration, resulting in an extra stability compared to neighboring nuclei with only partly filled shells. The magic numbers manifest themselves in many observed nuclear properties, such as masses, particle separation energies, nuclear charge radii, electric quadrupole moments, and so on. For example, Figure 1.12 shows the difference of the measured ground-state atomic mass excess from its mean value that is calculated using a smooth semiempirical mass formula. At the locations of magic neutron numbers, the atomic mass excess is

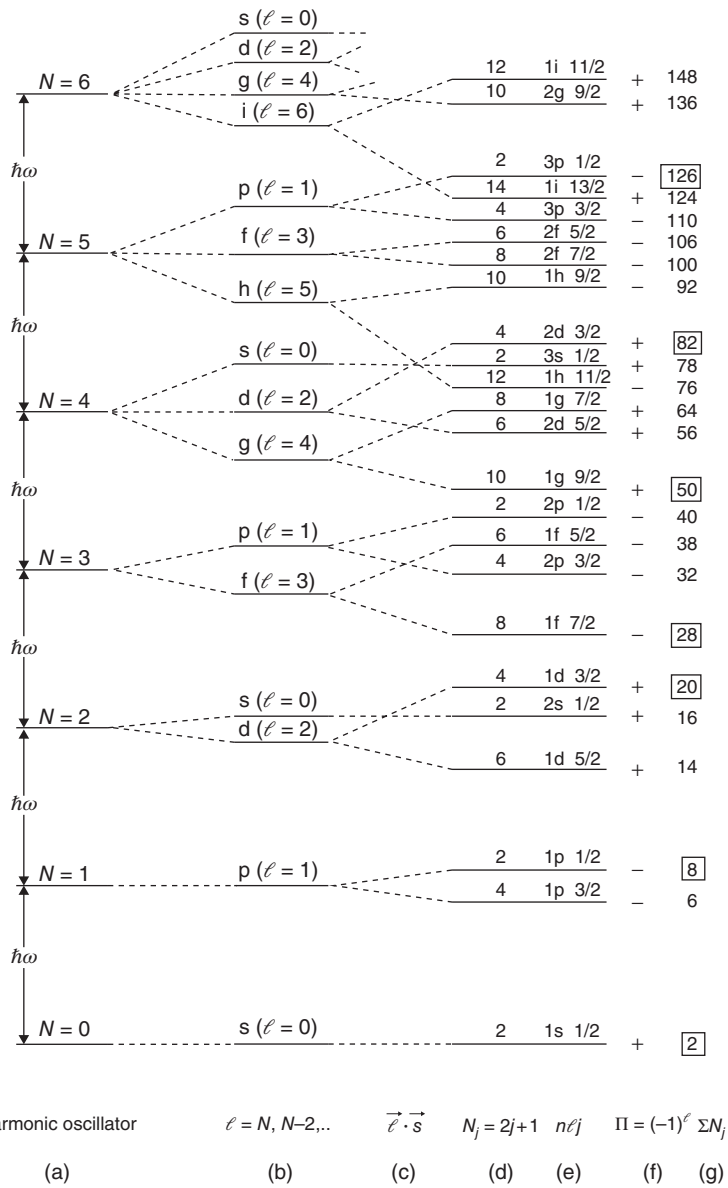

Figure 1.11 Approximate sequence of single-particle states for identical nucleons (protons or neutrons). The magic numbers (given in boxes on the right-hand side) appear at the energy gaps and correspond to the cumulative number of nucleons up to that state. The level pattern represents qualitative features only. This holds specifically for states with $N \geq 4$, where the level order differs for protons (which are subject to the Coulomb interaction) and neutrons. (Reprinted with permission from Brussaard and Glaudemans (1977). Copyright by P. J. Brussaard.)

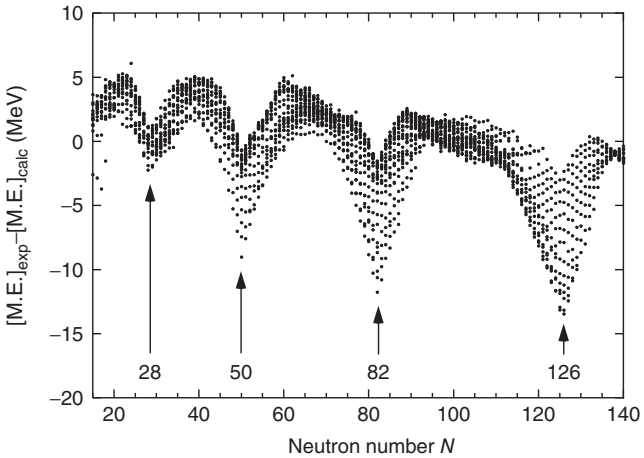

Figure 1.12 Difference between experimental ground-state atomic mass excess (Audi *et al.*, 2003) and the mass excess predicted by the spherical macroscopic part of the finite-range droplet (FRDM) mass formula (Möller *et al.*, 1995) versus neutron number.

smaller, resulting in a smaller atomic mass and a larger binding energy according to Eqs. (1.2) and (1.10). Another example will be given later in connection with neutron capture cross sections (Figure 5.67). Such observations provide unambiguous evidence for the shell structure of nuclei. As will become apparent in Section 5.6, the synthesis of the heavy elements is strongly influenced by the magic neutron numbers of $N = 50$, 82, and 126. It has to be emphasized again that the magic numbers as they are observed in nature can be reproduced only if a strong spin–orbit coupling term is introduced into the independent-particle potential.

1.6.2
Nuclear Structure and Nucleon Configuration

The shell model not only predicts the properties of closed shell nuclei, but also predicts the properties of nuclei with partly filled shells. The nuclear properties follow directly from the configuration of the nucleons: (i) the binding energy or mass of the nucleus is determined by the single-particle energies (caused by the independent motion of the nucleons in an average potential) and by the mutual interaction of the valence nucleons (i.e., those located outside a closed major shell); (ii) the total angular momentum of the nucleus (or the *nuclear spin*) is obtained by coupling the angular momenta of the independent single-particle states according to the quantum mechanical rules for vector addition (Appendix B); and (iii) the total parity of the nucleus is determined by the product of the parities for all nucleons.

Consider first a nucleus with completely filled subshells. In each subshell j all magnetic substates m_j are occupied and thus, the sum of j_z over all nucleons in the subshell must be zero. In other words, the nucleons in a completely filled subshell

must couple to an angular momentum of zero. Furthermore, since $(2j + 1)$ is an even number, the total parity of the nucleons amounts to $\pi = +1$. Indeed, the observed spin and parity of nuclei with closed subshells (or closed major shells) amount to $J^\pi = 0^+$ (e.g., ${}^{4}_{2}\mathrm{He}_2$, ${}^{12}_{6}\mathrm{C}_6$, ${}^{14}_{6}\mathrm{C}_8$, ${}^{14}_{8}\mathrm{O}_6$, ${}^{16}_{8}\mathrm{O}_8$, ${}^{28}_{14}\mathrm{Si}_{14}$, ${}^{32}_{16}\mathrm{S}_{16}$, or ${}^{40}_{20}\mathrm{Ca}_{20}$). A closed-shell nucleus can only be excited by promoting at least one nucleon to a higher lying, unoccupied, subshell. This is consistent with the observation that the first excited states of such nuclei are usually found at relatively high excitation energies. Nuclei with partly filled shells may have excited states that result from a recoupling of the angular momenta only. This explains why in such cases the observed excitation energies are significantly smaller.

By considering Figure 1.11, we can easily explain the quantum numbers for the ground states of nuclei when a single nucleon is located outside a closed subshell. In this case, the ground-state spin and parity is given by the lowest single-particle state available to the valence nucleon. For example, we find $J^\pi = 1/2^-$ for ${}^{13}_{6}\mathrm{C}_7$, $J^\pi = 5/2^+$ for ${}^{17}_{8}\mathrm{O}_9$, $J^\pi = 1/2^+$ for ${}^{29}_{14}\mathrm{Si}_{15}$, or $J^\pi = 3/2^+$ for ${}^{33}_{16}\mathrm{S}_{17}$. A single valence nucleon outside a closed subshell behaves in this respect the same as a single *hole* in an otherwise filled subshell. The ground-state spin and parity, for example, of ${}^{27}_{14}\mathrm{Si}_{13}$ amounts to $J^\pi = 5/2^+$ because it has a single neutron hole in the $1\mathrm{d}_{5/2}$ shell.

The situation is more complicated when the subshells are only partly filled. We observe experimentally that the ground states of all doubly even nuclei possess a spin and parity of $J^\pi = 0^+$. For example, this applies to ${}^{26}_{12}\mathrm{Mg}_{14}$ although neither the protons nor the neutrons completely fill the subshells. This means that it is energetically favorable for pairs of protons or neutrons to couple to a total spin and parity of $J^\pi_{\mathrm{pair}} = 0^+$. This *pairing effect* also influences the proton and neutron separation energies of neighboring nuclei, as will be seen in Section 5.6. The shell model can then be used to predict the ground-state spins and parities for odd-A nuclei. For example, consider ${}^{23}_{10}\mathrm{Ne}_{13}$. All the protons couple pairwise to quantum numbers of 0^+, as do 12 of the neutrons. The lowest available level for the odd neutron is the $1\mathrm{d}_{5/2}$ state (Figure 1.11) and thus the ground-state spin of ${}^{23}\mathrm{Ne}$ amounts to $J^\pi = 5/2^+$. These simplistic considerations reproduce many of the observed ground-state spins, but fail in some cases. According to the above arguments, one would expect a ground-state spin and parity of $J^\pi = 5/2^+$ for ${}^{23}_{11}\mathrm{Na}_{12}$, but instead we observe $J^\pi = 3/2^+$. The discrepancy is caused by the complicated interplay of many nucleons in an unfilled shell so that an even number of protons or neutrons does not always couple to a total angular momentum of $J = 0$ for the ground state. This is especially true for excited nuclear levels.

In all but the simplest situations, the nucleon configuration must be taken into account explicitly. Further complications arise since a given nuclear level may be described by a mixed configuration, that is, by different nucleon configurations that couple to the same value of J^π. In such cases, large-scale shell model calculations must be performed with numerical computer codes. The shell model has been enormously successful in explaining the structure of nuclei. It is frequently used in nuclear astrophysics to calculate nuclear quantities that have not yet been measured in the laboratory. Reduced γ-ray transition strengths (Section 1.7.2) or weak interaction transition strengths (Section 1.8.3), for instance, depend

on nuclear matrix elements that connect an initial (decaying) state with a final state. The matrix elements can be calculated numerically with the shell model in a straightforward manner once an appropriate form for the transition operator (for the electromagnetic or weak interaction) is assumed. Another important quantity in nuclear astrophysics is the spectroscopic factor. It will be explained in Section 2.5.7 how this property can be used for estimating an unknown cross section of a nuclear reaction $A + a \rightarrow B$. The spectroscopic factor is defined in terms of the overlap integral between the final state wave function of B and the initial state wave function of $A + a$. It does not depend on a transition operator, but only on a wave function overlap, and thus can be calculated rather reliably for many nuclei.

1.7 Nuclear Excited States and Electromagnetic Transitions

1.7.1 Energy, Angular Momentum, and Parity

Every nucleus exhibits excited states. They can be populated by many different means, for example, nuclear reactions, β-decays, thermal excitations (see below), inelastic electron or particle scattering, and Coulomb excitation. Each nuclear level is characterized by its excitation energy E_x, defined as the binding energy difference between the level in question and the ground state of the nucleus. For the ground state we have, as per definition, $E_x = 0$. In the laboratory, each excited level of energy E_i can make a transition to a lower lying state of energy E_f via three different processes that are all induced by the electromagnetic interaction: (i) γ-ray emission, (ii) internal conversion, and (iii) internal pair formation. *Internal conversion* refers to a process where an excited nucleus de-excites by transferring its energy directly, that is, in a single step, to an orbital electron. *Internal pair formation* denotes the de-excitation of a nucleus by creating an electron–positron pair, in which case the de-excitation energy must exceed twice the value of the electron rest energy ($2m_e c^2$). Although the three processes can in principle compete with each other, the emission of a γ-ray is by far the most important one for nuclear astrophysics and will be discussed in the following.

In a γ-ray transition between two nuclear levels, the energy of the emitted photon is given by

$$E_\gamma = E_i - E_f - \Delta E_{\mathrm{rec}} \tag{1.21}$$

where the origin of the *recoil shift* ΔE_{rec} is described in Appendix C.1 We are mainly concerned here with γ-ray energies in the range of 100 keV to 15 MeV. For such energies, the recoil shift is very small and can usually be neglected. Hence, we may use in most cases $E_\gamma \approx E_i - E_f$. This assumes that the excited nucleus decays from rest. If the decaying level is populated via a nuclear reaction, then another

correction (the Doppler shift) must also be taken into account (Appendix C.1). In any case, the emitted γ-rays will exhibit discrete energies. If E_f corresponds to the ground state, then no further emission of γ-rays is possible. Otherwise, de-excitation of the nucleus by emission of one or more photons before reaching the ground state is likely to occur.

The emitted (or absorbed) electromagnetic radiation can be classified according to the angular momentum $L\hbar$ carried by each photon, and according to its parity (Appendix B). The angular momentum carried away by the photon determines the multipolarity of the radiation. A value of L for the angular momentum corresponds to 2^L-pole radiation with its characteristic angular distribution for the emitted intensity. For example, $L = 1$ and $L = 2$ correspond to dipole (2^1) and quadrupole (2^2) radiation, respectively. Two identical radiation patterns for a given value of L may correspond to different waves, *electric* 2^L-pole radiation and *magnetic* 2^L-pole radiation, which differ through their parity. For example, E2 and M1 correspond to electric quadrupole radiation and magnetic dipole radiation, respectively. In a γ-ray transition between two nuclear levels the total angular momentum and parity of the system (nucleus plus electromagnetic field) are conserved. The conservation laws give rise to certain selection rules that must be fulfilled for an emission (or absorption) of radiation of given character to occur. The quantum mechanical rules are explained in Appendix B.

1.7.2 Transition Probabilities

A detailed discussion of the quantum theory for the interaction of nuclei with electromagnetic radiation is beyond the scope of this book. We will instead summarize the most important steps in the derivation of the transition probability. For more information, see Blatt and Weisskopf (1952).

The decay constant (i.e., the probability per unit time) for the emission of electromagnetic radiation of a given character (e.g., E1 or M2) in a transition connecting two given nuclear levels can be calculated using perturbation theory. The result is (Blatt and Weisskopf, 1952)

$$\lambda(\overline{\omega}L) = \frac{8\pi(L+1)}{\hbar L[(2L+1)!!]^2}\left(\frac{E_\gamma}{\hbar c}\right)^{2L+1} B(\overline{\omega}L) \tag{1.22}$$

with E_γ and L the energy and multipolarity of the radiation, respectively; $\overline{\omega}$ denotes either electric (E) or magnetic (M) radiation and the double factorial is defined as $(2L+1)!! \equiv 1 \cdot 3 \cdot 5 \cdot \ldots \cdot (2L+1)$. The quantity $B(\overline{\omega}L)$ is called the *reduced transition probability*. It contains the wave functions of the initial and final nuclear states, and the multipole operator, that is, the operator responsible for changing the initial to the final state while simultaneously creating a photon of proper energy, multipolarity, and character. Reduced transition probabilities can be calculated using nuclear structure models, for example, the shell model (Section 1.6). In the simplest case, one may assume that the nucleus consists of an inert core

plus a single nucleon, that the γ-ray transition is caused by this nucleon changing from one shell-model state to another, and that the radial wave functions of the initial and final states are constant over the nuclear interior and vanish outside the nucleus. With these assumptions, one obtains the *Weisskopf estimates* for the γ-ray transition probabilities, which are given below for the lowest – and as will be seen, most important – multipolarities:

$$\lambda_W(\mathrm{E1})\hbar = 6.8\times10^{-2}A^{2/3}E_\gamma^3, \qquad \lambda_W(\mathrm{M1})\hbar = 2.1\times10^{-2}E_\gamma^3 \tag{1.23}$$

$$\lambda_W(\mathrm{E2})\hbar = 4.9\times10^{-8}A^{4/3}E_\gamma^5, \qquad \lambda_W(\mathrm{M2})\hbar = 1.5\times10^{-8}A^{2/3}E_\gamma^5 \tag{1.24}$$

$$\lambda_W(\mathrm{E3})\hbar = 2.3\times10^{-14}A^{2}E_\gamma^7, \qquad \lambda_W(\mathrm{M3})\hbar = 6.8\times10^{-15}A^{4/3}E_\gamma^7 \tag{1.25}$$

In these numerical expressions, A denotes the mass number of the decaying nucleus, the photon energy E_γ is in units of mega electron volts, and the Weisskopf estimates are in units of electron volts. It will be shown later that the product $\lambda\hbar$ is equal to a γ-ray partial width.

The Weisskopf estimates for the γ-ray decay probability are shown in Figure 1.13 versus γ-ray energy for emitted radiations of different multipolarity and character. It is apparent that the quantity λ_W rises strongly with increasing γ-ray energy. We will be using in later chapters the relation $\Gamma = \lambda\hbar \sim E_\gamma^{2L+1}$, as predicted by the Weisskopf estimates, when describing the energy dependence of γ-ray partial widths. Also, the decay probability depends strongly on the multipolarity L and the character $\overline{\omega}$ of the radiation. Furthermore, according to the selection rules (Appendix B), electric and magnetic radiations of the same multipolarity cannot be emitted together in a transition between two given nuclear levels. For a

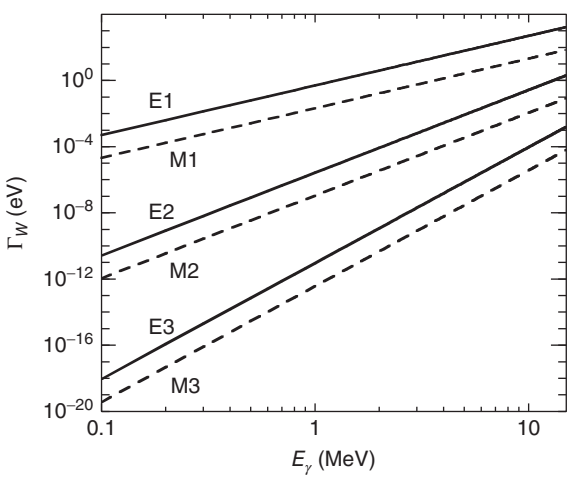

Figure 1.13 Weisskopf estimate of the γ-ray decay probability for pure electric (E) and magnetic (M) multipole radiations emitted in transitions between two nuclear levels of energy difference E_γ. The γ-ray partial width Γ_W is equal to the product $\lambda_W\hbar$. The curves are calculated for A = 20 and a nuclear radius of $R = 1.20A^{1/3}$ fm = 3.3 fm.

transition connecting two levels of opposite parities, we find from Figure 1.13 the inequalities

$$\lambda_W(\mathrm{E1}) \gg \lambda_W(\mathrm{M2}) \gg \lambda_W(\mathrm{E3}) \gg \cdots \tag{1.26}$$

In this case, the lowest multipole permitted by the selection rules usually dominates. In particular, if E1 radiation is allowed it will dominate the transition strength in the vast majority of astrophysical applications. For a transition connecting two levels of the same parity, one obtains

$$\lambda_W(\mathrm{M1}) \gg \lambda_W(\mathrm{E2}) \gg \lambda_W(\mathrm{M3}) \gg \cdots \tag{1.27}$$

However, experimentally measured γ-ray transition strengths do not support the conclusion that M1 transitions are always faster than E2 transitions if both radiations are allowed by the selection rules. The decay strengths may deviate strongly from the Weisskopf estimates since the latter are obtained using rather crude assumptions. It turns out that for many transitions the observed decay constants are several orders of magnitude smaller than the theoretically predicted value of λ_W, indicating a poor overlap in the wave functions of the initial and final nuclear levels. On the other hand, for E2 transitions it is found that the observed decay probability frequently exceeds the Weisskopf estimate by large factors. This indicates that more than one nucleon must be taking part in the transition and that the excitation energy of the decaying level is stored in the collective in-phase motion of several nucleons.

The Weisskopf estimates are very useful since they provide a standard against which to compare observed transition strengths. The latter are frequently quoted in *Weisskopf units*, defined as

$$M^2_W(\overline{\omega}L) \equiv \frac{\lambda(\overline{\omega}L)}{\lambda_W(\overline{\omega}L)} = \frac{\Gamma(\overline{\omega}L)}{\Gamma_W(\overline{\omega}L)} \qquad \text{or} \qquad \lambda(\overline{\omega}L) = M^2_W(\overline{\omega}L)\,\mathrm{W.u.} \tag{1.28}$$

This definition removes the strong energy dependence of the decay probability. Several thousand observed γ-ray transitions were analyzed in this manner and their transition strengths in Weisskopf units have been presented separately according to the multipolarity and character of the radiation (Endt, 1993, and references therein). The resulting distributions of transition strengths extend from some small value of $M^2_W(\overline{\omega}L)$, which is strongly influenced by the sensitivity of the detection apparatus, to the largest observed transition probability. The latter value defines for each combination of $\overline{\omega}L$ a *recommended upper limit* (RUL). For the mass region $A = 5$–44, the following values have been reported (Endt, 1993)

$$\begin{aligned} &\mathrm{RUL(E1)} = 0.5\,\mathrm{W.u.}, && \mathrm{RUL(M1)} = 10\,\mathrm{W.u.} \\ &\mathrm{RUL(E2)} = 100\,\mathrm{W.u.}, && \mathrm{RUL(M2)} = 5\,\mathrm{W.u.} \\ &\mathrm{RUL(E3)} = 50\,\mathrm{W.u.}, && \mathrm{RUL(M3)} = 10\,\mathrm{W.u.} \end{aligned}$$

These values are important for estimating the maximum expected γ-ray decay probability for an unobserved transition (Problem 1.5). It is tempting to estimate

average decay strengths based on the centroids of the observed transition strength distributions (see Figure 2 in Endt, 1993). However, one has to be very careful since the "averages" (as well as the "lower limits") depend on the γ-ray detection limit and thus may decrease with an improvement in the sensitivity of the detection equipment.

1.7.3 Branching Ratio and Mixing Ratio

So far we discussed γ-ray transitions of specific multipolarity L and character $\overline{\omega}$. In practice, however, a given initial state may decay to a number of different final states. Furthermore, each transition connecting two given states may proceed via a mixture of radiations according to the selection rules. These complications can be described by introducing two new quantities, the branching ratio and the mixing ratio. In the following we will express these quantities in terms of the γ-ray decay probability in units of energy, $\Gamma = \lambda\hbar$, also called the γ-ray partial width. Consider Figure 1.14 showing the γ-ray decay of an initial excited level *i*. The *total* γ-ray width of the initial state can be expressed in terms of *partial* γ-ray widths that each correspond to a transition to a specific final state *j* as

$$\Gamma_{\text{tot}} = \sum_j \Gamma_j \tag{1.29}$$

Assuming that the initial state decays only by γ-ray emission, the *γ-ray branching ratio* is defined by

$$B_j \equiv \frac{\Gamma_j}{\Gamma_{\text{tot}}} \times 100\% \tag{1.30}$$

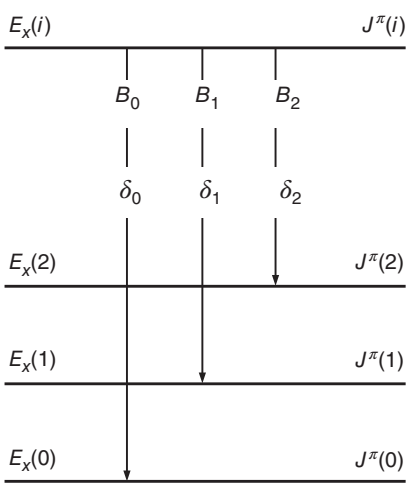

Figure 1.14 Energy level diagram showing the γ-ray decay of an initial state *i* to the ground state (0) and to two excited states (1, 2). The branching ratio B_j represents the relative intensity of a particular decay branch as a percentage of the total intensity and δ_j denotes the multipolarity mixing ratio.

and is usually given in percent. Each γ-ray branch may result from radiations of different multipolarities L and characters $\overline{\omega}$. Although the selection rules may allow for three or more possibilities (e.g., a $2^+ \rightarrow 1^+$ transition may proceed via M1, E2, or M3 radiations), in most practical cases not more than the lowest two values of $\overline{\omega}L$ need to be taken into account. If we assume that only radiations with $\overline{\omega}'L$ and $\overline{\omega}L + 1$ contribute to the transition (M1 and E2 in the above example), the partial γ-ray width is given by

$$\Gamma_j(\overline{\omega}L + 1; \overline{\omega}'L) = \Gamma_j(\overline{\omega}L + 1) + \Gamma_j(\overline{\omega}'L) \tag{1.31}$$

The γ-*ray multipolarity mixing ratio* is defined as

$$\delta_j^2 \equiv \frac{\Gamma_j(\overline{\omega}L + 1)}{\Gamma_j(\overline{\omega}'L)} \tag{1.32}$$

By combining Eqs. (1.29)–(1.32), we may express the individual widths in terms of the total width as

$$\Gamma_j(\overline{\omega}'L) = \frac{1}{1 + \delta_j^2} \frac{B_j}{100} \Gamma_{\text{tot}} \tag{1.33}$$

$$\Gamma_j(\overline{\omega}L + 1) = \frac{\delta_j^2}{1 + \delta_j^2} \frac{B_j}{100} \Gamma_{\text{tot}} \tag{1.34}$$

A highly excited nuclear state with many different decay probabilities to lower lying levels will preferably decay via those transitions that correspond to the largest decay strengths, that is, via emission of radiations with the smallest multipoles. If a given level is located, say, above at least 20 lower lying states, then the observed γ-ray decays from this level are in almost all instances either of dipole (E1 or M1, depending on the parity of the initial and final level) or of E2 character. This empirical finding is called the *dipole or E2 rule* (Endt, 1990) and is useful for estimating unknown spin and parities of nuclear levels.

1.7.4
γ-Ray Transitions in a Stellar Plasma

In a hot plasma, excited states in a given nucleus are thermally populated, for example, through absorption of photons (photoexcitation), Coulomb excitation by surrounding ions, inelastic particle scattering, and other means. The time scale for excitation and de-excitation (e.g., via emission and absorption of photons) in a hot stellar plasma is usually – with the important exception of isomeric states (see below) – considerably shorter than stellar hydrodynamical time scales, even under explosive conditions (Fowler, Caughlan, and Zimmerman, 1975). These excited levels will participate in nuclear reactions and β-decays, as will be explained later, and thus their population must in general be taken into account.

For a given nuclide in a nondegenerate plasma at thermodynamic equilibrium, the ratio of the number density of nuclei in excited state μ, denoted by N_μ, and the total number density of nuclei, N, is given by a Boltzmann distribution (Ward and Fowler, 1980)

$$P_\mu = \frac{N_\mu}{N} = \frac{g_\mu e^{-E_\mu/kT}}{\sum_\mu g_\mu e^{-E_\mu/kT}} = \frac{g_\mu e^{-E_\mu/kT}}{G} \tag{1.35}$$

with $g_\mu \equiv (2J_\mu + 1)$, J_μ and E_μ the statistical weight, spin and excitation energy, respectively, of state μ; the quantity k denotes the Boltzmann constant and T is the plasma temperature. The sum over μ in the denominator includes the ground state and is referred to as the *partition function, G*. Equation (1.35) follows directly from statistical thermodynamics and encompasses all the different processes for the excitation and de-excitation of levels (i.e., not only the emission and absorption of photons). The thermal population of excited nuclear levels becomes more important with increasing temperature and lower excitation energy. These properties of Eq. (1.35) are explored in Problem 1.6.

1.7.5 Isomeric States and the Case of ^{26}Al

In most cases, the nuclear levels decaying by γ-ray emission have very high transition probabilities, corresponding to half-lives that are generally $< 10^{-9}$ s. However, in some cases the half-lives are longer by many orders of magnitude, amounting to seconds, minutes or even days. Such long-lived excited nuclear levels are referred to as *isomeric states* (or isomers, or metastable states) and the corresponding γ-ray decays are called *isomeric transitions*. We will denote these levels with the superscript m (e.g., $^A\mathrm{X}^m$).

The two aspects that are mainly responsible for the long half-lives of isomeric states are (i) a large difference for the spins of the isomeric and the final nuclear level, and (ii) a relatively small energy difference between the two levels. The first aspect implies a large γ-ray multipolarity (e.g., M4 or E5). The second aspect implies a small γ-ray energy. According to Eq. (1.22), both of these effects have the tendency to reduce the decay probability substantially.

We will illustrate some of the complexities that arise from the presence of an isomer by discussing the important case of ^{26}Al. An energy level diagram is displayed in Figure 1.15. Focus first only on the left-hand part, showing the ground state ($E_x = 0$, $J^\pi = 5^+$) and three excited states ($E_x = 228$ keV, $J^\pi = 0^+$; $E_x = 417$ keV, $J^\pi = 3^+$; and $E_x = 1058$ keV, $J^\pi = 1^+$) in ^{26}Al. According to the selection rules, the direct γ-ray de-excitation of the first excited state at $E_x = 228$ keV would require the emission of M5 radiation. The γ-ray decay probability for such a high multipolarity is very small and thus the first excited state is an isomer ($^{26}\mathrm{Al}^m$). It decays via a β-transition (which is considerably more likely to occur than the M5 γ-ray transition) to the ground state of ^{26}Mg with a half-life of $T_{1/2}(^{26}\mathrm{Al}^m) = 6.34$ s. The ^{26}Al ground state is also β-unstable and decays with a half-life of

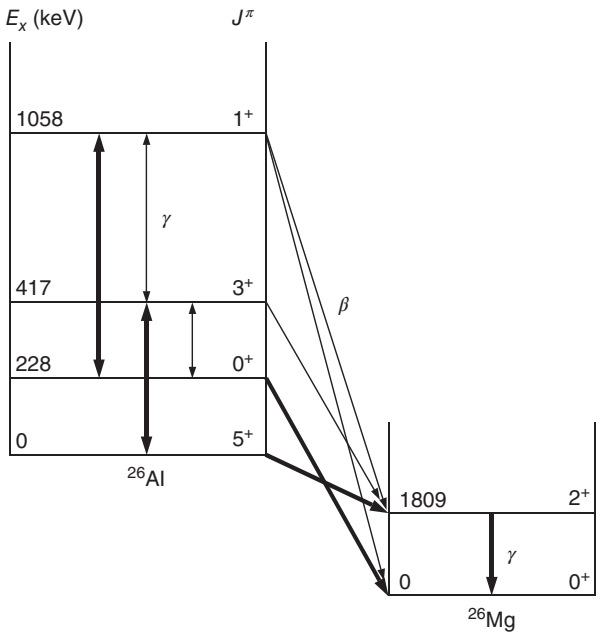

Figure 1.15 Energy level schemes of ^{26}Al and ^{26}Mg, showing the lowest lying states in each nuclide. The vertical arrows represent γ-ray decays, while the diagonal arrows indicate β-decay transitions. Only the transitions indicated by the thick arrows have been observed experimentally. The transitions shown as thin arrows play an important role in the equilibration of the ground state and the isomer at E_x = 228 keV in ^{26}Al. The direct γ-ray de-excitation of the isomer is strongly inhibited by the selection rules. The presence of ^{26}Al^g in the interstellar medium is inferred from the observed intensity of the 1809 keV γ-ray, originating from the de-excitation of the first excited state in ^{26}Mg. A small β-decay branch of the ^{26}Al ground state to the E_x = 2938 keV ($J^\pi = 2^+$) level in ^{26}Mg is omitted in the figure for clarity.

$T_{1/2}(^{26}\text{Al}^g) = 7.17 \times 10^5$ y mainly to the first excited state at $E_x = 1809$ keV in ^{26}Mg. This level, in turn, de-excites quickly via γ-ray emission of E2 character.

Interestingly, photons with an energy of 1809 keV originating from the interstellar medium have been detected first by the HEAO-3 spacecraft (Mahoney *et al.*, 1982), and subsequently by other instruments. The $E_x = 1809$ keV level in ^{26}Mg decays so quickly (within a fraction of a second) that, if it is populated via nuclear reactions in the interiors of stars, the emitted 1809 keV photons would immediately be absorbed by the surrounding matter and would never be able to escape from the stellar production site. However, suppose instead that ^{26}Al^g is synthesized via nuclear reactions in the stellar interior. The long half-life of the ground state provides ample opportunity for this species to be expelled from a star into the interstellar medium, where it then decays so that the emitted photons can reach the Earth. Only the decay of the ground state, but not the decay of the isomer, in ^{26}Al gives rise to the emission of 1809 keV γ-rays.

An all-sky map of the 1809 keV γ-ray line, obtained by the Imaging Compton Telescope (COMPTEL) aboard the Compton Gamma Ray Observatory (CGRO), is shown in color Figure 12 on page 624. The discovery of $^{26}Al^g$ in the interstellar medium is of paramount importance, as already pointed out (Section 1.4.1). It demonstrates that nucleosynthesis is currently active since the $^{26}Al^g$ half-life is considerably shorter than the time scale of Galactic chemical evolution ($\approx 10^{10}$ y). From the observed γ-ray intensity, it is estimated that the production rate of $^{26}Al^g$ in the Galaxy amounts to $\approx 2M_\odot$ per 10^6 y. The origin of the Galactic $^{26}Al^g$ is controversial at present. However, the observational evidence favors massive stars as sources. For example, the all-sky map of the 1809 keV γ-ray line shows that $^{26}Al^g$ is confined along the Galactic disk and that the measured intensity is clumpy and asymmetric. Furthermore, the measurement of the Doppler shift of the 1809 keV line demonstrated that the $^{26}Al^g$ co-rotates with the Galaxy and hence supports a Galaxy-wide origin for this species (Diehl *et al.*, 2006). Stellar model calculations for massive stars suggest that $^{26}Al^g$ is mainly produced in type II supernovae during explosive neon–carbon burning (Section 5.4.3 and right side of Figure 1.7). A smaller fraction is possibly synthesized in Wolf–Rayet stars during core hydrogen burning and in the subsequent type Ib/Ic supernova explosion. For more information, see Limongi and Chieffi (2006).

We noted above that in a hot stellar plasma, most nuclear levels quickly achieve thermal equilibrium since the time scales for excitation and de-excitation are very short. However, this is not necessarily the case for isomeric states. For example, the γ-ray transition probabilities for the de-excitation of the ^{26}Al isomer at $E_x =$ 228 keV and for its population from the ground state via absorption of radiation depend on the same reduced transition strength. Since the emission or absorption of M5 radiation is unlikely, the ground and isomeric states in ^{26}Al cannot achieve thermal equilibrium directly (i.e., Eq. (1.35) is not generally valid in this case). Thermal equilibrium may nevertheless be achieved indirectly via transitions involving higher lying levels in ^{26}Al.

Consider again Figure 1.15. In this case, the ground state and the isomer can communicate via the $E_x = 417$ keV state ($0 \leftrightarrow 417 \leftrightarrow 228$) or via the $E_x =$ 1058 keV state ($0 \leftrightarrow 417 \leftrightarrow 1058 \leftrightarrow 228$). Higher lying ^{26}Al states also play a role as the temperature is increased, but have been omitted in the figure for clarity. The thermal equilibration of ^{26}Al can be calculated by solving numerically a set of linear differential equations that describe all possible γ-ray and β-decay transitions. For some of these (indicated by thick arrows), the experimental transition strengths are known, while for others (thin arrows) the transition strengths have to be calculated using the shell model (Section 1.6). The procedure is described in detail in Coc, Porquet, and Nowacki (1999) and Runkle, Champagne, and Engel (2001), and is not repeated here. The resulting effective lifetime of ^{26}Al versus temperature is displayed in Figure 1.16. The solid line is obtained numerically by taking explicitly the equilibration of the ground and isomeric states via thermal excitations involving higher lying levels into account. The dashed curve is calculated analytically by assuming that the ground and isomeric states are in thermal

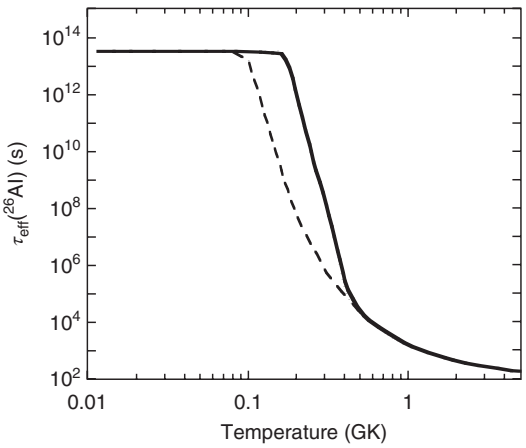

Figure 1.16 Effective lifetime of ^{26}Al as a function of temperature. The solid line is adopted from Coc, Porquet, and Nowacki (1999) and Runkle, Champagne, and Engel (2001). It was obtained numerically by taking explicitly the equilibration of the ground and isomeric states via thermal excitations involving higher lying levels into account. At each temperature, the calculation was started with a given amount of pure $^{26}Al^g$. The value of $\tau_{eff}(^{26}Al)$ is then defined by the time necessary for the total (ground plus isomeric state) ^{26}Al abundance to decline by $1/e$. The dashed curve is calculated analytically by assuming that the ground and isomeric states are in thermal equilibrium (Example 1.5).

equilibrium (Example 1.5). Below $T = 0.1$ GK, the effective lifetime is given by the laboratory lifetime of $^{26}Al^g$ ($\tau = 1.4427\, T_{1/2} = 3.3 \times 10^{13}$ s). Above $T = 0.4$ GK, the ground and isomeric states are in thermal equilibrium. At intermediate temperatures, $T = 0.1$–0.4 GK, the equilibration of ^{26}Al via higher lying levels results in an effective lifetime that differs significantly from the thermal equilibrium value.

We focussed here on the case of ^{26}Al. Other important examples of isomers in nuclear astrophysics are $^{176}Lu^m$ (Zhao and Käppeler, 1991) and $^{180}Ta^m$ (Wisshak *et al.*, 2001). For a distinction between the kind of isomer discussed above (also called *spin-isomer*) and other types of isomers (*shape-* and *K-isomers*), see Walker and Dracoulis (1999).

1.8 Weak Interaction

The strong nuclear force and the electromagnetic force govern the nuclear reactions that are of outstanding importance for the energy generation and the nucleosynthesis in stars. However, weak interactions also play an important role in stars for several reasons. First, when a radioactive nuclide is produced during the nuclear burning, its decay via weak-interaction processes will compete with its

destruction via nuclear reactions, as will become apparent in Chapter 5. Second, weak interactions determine the *neutron excess parameter* during the nucleosynthesis, defined as

$$\eta \equiv \sum_i (N_i - Z_i) Y_i = \sum_i \frac{(N_i - Z_i)}{M_i} X_i \qquad \text{with} \qquad -1 \leq \eta \leq 1 \tag{1.36}$$

where N_i, Z_i, M_i, Y_i, and X_i denote the number of neutrons and protons, the relative atomic mass (in atomic mass units), the mole fraction, and the mass fraction, respectively. The sum runs over all nuclides i in the plasma. Note that $\eta = 0$ if only $N = Z$ nuclei (^{4}He, ^{12}C, ^{16}O, and so on) are present. The quantity η represents physically the number of *excess* neutrons per nucleon in the plasma and can only change as a result of weak interactions. A closely related quantity is the electron mole fraction, Y_e, which, according to Eqs. (1.13) and (1.15), is equal to the electron-to-baryon ratio, or the proton-to-baryon ratio,

$$Y_e = \frac{N_e}{\sum_i N_i M_i} \tag{1.37}$$

where the sum is again over all nuclides present and N_e denotes the electron number density. Thus, the electron mole fraction is related to the neutron excess parameter via

$$\eta = 1 - 2Y_e \tag{1.38}$$

The neutron excess must be monitored carefully in stellar model computations, since it is of crucial importance for the nucleosynthesis during the late burning stages in massive stars and during explosive burning (Section 5.3). Furthermore, we already mentioned that electron capture is very important for the dynamic behavior of the core collapse in massive stars before a type II supernova explosion because it reduces the number of electrons available for pressure support (Section 1.4.3). Third, neutrinos emitted in weak interactions affect the energy budget of stars and thus influence models of stellar evolution and explosion.

We will focus in this section on the process of nuclear β-decay, which involves the proton, neutron, electron, positron, neutrino, and antineutrino, and we will summarize some concepts that are important in the present context. Weak interaction processes in stars will be addressed in Chapter 5. A note regarding the nomenclature. Neutrinos come in three types, or *flavors*: electron neutrinos, muon neutrinos, and tau neutrinos. For weak interaction processes where this distinction matters, we will use appropriate subscripts for the different flavors (ν_e, ν_μ, ν_τ). If no subscript is used, the symbol ν refers explicitly to electron neutrinos.

1.8.1 Weak Interaction Processes

Consider first the free neutron. It decays into a proton under the influence of the weak interaction via

$$n \rightarrow p + e^- + \overline{\nu} \tag{1.39}$$

where e^- and $\overline{\nu}$ denote an electron and antineutrino, respectively. The half-life of the free neutron amounts to $T_{1/2} = 10.2$ min. This decay is slower by many orders of magnitude compared to typical nuclear reaction time scales or electromagnetic decay probabilities and demonstrates that the interaction causing β-decay is very weak. The most common weak interaction processes in nuclear β-decay are listed below:

$$ {}^{A}_{Z}X_N \rightarrow {}^{A}_{Z+1}X'_{N-1} + e^- + \overline{\nu} \qquad \beta^-\text{-decay (electron emission)} \qquad (1.40) $$

$$ {}^{A}_{Z}X_N \rightarrow {}^{A}_{Z-1}X'_{N+1} + e^+ + \nu \qquad \beta^+\text{-decay (positron emission)} \qquad (1.41) $$

$$ {}^{A}_{Z}X_N + e^- \rightarrow {}^{A}_{Z-1}X'_{N+1} + \nu \qquad \text{electron capture} \qquad (1.42) $$

$$ {}^{A}_{Z}X_N + \nu \rightarrow {}^{A}_{Z+1}X'_{N-1} + e^- \qquad \text{neutrino capture} \qquad (1.43) $$

$$ {}^{A}_{Z}X_N + \overline{\nu} \rightarrow {}^{A}_{Z-1}X'_{N+1} + e^+ \qquad (1.44) $$

Here e^+, ν, and $\overline{\nu}$ denote a positron, neutrino, and antineutrino, respectively. In each of these interactions, the decaying nuclide changes its chemical identity, but the mass number A remains the same. The light particles e^-, e^+, ν, and $\overline{\nu}$ are leptons, that is, they do not interact via the strong nuclear force.

The first three decays represent the most common weak interaction processes of radioactive nuclei in the laboratory. Consider an example, the β-decay of ${}^{64}_{29}Cu_{35}$. It may proceed via ${}^{64}_{29}Cu_{35} \rightarrow {}^{64}_{30}Zn_{34} + e^- + \overline{\nu}$ (β^--decay), ${}^{64}_{29}Cu_{35} \rightarrow {}^{64}_{28}Ni_{36} + e^+ + \nu$ (β^+-decay), or ${}^{64}_{29}Cu_{35} + e^- \rightarrow {}^{64}_{28}Ni_{35} + \nu$ (electron capture). When the electron is captured from the atomic K-shell, the process is called *K capture*. Neutrino capture is observed, for example, in the reaction ${}^{37}_{17}Cl_{20} + \nu \rightarrow {}^{37}_{18}Ar_{19} + e^-$, which has been used for the detection of solar neutrinos (Davis, Harmer, and Hoffman, 1968). Antineutrinos produced by nuclear power plants have been observed via the process $p + \overline{\nu} \rightarrow e^+ + n$ (Reines and Cowan, 1959).

Positron emission and electron capture populate the same daughter nuclide. In later chapters, both of these decays will sometimes be considered together, while at other times it will be important to distinguish between these processes. We will be using the following abbreviated notation. The β-decay of ^{64}Cu to ^{64}Ni, irrespective of the specific process, will be denoted by $^{64}\mathrm{Cu}(\beta^+\nu)^{64}\mathrm{Ni}$. When we would like to make specific reference to the positron emission or electron capture, we write $^{64}\mathrm{Cu}(e^+\nu)^{64}\mathrm{Ni}$ or $^{64}\mathrm{Cu}(e^-,\nu)^{64}\mathrm{Ni}$, respectively. The β^--decay of ^{64}Cu to ^{64}Zn will be denoted by $^{64}\mathrm{Cu}(\beta^-\nu)^{64}\mathrm{Zn}$, irrespective of the fact that an antineutrino rather than a neutrino is emitted in this decay.

1.8.2 Energetics

The total energy release in nuclear β-decay can be expressed by the difference of the *atomic* masses before and after the interaction. We find (Problem 1.7)

$$ Q_{\beta^-} = \left[m({}^{A}_{Z}X_N) - m({}^{A}_{Z+1}X'_{N-1})\right] c^2 \qquad \beta^-\text{-decay} \qquad (1.45) $$

$$ Q_{e^+} = \left[m({}^{A}_{Z}X_N) - m({}^{A}_{Z-1}X'_{N+1}) - 2m_e\right] c^2 \qquad \text{positron emission} \qquad (1.46) $$

$$ Q_{EC} = \left[m({}^{A}_{Z}X_N) - m({}^{A}_{Z-1}X'_{N+1})\right] c^2 - E_b \qquad \text{electron capture} \qquad (1.47) $$

where m_e and E_b denote the electron mass and the atomic binding energy of the captured electron, respectively. The released energy is almost entirely transferred to the emitted leptons. For example, in β^--decay we have $Q_{\beta^-} = K_e + E_\nu$, where K_e and E_ν denote the kinetic electron energy and the total neutrino energy, respectively. Since there are three particles after the interaction, the electron and neutrino energy distributions must be continuous, ranging from zero to Q_{β^-} for each lepton. In electron capture, only one lepton is emitted and thus the neutrino is monoenergetic, with $Q_{EC} = E_\nu$. Furthermore, this decay mode is accompanied by X-ray emission since the vacancy in the atomic shell caused by the captured electron is quickly filled by other atomic electrons. Electron capture competes in general with positron emission since both decay modes populate the same daughter nucleus. However, if the difference in *atomic* masses amounts to $[m(^A_Z X_N) - m(^A_{Z-1}X'_{N+1})]c^2 < 2m_e c^2 = 1022$ keV, then only electron capture is energetically allowed.

It must be emphasized that for positron emission in a stellar plasma, the energy release calculated from the mass difference of parent and daughter nucleus alone, $Q'_{e^+} = [m(^A_Z X_N) - m(^A_{Z-1}X'_{N+1})]c^2$, includes the annihilation energy $2m_e c^2 = 1022$ keV of the positron with another electron from the environment, as can be seen by comparison with Eq. (1.46). Therefore, the quantity Q'_{e^+} rather than Q_{e^+} is of primary interest when calculating the energy release of positron emission in a stellar plasma. Also, Q'_{e^+} must be properly corrected for neutrino losses (see below).

We considered so far only β-decay transitions involving nuclear ground states. If a transition proceeds to an excited state in the daughter nucleus, then we have to replace Q_i by $Q_i^{gs} - E_x$ in Eqs. (1.45)–(1.47), where Q_i^{gs} and E_x denote the ground-state energy release and the excitation energy, respectively. Sometimes a β-decay populates levels in the daughter nucleus that are unstable by emission of light particles (protons, neutrons, or α-particles). These transitions give rise to *β-delayed particle decays*. They compete with transitions to bound states in the daughter nucleus. Therefore, both of these processes have to be distinguished carefully when modeling the nucleosynthesis in certain scenarios. For example, consider the β-decay of ^{29}S which proceeds with about equal probability to bound states in ^{29}P and to excited ^{29}P levels that are unbound by proton emission. In the first case, ^{29}S decays to the final nucleus ^{29}P via $^{29}\mathrm{S} \rightarrow \mathrm{e}^+ + \nu + {}^{29}\mathrm{P}$, while in the second case ^{29}S decays to the final nucleus ^{28}Si via $^{29}\mathrm{S} \rightarrow \mathrm{e}^+ + \nu + {}^{29}\mathrm{P}^*$ and $^{29}\mathrm{P}^* \rightarrow {}^{28}\mathrm{Si} + \mathrm{p}$. These processes can be distinguished using the notations $^{29}\mathrm{S}(\mathrm{e}^+\nu)^{29}\mathrm{P}$ and $^{29}\mathrm{S}(\mathrm{e}^+\nu\mathrm{p})^{28}\mathrm{Si}$.

The neutrinos released in nuclear β-decay interact so weakly with matter that they are lost from the star unless the density is very large ($\rho \geq 10^{11}$ g/cm^3). Consequently, the average neutrino energy must usually be subtracted from the total nuclear energy liberated when considering the energy budget of a star. An approximate expression for the average neutrino energy loss in β^--decay or positron emission is given by (Fowler, Caughlan, and Zimmerman, 1967)

$$\overline{E}_\nu^\beta \approx \frac{m_e c^2}{2} w \left(1 - \frac{1}{w^2}\right)\left(1 - \frac{1}{4w} - \frac{1}{9w^2}\right) \tag{1.48}$$

where $w = (Q_\beta + m_e c^2)/m_e c^2$. The energy release of the β-decay, Q_β, is given by Eqs. (1.45) and (1.46), and may need to be corrected for the excitation energy if the transition proceeds to an excited state in the daughter nucleus. As already mentioned above, the neutrinos emitted in electron capture are monoenergetic.

Neutrino emission is also important for the transport of energy from the stellar interior to the surface, from which the energy can be radiated. During the early evolutionary stages of stars, internal energy is mainly transported by mechanisms such as radiative diffusion or convection. As a result, the rate of energy outflow is related to the temperature gradient of the star. At high temperature ($T > 10^9$ K), however, a relatively large number of photons have energies in excess of the threshold for pair production, $\gamma \rightarrow e^+ + e^-$ (Section 4.2.2). The positron and electron, in turn, may either annihilate via $e^+ + e^- \rightarrow 2\gamma$ or via $e^+ + e^- \rightarrow \nu + \overline{\nu}$. These neutrinos emerge directly from their point of origin and will escape from the star. During the late evolutionary stages of massive stars, this production of neutrino–antineutrino pairs represents the dominant energy loss mechanism. The energy outflow is in this case directly determined by the neutrino production rate. Neutrino energy losses rise strongly with temperature and have a profound influence on the stellar evolution of massive stars (Section 1.4.3 and Chapter 5).

1.8.3 β-Decay Probabilities

A detailed discussion of the theory of weak interactions in nuclei is beyond the scope of the present book. A modern account can be found, for example, in Holstein (1989). Here we will focus on the elementary Fermi theory of β-decay which explains satisfactorily lifetimes and the shapes of electron (or positron) energy distributions. Fermi's theory of β-decay is discussed in most introductory nuclear physics texts (see, e.g., Krane, 1988). We will initially assume that the β-decay occurs under laboratory conditions. Beta-decays in stellar plasmas will be addressed afterward. The rate of nuclear β-decay can be calculated from the golden rule of time-dependent, first-order perturbation theory (Messiah, 1999). To illustrate the most important results, we will first discuss β^--decay, although the derived expressions are equally valid for positron emission. The case of electron capture is subsequently discussed.

Electron or Positron Emission

The probability $N(p)\,dp$ per unit time that an electron (or positron) with linear momentum between p and $p + dp$ is emitted can be written as

$$d\lambda = N(p)\,dp = \frac{2\pi}{\hbar}\left|\int \Psi_f^* H \Psi_i\, dV\right|^2 \frac{dn}{dE_0} = \frac{2\pi}{\hbar}\left|H_{fi}\right|^2 \frac{dn}{dE_0} \tag{1.49}$$

where Ψ_i and Ψ_f are the total wave functions before and after the decay, respectively, H is the Hamiltonian associated with the weak interaction, and dV is a volume element. The factor dn/dE_0 denotes the number of final states per unit

energy. A given transition is more likely to proceed if the number of accessible final states is large. The experimental evidence shows that the shapes of many measured electron (or positron) energy distributions are dominated by the factor dn/dE_0. The integral H_{fi} (or matrix element), which depends only weakly on energy, determines the overall magnitude of the decay probability. It can be expressed in terms of the separate wave functions of the final nuclear state (ψ_f) and of the leptons (ϕ_e, ϕ_ν) after the decay as

$$H_{fi} = g \int \left[\psi_f^* \phi_e^* \phi_\nu^*\right] \Omega \Psi_i \, dV \tag{1.50}$$

where the constant g determines the strength of the interaction. For electron (or positron) decay, the total wave function before the transition is equal to the wave function of the parent nucleus, $\Psi_i = \psi_i$. The operator Ω describes the transition from nuclear level ψ_i to level ψ_f. The emitted neutrino (or antineutrino) can be treated as a free particle because it interacts only weakly. The emitted electron (or positron) can also be treated as a free particle because it has a relatively high velocity and is little affected by the nuclear Coulomb field. Thus, we may approximate the lepton wave functions by plane waves, normalized within the nuclear volume V, and expand the exponentials according to

$$\phi_e(\vec{r}) = \frac{1}{\sqrt{V}} e^{-i\vec{p}\cdot\vec{r}/\hbar} \approx \frac{1}{\sqrt{V}} \left(1 + \frac{i\vec{p}\cdot\vec{r}}{\hbar} + \cdots\right) \tag{1.51}$$

$$\phi_\nu(\vec{r}) = \frac{1}{\sqrt{V}} e^{-i\vec{q}\cdot\vec{r}/\hbar} \approx \frac{1}{\sqrt{V}} \left(1 + \frac{i\vec{q}\cdot\vec{r}}{\hbar} + \cdots\right) \tag{1.52}$$

where $\vec{p}$ and $\vec{q}$ are the linear momenta of the electron (or positron) and the neutrino (or antineutrino), respectively. Consider, for example, the emission of an electron in β^--decay with a typical kinetic energy of 1 MeV. The relativistic electron momentum amounts in this case to $p = 1.4\ \mathrm{MeV}/c$. For a nuclear radius of $r \approx 5$ fm, we find then a value of $pr/\hbar = 0.035$. Hence, the second term in the expansion of Eq. (1.51) is usually very small and, therefore, the electron wave function is approximately constant over the nuclear volume. Similar arguments apply to the neutrino wave function. In the simplest case, one may then retain just the first, leading, term in Eqs. (1.51) and (1.52). It follows

$$|H_{fi}|^2 = \frac{1}{V^2} \left| g \int \psi_f^* \Omega \psi_i \, dV \right|^2 = \frac{1}{V^2} g^2 M^2 \tag{1.53}$$

The nuclear matrix element M describes the transition probability between the initial and final nuclear levels. A proper relativistic treatment of β-decay results in two different matrix elements with different strengths that may contribute to the overall transition probability. Thus, we have to replace Eq. (1.53) by

$$|H_{fi}|^2 = \frac{1}{V^2} \left(G_V^2 M_F^2 + G_A^2 M_{\mathrm{GT}}^2\right) \tag{1.54}$$

where G_V and G_A are the vector and axial-vector coupling constants, and M_F and M_{GT} are referred to as *Fermi* and *Gamow–Teller matrix element*, respectively.

It can be shown that no interference term between vector and axial-vector interaction occurs. The two matrix elements depend on the structure of the initial and final nuclear states and can be calculated by using the shell model (Section 1.6).

The above nonrelativistic treatment of the nucleons and the assumption of constant lepton wave functions over the nuclear volume results in nuclear matrix elements that are independent of the lepton energies and define the *allowed β-decay transitions*. In some decays, however, it turns out that angular momentum and parity selection rules prevent allowed transitions. In such cases, the next terms in the plane wave approximations of Eqs. (1.51) and (1.52) have to be taken into account and the nuclear matrix element is no longer independent of energy. These transitions are termed *forbidden* since they are considerably less likely to occur than allowed decays. The degree by which a transition is forbidden depends on how many terms in the plane wave approximation need to be taken into account until a nonvanishing nuclear matrix element is obtained. The second term gives rise to *first-forbidden* transitions, the third to *second-forbidden*, and so on. We will consider in the following only allowed β-decay transitions.

The density of final states, dn/dE_0, in Eq. (1.49) determines for allowed transitions the shape of the electron (or positron) energy distribution. It is given by (Problem 1.10)

$$\frac{dn}{dE_0} = \frac{dn_e dn_\nu}{dE_0} = \frac{(4\pi)^2 V^2}{h^6} p^2\, dp\, q^2\, dq \frac{1}{dE_0} \tag{1.55}$$

The final state (or total decay) energy is $E_0 = Q = K_e + E_\nu$, where Q is the energy release for the transition under consideration (see Eqs. (1.45) and (1.46); if the decay proceeds to an excited state, Q must account for the excitation energy). Since the neutrino mass is very small, we may use $m_\nu c^2 \approx 0$, so that $q = E_\nu/c = (E_0 - K_e)/c$ and $dq/dE_0 = 1/c$. A correction must be applied to Eq. (1.55) that takes into account the Coulomb interaction between the daughter nucleus and the emitted electron or positron. The electron in β^--decay feels an attractive Coulomb force, while the positron in β^+-decay experiences a repulsive force. Hence, the electron or positron plane wave in Eq. (1.51) has to be replaced by a distorted wave. The correction factor is referred to as *Fermi function*, $F(Z', p)$, and depends on the electron or positron momentum and the charge of the daughter nucleus. The function $F(Z', p)$ can be calculated numerically and is tabulated in Gove and Martin (1971).

It follows from Eqs. (1.49), (1.54), and (1.55) that

$$d\lambda = N(p)\, dp = \frac{1}{2\pi^3 \hbar^7 c^3} \left(G_V^2 M_F^2 + G_A^2 M_{GT}^2\right) F(Z', p) p^2 (E_0 - K_e)^2\, dp \tag{1.56}$$

This distribution vanishes for $p = 0$ and at the endpoint where the maximum electron or positron kinetic energy is equal to the total decay energy, $K_e^{max} = E_0 = Q$. Hence, a measurement of the momentum or energy distribution in a given decay yields a value for the total energy release in β-decay. Total relativistic energy, kinetic energy, and linear momentum of the electron or positron are related by

$$E_e = K_e + m_e c^2 = \sqrt{(m_e c^2)^2 + (pc)^2} \tag{1.57}$$

The total decay constant is then given by the integral

$$\lambda = \frac{\ln 2}{T_{1/2}} = \frac{\left(G_V^2 M_F^2 + G_A^2 M_{\mathrm{GT}}^2\right)}{2\pi^3 \hbar^7 c^3} \int_0^{p_{\max}} F(Z', p) p^2 (E_0 - K_{\mathrm{e}})^2 \, dp$$
$$= \frac{m_{\mathrm{e}}^5 c^4}{2\pi^3 \hbar^7} \left(G_V^2 M_F^2 + G_A^2 M_{\mathrm{GT}}^2\right) f(Z', E_{\mathrm{e}}^{\max}) \tag{1.58}$$

The dimensionless quantity

$$f(Z', E_{\mathrm{e}}^{\max}) = \frac{1}{m_{\mathrm{e}}^5 c^7} \int_0^{p_{\max}} F(Z', p) p^2 (E_{\mathrm{e}}^{\max} - E_{\mathrm{e}})^2 \, dp \tag{1.59}$$

is referred to as the *Fermi integral* and depends only on the charge Z' of the daughter nucleus and on the maximum total energy of the electron, $E_{\mathrm{e}}^{\max}$. Numerical values of $f(Z', E_{\mathrm{e}}^{\max})$ have also been tabulated. For the derivation of Eq. (1.58), we used the relationships $p_{\max} c = \sqrt{(E_{\mathrm{e}}^{\max})^2 - (m_e c^2)^2}$ and $E_0 - K_{\mathrm{e}} = K_{\mathrm{e}}^{\max} - K_{\mathrm{e}} = E_{\mathrm{e}}^{\max} - E_{\mathrm{e}}$ that are obtained from Eq. (1.57).

We can rewrite Eq. (1.58) as

$$f(Z', E_{\mathrm{e}}^{\max}) T_{1/2} = \frac{2\pi^3 \hbar^7}{m_{\mathrm{e}}^5 c^4} \frac{\ln 2}{\left(G_V^2 M_F^2 + G_A^2 M_{\mathrm{GT}}^2\right)} \tag{1.60}$$

The quantity $f(Z', E_{\mathrm{e}}^{\max}) T_{1/2}$ is called the *ft-value* and is experimentally obtained from measurements of the half-life and the maximum energy of the emitted electrons or positrons. The ft-value is a standard measure for the strength of a particular β-decay transition and yields information about the nuclear matrix elements and the coupling constants.

Electron Capture

The decay constant for allowed electron capture can be obtained in a similar manner. Recall that in this case the energy spectrum of the emitted neutrino is not continuous, but monoenergetic with $Q_{EC} = E_0 = E_\nu$. Instead of Eq. (1.49) we write

$$\lambda = \frac{2\pi}{\hbar} \left| \int \Psi_f^* H \Psi_i \, dV \right|^2 \frac{dn}{dE_0} = \frac{2\pi}{\hbar} |H_{fi}|^2 \frac{dn_\nu}{dE_0} \tag{1.61}$$

The density of final states in this case is given by (Problem 1.10)

$$\frac{dn_\nu}{dE_0} = \frac{Vq^2}{2\pi^2 \hbar^3} \frac{dq}{dE_0} = \frac{VE_\nu^2}{2\pi^2 \hbar^3 c^3} \tag{1.62}$$

where we used $E_\nu = qc$. The total wave functions before and after the decay are now given by $\Psi_i = \psi_i \phi_{\mathrm{e}}$ and $\Psi_f = \psi_f \phi_\nu$ (the subscripts have the same meaning as before). Usually an electron from the atomic K shell is captured because these have the largest probability of being near the nucleus. But the electron is now in a bound state and cannot be described by a free-particle plane wave. One can approximate ϕ_{e} by the electron wave function ϕ_K of the K orbit at the location of the nucleus,

$$\phi_e(\vec{r}) = \phi_K(\vec{r}) = \frac{1}{\sqrt{\pi}} \left(\frac{Z}{a_0}\right)^{3/2} e^{-Zr/a_0}$$
$$\approx \phi_K(0) = \frac{1}{\sqrt{\pi}} \left(\frac{Z}{a_0}\right)^{3/2} = \frac{1}{\sqrt{\pi}} \left(\frac{Z m_e e^2}{\hbar^2}\right)^{3/2} \tag{1.63}$$

with Z the atomic number of the parent nucleus. The constant a_0 denotes the Bohr radius, $a_0 = \hbar^2/(m_e e^2) = 0.0529$ nm. For the neutrino wave function ϕ_ν, we use again only the first (constant) term in the plane wave approximation.

From Eqs. (1.52), (1.61)–(1.63), one finds for the decay constant of allowed electron capture

$$\lambda_K = 2\frac{Z^3 m_e^3 e^6}{\pi^2 \hbar^{10} c^3} \left(G_V^2 M_F^2 + G_A^2 M_{GT}^2\right) E_\nu^2 \tag{1.64}$$

where the matrix elements are defined as before in terms of initial and final state nuclear wave functions. These are identical to the matrix elements that occur in Eq. (1.54) for positron emission, since they connect the very same nuclear states. The additional factor of two in Eq. (1.64) arises because either of the two electrons in the K shell can be captured. The transition probability for the weaker L-capture can be calculated in a similar manner. The electron capture probability increases strongly with the charge Z of the parent nucleus. This is the reason why electron capture is greatly favored over positron emission in heavy nuclei. The above expression must be corrected for relativistic effects and the influence of the shielding of the nuclear Coulomb field by the outer electrons. Such corrections have been calculated numerically and are tabulated, for example, in Gove and Martin (1971).

Fermi and Gamow–Teller Transitions

We already commented on the classification of β-decays into allowed and forbidden transitions. In the first case, the leptons do not remove any orbital angular momentum. In the latter case, the radiations are inhibited because angular momentum conservation requires the leptons to carry off orbital angular momentum or because the parities of the initial and final nuclear states are mismatched. The allowed radiations are further subdivided into *Fermi transitions* and *Gamow–Teller transitions*. They can only occur (i.e., the corresponding matrix elements M_F or M_{GT} are nonzero only) if certain selection rules are satisfied for the nuclear spins (J_i, J_f) and parities (π_i, π_f) of the initial and final nuclear states connected by the transition:

$$\Delta J \equiv |J_i - J_f| = 0, \qquad \pi_i = \pi_f \qquad \text{for Fermi transitions} \tag{1.65}$$

$$\Delta J \equiv |J_i - J_f| = 0 \text{ or } 1, \qquad \pi_i = \pi_f \qquad \text{for Gamow–Teller transitions (but not } J_i = 0 \to J_f = 0) \tag{1.66}$$

It follows that one can study these cases separately since decays with $0 \to 0$ ($\Delta J = 0$) and $\pi_i = \pi_f$ represent pure Fermi transitions ($M_{GT} = 0$), while decays with

$\Delta J = 1$ and $\pi_i = \pi_f$ are pure Gamow–Teller transitions ($M_F = 0$). Examples for pure Fermi and Gamow–Teller transitions are $^{14}\mathrm{O} \rightarrow {}^{14}\mathrm{N} + \mathrm{e}^+ + \nu$ ($J_i = 0^+ \rightarrow J_f = 0^+$) and $^6\mathrm{He} \rightarrow {}^6\mathrm{Li} + \mathrm{e}^- + \overline{\nu}$ ($J_i = 0^+ \rightarrow J_f = 1^+$). The decay of the free neutron in Eq. (1.39), on the other hand, represents a mixed transition. From studies of such decays, the values of the coupling constants G_V and G_A can be deduced (see, e.g., Wilkinson, 1994).

In the laboratory, where the parent nucleus is usually in its ground state, β-decay transitions proceed to all energetically accessible states in the daughter nucleus. The total decay constant is given by the sum of transition probabilities for all of these β-decay branches. Such laboratory β-decay constants or half-lives are independent of temperature and density. Experimental values of $T_{1/2}$ are tabulated in Audi *et al.* (2012) and this reference will be used as a source of terrestrial half-lives throughout this book, unless mentioned otherwise.

1.8.4
β-Decays in a Stellar Plasma

Consider now the weak interaction processes that take place when β-decays occur in a stellar plasma at elevated temperature T and density ρ. In a hot plasma, excited states in the parent nucleus are thermally populated and these excited levels may also undergo β-decay transitions to the ground state or to excited states in the daughter nucleus. The total β-decay rate in a stellar plasma, λ_β^*, is given by the weighted sum of the individual transition rates, λ_{ij}, according to

$$\lambda_\beta^* = \sum_i P_i \sum_j \lambda_{ij} \tag{1.67}$$

The sum on i and j is over parent and daughter states, respectively. The population probabilities, P_i, of excited states in a nondegenerate plasma at thermodynamic equilibrium are given by Eq. (1.35). Since the quantity P_i is temperature dependent, it follows immediately that λ_β^* will also depend on temperature. If the decay constants for excited state β-decays are larger than the one for ground-state β-decay, the total decay constant λ_β^* may become strongly temperature dependent. Even if the ground state of the parent nucleus is stable in the laboratory, it may nevertheless undergo β-decay in a hot stellar plasma. Similar considerations apply to the β-decay of the daughter nucleus. In the laboratory, it cannot decay back to the parent nucleus because the transition is energetically forbidden. In a hot plasma, however, β-decay transitions may occur from thermally populated excited states in the daughter nucleus to the ground state or to excited states in the parent nucleus. The situation is schematically shown in Figure 1.17. In practice, one finds that most of the transition probability for β^--decay or positron emission in a hot stellar plasma arises from the first few levels in a given parent nucleus. The β^--decay rate becomes also density dependent at sufficiently large values of ρ when the electron gas is degenerate. The decay rate decreases with increasing density since the number of final states available for the emitted electron to occupy is reduced (Langanke and Martinez-Pinedo, 2000).

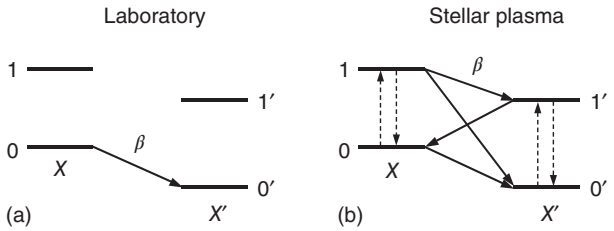

Figure 1.17 β-Decays (a) in the laboratory, and (b) in a hot stellar plasma. The vertical direction corresponds to an energy scale. For reasons of clarity, only two levels are shown in the parent nucleus X and the daughter nucleus X'. The ground and first excited state are labeled by 0 and 1, respectively. In the laboratory, the β-decay proceeds from the ground state of nucleus X to levels in nucleus X', while far more β-decay transitions are energetically accessible in a stellar plasma owing to the thermal excitation of levels (dashed vertical arrows).

Example 1.5

In the laboratory, β^+-decays of the nuclide ^{26}Al have been observed both from the ground state ($J^\pi = 5^+$) and from the first excited (isomeric) state ($J^\pi = 0^+$) located at an excitation energy of $E_x = 228$ keV (Figure 1.15). The ground state decays via positron emission to excited levels in the daughter nucleus ^{26}Mg (we will neglect a small electron capture branch) with a half-life of $T^{\rm gs}_{1/2} = 7.17 \times 10^5$ y, while the first excited state decays to the ^{26}Mg ground state with a half-life of $T^{m}_{1/2} = 6.345$ s. Above a temperature of $T = 0.4$ GK, both of these ^{26}Al levels are in thermal equilibrium (Figure 1.16). Calculate the *stellar* half-life of ^{26}Al when the plasma temperature amounts to $T = 2$ GK.

According to Eq. (1.67), the decay constant of ^{26}Al in the stellar plasma is given by

$$\lambda^*_\beta = P_{\rm gs}\lambda_{\rm gs} + P_m\lambda_m = P_{\rm gs}\frac{\ln 2}{T^{\rm gs}_{1/2}} + P_m\frac{\ln 2}{T^{m}_{1/2}}$$

where the subscripts *gs* and *m* denote the ground state and the first excited state, respectively. The thermal population probability P_i (i.e., the fraction of ^{26}Al nuclei residing in either the ground or the first excited state) can be calculated from Eq. (1.35) (a numerical expression for the quantity kT is given in Section 3.1.1). Thus

$$\begin{aligned}
\lambda^*_\beta &= \frac{\ln 2}{g_{\rm gs}e^{-E_{\rm gs}/kT} + g_m e^{-E_m/kT}}\left[\frac{g_{\rm gs}e^{-E_{\rm gs}/kT}}{T^{\rm gs}_{1/2}} + \frac{g_m e^{-E_m/kT}}{T^{m}_{1/2}}\right] \\
&= \frac{\ln 2}{(2\cdot 5+1) + (2\cdot 0+1)e^{-0.228/kT}}\left[\frac{(2\cdot 5+1)}{T^{\rm gs}_{1/2}} + \frac{(2\cdot 0+1)e^{-0.228/kT}}{T^{m}_{1/2}}\right] \\
&= \frac{\ln 2}{11 + e^{-0.228/0.0862\,T_9}}\left[\frac{11}{T^{\rm gs}_{1/2}} + \frac{e^{-0.228/0.0862\,T_9}}{T^{m}_{1/2}}\right] \\
&\approx \frac{\ln 2}{11}\left[\frac{e^{-0.228/0.0862\,T_9}}{6.345\,\text{s}}\right] = 9.93\times 10^{-3}e^{-2.646/T_9} \quad (\text{s}^{-1})
\end{aligned}$$

Hence, we find at $T = 2$ GK ($T_9 = 2$)

$$\lambda_\beta^* = 9.93 \times 10^{-3} e^{-2.646/2.0}\,\mathrm{s}^{-1} = 0.0026\,\mathrm{s}^{-1}$$

and the stellar half-life of ^{26}Al amounts to $T_{1/2}^* = \ln 2/\lambda_\beta^* = 270$ s. The result is valid only for densities of $\rho \leq 10^6$ g/cm^3, since at higher densities electron capture needs to be taken into account (see below). The results from the above method for calculating the stellar half-life of ^{26}Al are shown as the dashed line in Figure 1.16. The values are only correct for temperatures in the range of $T = 0.4$–5 GK. At lower temperatures, the ground and isomeric states are not in thermal equilibrium (Section 1.7.5), while at higher temperatures the thermal populations of other excited states in ^{26}Al have to be taken into account.

We will now discuss the interesting case of electron capture. It will be shown later (Section 3.1.1) that the average thermal energies at the temperatures typical for the interior of main-sequence stars and red giants amount to ≈ 1 keV and a few tens of kilo electron volts, respectively. For most atoms, however, the ionization energies are smaller than these values. Therefore, most nuclei in these environments possess few, if any, bound electrons. The decay constant for bound electron capture, given by Eq. (1.64), may thus be very small or even zero. In the hot interiors of stars, however, there is an appreciable density of free electrons. Hence, β-decays can proceed by capture of (free) electrons from the continuum. The probability of continuum electron capture is proportional to the free electron density at the location of the nucleus and is inversely proportional to the average electron velocity which depends on the plasma temperature. Consequently, the rate of continuum electron capture depends on the local electron temperature and the density. At lower stellar temperatures, a given parent nucleus may not be completely ionized. In that case, both bound and continuum electron capture contribute to the total decay constant.

At low densities, the kinetic energies of the free electrons are usually small. At very high densities, however, the (Fermi) energy of the degenerate electrons may become sufficiently large to cause nuclei to undergo continuum capture of energetic electrons, even if they are stable under laboratory conditions. Electron capture transitions involving thermally excited nuclear levels must also be taken into account according to Eq. (1.67).

Moreover, at high temperature ($T > 1$ GK) a large number of photons have energies in excess of the threshold energy for pair production (Section 4.2.2). Although a positron annihilates quickly in the stellar plasma with an electron, the pair production rate becomes eventually so large at high temperatures that the positron density is a significant fraction of the electron density. Thus, capture of continuum positrons by nuclei must be considered in addition to continuum electron capture.

The decay constant for continuum electron capture can be obtained for a given nuclide if its laboratory decay constant for bound electron capture is known. The ratio of stellar to laboratory decay constant is approximately equal to the ratio of

the electron densities at the nucleus for the stellar and laboratory environments, that is, the ratio of probabilities for finding an electron at the nucleus where it can be captured. An order of magnitude estimate for the ratio of electron capture probabilities is given by

$$\frac{\lambda_{\rm star}}{\lambda_{\rm lab}} \approx \frac{n_{\rm e^-}\langle F(Z,p)\rangle}{2N_A|\phi_{\rm e}(0)|^2} \tag{1.68}$$

where $n_{\rm e^-}/N_A = \rho(1-\eta)/2 = \rho Y_{\rm e}$ is the electron density (Fowler, Caughlan, and Zimmerman, 1967), η is the neutron excess parameter given by Eq. (1.36), $Y_{\rm e}$ is the electron mole fraction given by Eq. (1.37), and $|\phi_{\rm e}(0)|^2$ is given by Eq. (1.63). The Fermi function $F(Z,p)$ accounts for the distortion of the wave function of the captured electron by the nuclear Coulomb field. Since the electron velocities in the plasma are given by a distribution, the Fermi function must be averaged over the electron velocities. It can be seen from Eq. (1.68) that the ratio $\lambda_{\rm star}/\lambda_{\rm lab}$ depends on the density and composition (through $n_{\rm e^-}$), and on the temperature (through $\langle F(Z,p)\rangle$). The above expression is independent of nuclear matrix elements. For more information, including a discussion of induced continuum electron capture (i.e., when a nuclide is stable in the laboratory), see Bahcall (1964).

Many different transitions contribute to the stellar decay rate of a given nucleus. In the laboratory, the decay proceeds from the ground state of parent nucleus X to energetically accessible states in the daughter nucleus X'. In a stellar plasma, the labels "parent" and "daughter" can alternatively apply to both nuclei. For example, in the laboratory ^{56}Mn decays to the stable nuclide ^{56}Fe via ^{56}Mn$(\beta^-\nu)^{56}$Fe. At high temperatures and densities, however, ^{56}Fe decays via continuum electron capture, ^{56}Fe$(e^-,\nu)^{56}$Mn, and via positron emission through thermally populated ^{56}Fe states, ^{56}Fe$(e^+\nu)^{56}$Mn.

The estimation of stellar β-decay rates essentially reduces to the calculation of (i) nuclear matrix elements using some model of nuclear structure (e.g., the shell model; Section 1.6), and (ii) the appropriate Fermi functions and integrals for all energetically accessible transitions from the parent to the daughter nucleus. The calculations can be constrained and tested by experimental measurements of half-lives and Gamow–Teller strength distributions. Stellar weak interaction rates and the associated neutrino energy losses for a range of temperatures and densities are tabulated in Fuller, Fowler, and Newman (1982) (for the proton, neutron, and nuclides with $A = 21$–60), Oda *et al.* (1994) (for $A = 17$–39), and Langanke and Martinez-Pinedo (2001) (for $A = 45$–65). Figure 1.18 shows as an example the stellar decay constants versus temperature for the electron capture (solid lines) and positron emission (dashed line) of ^{37}Ar. The three lines for electron capture correspond to different values of $\rho Y_{\rm e} = \rho(1-\eta)/2$. The strong density dependence of the electron capture rate is apparent. In the laboratory, ^{37}Ar decays to ^{37}Cl by bound electron capture with a half-life of $T_{1/2} = 35.0$ d (horizontal solid line).

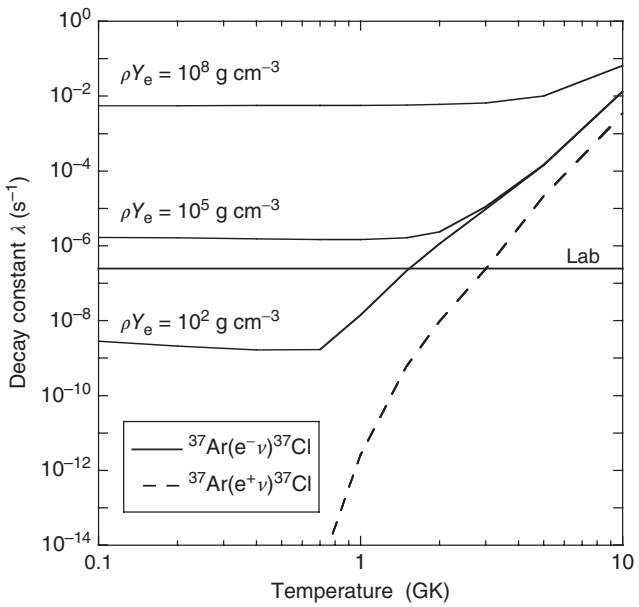

Figure 1.18 Stellar decay constants versus temperature for the electron capture (thin solid lines) and positron emission (dashed line) of ^{37}Ar. The three lines for electron capture correspond to different values of $\rho Y_e = \rho(1-\eta)/2$, whereas the decay rate for positron emission is independent of density. In the laboratory, ^{37}Ar decays to ^{37}Cl by bound electron capture with a decay constant of $\lambda_{lab} = 2.3\times10^{-7}$ s^{-1} ($T_{1/2} = \ln 2/\lambda_{lab}$ = 35.0 d), shown as the horizontal solid line labeled "Lab". Data from Oda *et al.* (1994).

Finally, we will briefly discuss a neutrino energy loss mechanism that becomes important at very high temperatures and densities. It is referred to as the *Urca process* (Gamow and Schoenberg, 1940) and consists of alternate electron captures and β^--decays involving the same pair of parent and daughter nuclei

$$ {}^A_Z\mathrm{X}_N(\mathrm{e}^-,\nu)\,{}^A_{Z-1}\mathrm{X}'_{N+1}(\beta^-\nu)\,{}^A_Z\mathrm{X}_N \ldots \tag{1.69} $$

The net result of two subsequent decays gives ${}^A_Z\mathrm{X}_N + \mathrm{e}^- \rightarrow {}^A_Z\mathrm{X}_N + \mathrm{e}^- + \nu + \overline{\nu}$. A neutrino–antineutrino pair is produced with no change in the composition, but energy in the form of neutrinos is lost from the star. It is obvious from energy arguments that both the electron capture and the β^--decay cannot occur spontaneously. The first step may be induced by continuum electron capture of energetic electrons when the density is high, while the second step may proceed from thermally populated excited states when the temperature is high. In the end, thermal energy is lost every time a pair of interactions goes to completion. The mechanism represents an efficient cooling process that will not only depend on temperature and density but also on the composition of the stellar plasma. The Urca process is thought to be vital for understanding the explosion mechanism in some models of type Ia supernovae (Section 1.4.4).

Problems

1.1 Determine the number of protons, Z, and the number of neutrons, N, for the nuclides ^{18}F, ^{56}Ni, ^{82}Rb, ^{120}In, ^{150}Gd, and ^{235}U.

1.2 How much energy is released in the following reactions: (i) ^{3}He(d,p)^{4}He; (ii) ^{17}O(p,γ)^{18}F; (iii) ^{12}C(α,γ)^{16}O; and (iv) ^{13}C(α,n)^{16}O? Assume that the reactions involve nuclei only in their ground states. Use the results presented in Table 1.1.

1.3 Consider the chain of radioactive decays, $1 \rightarrow 2 \rightarrow 3$, where 1, 2, and 3 denote a parent, daughter, and final nuclide respectively. Assume that initially only the parent nuclei are present, that is, $N_1(t = 0) = N_0$, $N_2(t = 0) = 0$, $N_3(t = 0) = 0$, and that species 3 is stable. (i) Set up the differential equation describing the abundance change of species 2 and find the time evolution of the daughter abundance, $N_2(t)$. (ii) Find the time evolution of the final nuclide abundance, $N_3(t)$. (iii) Examine the abundances N_1, N_2, and N_3 at small values of t. Keep only the linear terms in the expansion of the exponential function and interpret the results.

1.4 With the aid of Figure 1.11, predict the spins and parities of ^{19}O, ^{31}P, and ^{37}Cl for both the ground state and the first excited state. Compare your answer with the observed values. These can be found in Endt (1990) and Tilley *et al.* (1995).

1.5 Suppose that an excited state with spin and parity of 2^+ in a nucleus of mass $A = 20$ decays via emission of a γ-ray with a branching ratio of 100% to a lower lying level with spin and parity of 0^+. Assume that the γ-ray energy amounts to $E_\gamma = E_i - E_f = 6$ MeV. Estimate the maximum expected γ-ray transition probability $\Gamma = \lambda\hbar$.

1.6 Consider a nucleus in a plasma at thermal equilibrium. Calculate the population probabilities of the ground state ($E_0 = 0$) and of the first three excited states ($E_1 = 0.1$ MeV, $E_2 = 0.5$ MeV, $E_3 = 1.0$ MeV). Perform the computations for two temperatures, $T = 1.0 \times 10^9$ K and 3.0×10^9 K, and assume for simplicity that all states have the same spin value.

1.7 Derive the relationships of Eqs. (1.45)–(1.47) from the differences in *nuclear* masses before and after the decay.

1.8 How much energy is released in the following β-decays: (i) ^{7}Be(e$^-$,ν)^{7}Li; (ii) ^{14}C($\beta^-\nu$)^{14}N; and (iii) ^{18}F(e$^+\nu$)^{18}O? Assume that the decays involve nuclei in their ground states only. Use the results presented in Table 1.1.

1.9 Calculate the average neutrino energy losses in the decays ^{13}N(e$^+\nu$)^{13}C and ^{15}O(e$^+\nu$)^{15}N. Assume that the positron emissions involve the ground states of the parent and daughter nuclei only. Use the results presented in Table 1.1.

1.10 Derive Eq. (1.55) for the density of final states. Recall that the final state contains both an electron and a neutrino. You have to count the states in the six-dimensional *phase space* that is defined by three space and three linear momentum coordinates. The unit volume in phase space is h^3.